



**HAL**  
open science

# Gas-sheared falling liquid films beyond the absolute instability limit

Misa Ishimura, Sophie Mergui, Christian Ruyer-Quil, Georg F. Dietze

► **To cite this version:**

Misa Ishimura, Sophie Mergui, Christian Ruyer-Quil, Georg F. Dietze. Gas-sheared falling liquid films beyond the absolute instability limit. *Journal of Fluid Mechanics*, 2023, 971, pp.A37. 10.1017/jfm.2023.670 . hal-04304395

**HAL Id: hal-04304395**

**<https://hal.science/hal-04304395>**

Submitted on 24 Nov 2023

**HAL** is a multi-disciplinary open access archive for the deposit and dissemination of scientific research documents, whether they are published or not. The documents may come from teaching and research institutions in France or abroad, or from public or private research centers.

L'archive ouverte pluridisciplinaire **HAL**, est destinée au dépôt et à la diffusion de documents scientifiques de niveau recherche, publiés ou non, émanant des établissements d'enseignement et de recherche français ou étrangers, des laboratoires publics ou privés.

Banner appropriate to article type will appear here in typeset article

# 1 **Gas-sheared falling liquid films beyond the absolute** 2 **instability limit**

3 **Misa Ishimura<sup>1,3,4</sup>, S. Mergui<sup>1,2</sup>, C. Ruyer-Quil<sup>3</sup>, and G. F. Dietze<sup>1</sup>†**

4 <sup>1</sup>Université Paris-Saclay, CNRS, FAST, 91405, Orsay, France.

5 <sup>2</sup>Sorbonne Université, UFR 919, 4 place Jussieu, F-75252 Paris CEDEX 05, France.

6 <sup>3</sup>Université Savoie Mont Blanc, CNRS, LOCIE, 73376 Le Bourget du Lac, France.

7 <sup>4</sup>Department of Mechanical Engineering, Yokohama National University, Kanagawa 240-8501, Japan.

8 (Received 9 August 2023; revised xx; accepted xx)

9 We study the effect of a confined turbulent counter-current gas flow on the waviness of a  
10 weakly-inclined falling liquid film. Our study is centered on experiments in a channel of 13  
11 mm height, using water and air, where we have successively increased the counter-current gas  
12 flow rate until flooding. Computations with a new low-dimensional model and linear stability  
13 calculations are used to elucidate the linear and nonlinear wave dynamics. We find that the gas  
14 pressure gradient plays an important role in countering the stabilizing effect of the tangential  
15 gas shear stress at the liquid-gas interface. At very low inclination angles, the latter effect  
16 dominates and can suppress the long-wave Kapitza instability unconditionally. By contrast,  
17 for non-negligible inclination, the gas-effect is linearly destabilizing, amplifies the height of  
18 nonlinear Kapitza waves, and exacerbates coalescence-induced formation of large-amplitude  
19 tsunami waves. Kapitza waves do not undergo any catastrophic transformation when the  
20 counter-current gas flow rate is increased beyond the absolute instability (AI) limit. On the  
21 contrary, we find that AI is an effective linear wave selection mechanism in a noise-driven  
22 wave evolution scenario, leading to highly regular downward-travelling nonlinear wave trains,  
23 which preclude coalescence events. In our experiments, where Kapitza waves develop in a  
24 protected region before coming into contact with the gas, flooding is eventually caused far  
25 beyond the AI limit by upward-travelling short-wave ripples. Based on our linear stability  
26 calculations for arbitrary wave numbers, we have uncovered a new short-wave interfacial  
27 instability mode with negative linear wave speed, causing these ripples.

28 **Key words:** Thin films, gas/liquid flow

---

## 29 **1. Introduction**

30 Falling liquid films intervene in many engineering applications (Alekseenko *et al.* 2007;  
31 Azzopardi *et al.* 2011; Lapkin & Anastas 2018). One example are rectification columns  
32 containing structured packings for cryogenic air separation (Fair & Bravo 1990), where

† Email address for correspondence: dietze@fast.u-psud.fr

the liquid film is subject to a turbulent counter-current gas flow within narrow channels (Valluri *et al.* 2005). Surface waves, forming at the liquid-gas interface due to the inertia-driven Kapitza instability (Kapitza 1948), which consist of large humps preceded by several precursory capillary ripples, are known to greatly intensify inter-phase heat and mass transfer (Yoshimura *et al.* 1996; Miyara 1999; Dietze 2019). At the same time, they can trigger flooding events (Bankoff & Lee 1986) that are detrimental to adequate process operation. Such events include obstruction of the channel cross-section (Vlachos *et al.* 2001), wave reversal (Tseluiko & Kalliadasis 2011), fragmentation and droplet entrainment (Zapke & Kröger 2000), or (partial) liquid reversal (Trifonov 2010*b*, 2019). In light of these two competing roles played by surface waves, numerous experimental (Vlachos *et al.* 2001; Drosos *et al.* 2006; Kofman *et al.* 2017), numerical (Trifonov 2010*a*; Vellingiri *et al.* 2015; Schmidt *et al.* 2016; Trifonov 2019; Lavalle *et al.* 2019), and modelling (Tseluiko & Kalliadasis 2011; Dietze & Ruyer-Quil 2013; Lavalle *et al.* 2020, 2021) works have been dedicated to unraveling the effect of a counter-current gas flow on the linear and nonlinear dynamics of wavy falling liquid films. Our current manuscript seeks to further contribute to this task.

We study the configuration of a laminar falling liquid film sheared by a turbulent counter-current gas flow confined in a rectangular channel of height  $H^* \sim 10$  mm (the star superscript denotes dimensional quantities throughout), according to the experimental setup sketched in figure 1. The confinement level chosen here is representative of structured packings (Fair & Bravo 1990) and lies in between those used in the experiments of Lavalle *et al.* (2019),  $H^* \sim 5$  mm, where the gas flow was laminar, and those of Kofman *et al.* (2017),  $H^* \sim 20$  mm, where the confinement was weak and the gas flow was turbulent. We have applied three different approaches to study this flow: (i) experiments, where developed surface waves of prescribed frequency were produced within a protected zone before being submitted to the counter-current gas flow, (ii) linear stability analysis based on the full governing equations, and (iii) nonlinear numerical computations with a new integral boundary layer model. Our study is guided by a set of experimental runs, where we have successively increased the counter-current gas flow rate, starting from conditions where the gas-effect is weak, up until breakdown of the experiment due to flooding. Computations with our low-dimensional model and linear stability calculations have allowed us to elucidate the linear and nonlinear wave dynamics associated with this transition.

We focus mainly (but not exclusively) on weakly-inclined falling liquid films, which allows to investigate weakly supercritical flow regimes. According to Brooke Benjamin (1957) and Yih (1963), the onset of the Kapitza instability for a liquid film falling in a passive atmosphere is given by  $\text{Re}_L = 5/6 \cot(\phi)$ , where  $\phi$  denotes the inclination angle, and  $\text{Re}_L = q_L^* / \nu_L$  is the liquid Reynolds number based on the liquid flow rate per unit width  $q_L^*$  and liquid kinematic viscosity  $\nu_L$ . Thus, the smaller  $\phi$ , the more closely the instability threshold can be approached while maintaining an experimentally realizable film thickness  $h_0^* = (3\text{Re}_L \nu_L^2 / g / \sin(\phi))^{1/3}$ , where the subscript 0 denotes the primary flow and  $g$  the gravitational acceleration. Closer to the instability threshold, the interfacial dynamics are less complicated and surface waves are predominantly two-dimensional (Kofman *et al.* 2014).

Our current work is inspired by several recent findings reported in the literature, which we discuss next. Lavalle *et al.* (2019) demonstrated that the onset of the Kapitza instability can be significantly delayed at low inclination angles, by strongly confining the surrounding gas, as conjectured by Tilley *et al.* (1994). Moreover, they discovered that the gas-induced stabilization is strongest in the counter-current configuration, and increases with increasing magnitude of the gas flow rate. Kushnir *et al.* (2021) subsequently showed that stabilization also occurs in the case of a confined recirculating gas, i.e. when the net gas flow rate is zero. In the above three studies, the gas flow was considered laminar and the stabilization occurred

82 for strong confinement, i.e.  $H^* \leq 5$  mm. As demonstrated by Lavalle *et al.* (2019), it is  
 83 caused by the linear response of the interfacial tangential gas shear stress  $T_G$  to a perturbation  
 84 of the liquid film thickness. Potentially, gas-induced stabilization may thus be achieved for  
 85 weaker confinement if the gas flow is turbulent, as turbulence increases the magnitude of  
 86  $T_G$ . In the current manuscript, we have checked this hypothesis based on linear stability  
 87 calculations. In particular, we find that the Kapitza instability can be fully suppressed by a  
 88 turbulent counter-current gas flow for  $H^* \sim 10$  mm, when the inclination angle is very small  
 89 ( $\phi \sim 1^\circ$ ). By *full suppression*, we mean that the falling liquid film becomes unconditionally  
 90 stable to long-wave disturbances, i.e. for all  $\text{Re}_L$ . By contrast, at non-negligible inclination  
 91 ( $\phi \sim 5^\circ$ ), the linear gas-effect is destabilizing and the counter-current gas flow can render the  
 92 liquid film unconditionally unstable to long-wave disturbances, as previously reported for  
 93 laminar flow conditions (Trifonov 2017; Kushnir *et al.* 2021). We find that turbulence can  
 94 significantly delay the onset of this unconditional instability.

95 Recent numerical (Lavalley *et al.* 2021) and experimental (Mergui *et al.* 2023) investiga-  
 96 tions of weakly-inclined falling liquid films have shown that a strongly-confined laminar  
 97 counter-current gas flow can attenuate the amplitude of nonlinear travelling-wave solutions  
 98 (TWS), even though the linear gas-effect is destabilizing. In our current configuration, where  
 99 the inclination angle is similar but the confinement is weaker and the gas flow is turbulent,  
 100 both the TWS amplitude and the linear spatial growth rate increase with increasing counter-  
 101 current gas flow rate, at least until the absolute instability (AI) limit is reached.

102 Several works on gas-sheared falling liquid films in narrow (vertical) channels have  
 103 identified wave coalescence as a possible route toward flooding. For example, Drosos *et al.*  
 104 (2006) measured the probability density function of the wave height and found that the  
 105 dominant wave frequency strongly decreases as the flooding limit is approached. Later,  
 106 Dietze & Ruyer-Quil (2013) computed the noise-driven spatial evolution of Kapitza waves  
 107 sheared by a superconfined laminar gas flow and showed that coalescence can trigger an  
 108 intermittent obstruction of the channel. Geometrical obstruction is not possible in our current  
 109 configuration, where  $H^*$ , although smaller than the typical wavelength  $\Lambda^*$ , is much greater  
 110 than  $h_0^*$ . Nonetheless, we find that the counter-current gas flow exacerbates coalescence  
 111 events, entailing very large waves that form via the successive absorption of smaller waves.  
 112 Such waves have been designated as tsunami waves (Meza & Balakotaiah 2008), and we  
 113 will employ this term throughout. In particular, the onset of coalescence moves upstream  
 114 significantly when the counter-current gas flow rate is increased, precipitating the usual wave  
 115 coarsening dynamics observed in liquid films falling in a quiescent gas (Chang *et al.* 1996b).

116 The transition between convective instability (spatial growth) and absolute instability  
 117 (temporal growth), which occurs when the counter-current gas flow rate is increased, has been  
 118 suggested as another potential cause for the onset of flooding. For example, Vellingiri *et al.*  
 119 (2015) showed that the AI limit predicted by their linear stability analysis lies not too far  
 120 from the flooding threshold reported in the experiments of Zapke & Kröger (2000), where  
 121 a vertically-falling liquid film was sheared by a counter-current gas flow. However, the  
 122 trends of the two limits versus the liquid Reynolds number  $\text{Re}_L$  were opposed, i.e. the  
 123 flooding onset, expressed in terms of the superficial gas velocity, increased with increasing  
 124  $\text{Re}_L$ , whereas the AI limit diminished. In the current work, we have thus explored the spatio-  
 125 temporal evolution of nonlinear Kapitza waves beyond the AI limit, based on experiments and  
 126 numerical computations. We find that AI is not necessarily dangerous in our configuration,  
 127 i.e. no catastrophic events occur until far beyond the AI limit. Moreover, in the case of a  
 128 noise-driven wave evolution scenario, AI can act as an effective linear selection mechanism,  
 129 leading to a regular train of downward-travelling nonlinear surface waves, thus precluding  
 130 dangerous coalescence events.

131 Lavalle *et al.* (2020) studied vertically-falling wavy liquid films sheared by a superconfined

132 laminar counter-current gas flow, and discovered an oscillatory secondary instability. This  
133 instability entails a regular spatial modulation of TWS generated by coherent inlet forcing.  
134 We have performed computations for the same liquid-side parameters, but with our moderate  
135 confinement, i.e.  $H^* \sim 10$  mm. Although we do not observe any oscillatory instability, wave  
136 amplitude modulations occur nonetheless, albeit due to an entirely different mechanism,  
137 which sets in beyond the AI limit. There, a competition between the forcing frequency and  
138 the absolute frequency can lead to coalescence-induced tsunami waves that are separated by  
139 a long and thin residual film, on which small-amplitude standing ripples form as a result of  
140 AI. These ripples continually perturb the tsunami waves passing over them, similar to the  
141 effect of wall corrugations (Dietze 2019).

142 Several numerical works have suggested that a counter-current gas flow may provoke  
143 the reversal of nonlinear Kapitza waves, which can be viewed as another manifestation  
144 of flooding. Tseluiko & Kalliadasis (2011) observed this for a vertically-falling liquid film  
145 sheared by a weakly-confined turbulent gas flow. However, in their computations, the average  
146 film thickness  $\bar{h}$  was fixed instead of the liquid flow rate, which is more representative of  
147 a sudden gas flow rate increase in an experiment. Trifonov (2017) observed the reversal of  
148 travelling Kapitza waves in the case of an inclined falling liquid film sheared by a laminar  
149 gas flow. However, the gas Reynolds number in his computations was far greater than the  
150 turbulence threshold, i.e.  $|\text{Re}_G| > 10000$ . Lavalle *et al.* (2020) observed wave reversal due to  
151 a gas-induced secondary instability of TWS in the case of extreme confinement ( $H^* \sim 1$  mm).  
152 In our current configuration, where the liquid flow rate is imposed, the gas flow is turbulent,  
153 and the confinement is moderate, we did not observe any reversal of Kapitza waves, neither  
154 in terms of TWS nor in the case of spatially evolving waves.

155 In our experiments, flooding is triggered (far beyond the AI limit) by upward-travelling  
156 short ripples that first coexist with the initial Kapitza waves and then overpower the latter.  
157 As soon as these ripples appear, liquid, in the form of small droplets, starts to accumulate  
158 in the gas loop, eventually forcing a shut-down of the experiment. Such ripples were first  
159 observed in the experiments of Kofman *et al.* (2017). In the current manuscript, we elucidate  
160 their origin, which has remained an open question.

161 Kofman *et al.* (2017) pointed out that the ripples observed in their experiments have  
162 similar wavelengths and amplitudes than ripples forming in horizontal liquid films sheared  
163 by an unconfined co-current turbulent gas flow (Özgen *et al.* 2002). Those ripples are  
164 caused by a short-wave interfacial instability mode (Miesen & Boersma 1995). They have  
165 also been observed when the co-current gas flow is confined, e.g. in the experiments  
166 of Hanratty & Engen (1957), where  $H^* = 25.4$  mm, and where the ripples were seen to  
167 coalesce into fast-travelling slugs. The corresponding instability mode was identified by  
168 McCready & Chang (1994). They showed that the dispersion curve of the linear temporal  
169 growth rate  $kc_i$ , where  $k$  and  $c_i$  denote the wave number and complex celerity, originates at  
170  $k=c_i=0$ , and displays two unstable ( $kc_i > 0$ ) humps, one at small and another at large  $k$ , the  
171 short-wave hump being dominant. However, no short-wave instability mode has ever been  
172 identified for falling liquid films sheared by a counter-current (turbulent) gas flow, despite  
173 several previous linear stability investigations. And, the ripples observed in our experiments  
174 move upstream, i.e. in opposite direction to the liquid.

175 Schmidt *et al.* (2016) applied the Chebyshev collocation approach (Orszag 1971;  
176 Barmak *et al.* 2016a) to study this problem in the vertical configuration at  $|\text{Re}_G| > 35000$ ,  
177 where  $\text{Re}_G = q_G^* / \nu_G$  designates the gas Reynolds number based on the gas flow rate per unit  
178 width  $q_G^*$  and the gas kinematic viscosity  $\nu_G$ . Although the gas flow under these conditions  
179 would be turbulent in an experiment, the laminar Navier-Stokes equations were used. The  
180 authors identified four instability modes: (1) the long-wave Kapitza mode (Brooke Benjamin  
181 1957; Yih 1963), which is an interfacial mode; (2) the liquid-side short-wave Tollmien-

182 Schlichting mode (Floryan *et al.* 1987; Samanta 2020), which travels in the direction of  
 183 the liquid and occurs at very large  $Re_L$ ; (3) the gas-side short-wave Tollmien-Schlichting  
 184 mode; and (4) a so-called long-wave internal mode, which appears at  $|Re_G| \sim 10 \times 10^4$  and  
 185 can merge with the Kapitza mode. Trifonov (2017) applied the same approach to the case  
 186 of an inclined falling liquid film, and showed that the gas-side Tollmien-Schlichting mode  
 187 corresponds to the classical result for channel flow, i.e.  $|Re_G| = \frac{4}{3} 5772 = 7696$  (Orszag 1971).  
 188 This mode always travels in the direction of the gas flow, but it does not meaningfully perturb  
 189 the liquid-gas interface. Thus, it cannot generate the upward-travelling ripples observed in  
 190 our experiment, which, moreover, occur at  $|Re_G| \sim 6000$ .

191 The works of Schmidt *et al.* (2016) and Trifonov (2017) did not account for turbulence  
 192 in the primary flow, even though the gas Reynolds number  $|Re_G|$  was far greater than  
 193 the experimental turbulence threshold  $|Re_G| \sim 1800$  (Pope 2000). Following the seminal  
 194 work of Náraigh *et al.* (2011), this shortcoming was remedied by Vellingiri *et al.* (2015),  
 195 who represented the turbulent gas flow via the Reynolds averaged Navier-Stokes equations  
 196 (RANS), using curvilinear coordinates and Prandtl's mixing-length approach. These authors  
 197 observed a transition of the long-wave Kapitza instability from downward-convective to  
 198 upward-convective upon increasing the counter-current gas flow rate  $q_{L0}$ . However, as the  
 199 liquid film thickness  $h_0$  and not  $q_{L0}$  was fixed in these calculations, upward-travelling waves  
 200 were associated with  $q_{L0} < 0$ . By contrast,  $q_{L0}$  is fixed and positive in our experiments.  
 201 Vellingiri *et al.* (2015) did not identify any short-wave instability mode. Nonetheless, they  
 202 reported a non-monotonic variation of the cut-off wave number  $k_c$  upon increasing  $|Re_G|$  for  
 203 the long-wave instability mode, i.e. a decrease followed by an increase in  $k_c$ . Trifonov (2017)  
 204 later made a similar observation. We will show that this behavior results from an interaction  
 205 between the long-wave Kapitza instability mode and a new short-wave interfacial instability  
 206 mode, which we have detected via temporal linear stability calculations at fixed  $q_{L0} > 0$ , using  
 207 the Chebyshev collocation approach.

208 This new short-wave mode emerges around the AI limit of the long-wave Kapitza instability  
 209 mode, upon increasing the counter-current gas flow rate. Initially, the long-wave and short-  
 210 wave modes coexist, but, at sufficiently large  $|Re_G|$ , they merge to form a two-humped  
 211 dispersion curve originating at  $k=c_i=0$ , and the short-wave maximum eventually becomes  
 212 dominant. Linear waves corresponding to this maximum display a negative wave celerity  
 213  $c_r < 0$ , and both their wavelength  $\Lambda$  and  $c_r$  agree well with the upward-travelling ripples  
 214 observed in our experiment. The wave celerity  $c_r$  of the new short-wave instability mode  
 215 is always negative at the most-amplified wave number  $k=k_{max}$ , but it can change sign at  
 216 lower  $k$ . This is a fundamental difference with the gas-side Tollmien-Schlichting mode.  
 217 Conversely, when  $c_r < 0$ , the liquid film surface velocity is not necessarily negative. Thus,  
 218 ripples travel upward, even when the liquid travels downward across the entire film thickness.  
 219 This is a difference with the interfacial mode observed in co-current liquid/gas flows  
 220 (Miesen & Boersma 1995).

221 Nonlinear computations in the current manuscript have been performed with a new low-  
 222 dimensional model, which we introduce. Therein, the liquid film is represented via the  
 223 weighted residual integral boundary layer (WRIBL) approach of Ruyer-Quil & Manneville  
 224 (1998), leading to two coupled evolution equations for the local instantaneous film thickness  
 225  $h$  and liquid flow rate  $q_L$ . We develop these equations up to second order in the long-wave  
 226 parameter, and account for the effect of an adjacent gas via the gas shear stress  $T_G$  and  
 227 the gas pressure  $P_G$ , acting at the liquid-gas interface. Following Camassa *et al.* (2017), we  
 228 obtain these coupling quantities from a first-order long-wave (LW) approximation of the  
 229 gas-side RANS equations written in curvilinear coordinates (Thorsness *et al.* 1978), while  
 230 assuming a frozen liquid-gas interface. Our thus obtained WRIBL-LW model represents  
 231 several improvements w.r.t. previous works, which we will discuss next.

232 Demekhin (1981) used the IBL approach of Shkadov (1967) to model the liquid film, and  
233 accounted for the effect of a turbulent gas flow, via  $T_G$  and  $P_G$ , through the linear response of  
234 the gas-side RANS equations to a waviness of the liquid-gas interface (assumed frozen). This  
235 linearized approach is valid in the limit  $h/H \ll 1$ , i.e. assuming a large channel height versus  
236 the film thickness. Further, the authors invoked the quasi-laminar assumption (Miles 1957;  
237 Brooke Benjamin 1959), where turbulence enters only via the unperturbed flow and linear  
238 perturbations of the Reynolds stresses are neglected, which is usually valid in gas-sheared  
239 wavy liquid films (Náraigh *et al.* 2011). However, the liquid-side IBL approach is known to  
240 significantly over-predict the instability threshold of an inclined falling liquid film.

241 Tseluiko & Kalliadasis (2011) remedied this shortcoming by combining the gas-side  
242 description of Demekhin (1981) with a WRIBL representation of the liquid film. However,  
243 their liquid-side WRIBL model was developed only up to first order in the long-wave  
244 parameter, and, thus, in conjunction with the linear gas-side approach, the gas pressure  $P_G$   
245 did not enter the problem. We will show that this changes the linear response of the liquid film  
246 qualitatively in our configuration, and that a second-order liquid-side WRIBL development,  
247 accounting for  $P_G$ , is needed to accurately capture the effect of the counter-current gas flow.

248 Such a liquid-side treatment was applied by Samanta (2014), but the author made several  
249 simplifications in the gas-side description, i.e.  $P_G$  was neglected altogether, and  $T_G$  was  
250 assumed constant. The latter assumption entails that the gas-induced stabilization observed  
251 in superconfined falling liquid films (Lavalle *et al.* 2019), which relies on the linear response  
252 of  $T_G$ , cannot be captured.

253 Camassa *et al.* (2017) accounted for variations in  $P_G$  and  $T_G$  in their gas-side description.  
254 Moreover, their gas-side description relies on a long-wave rather than a low-amplitude  
255 expansion of the RANS equations, and, thus, finite confinement levels can be studied.  
256 However, their description of the liquid film relied on the lubrication approach. Thus, the  
257 inertia-driven Kapitza instability, which is responsible for generating long waves in our  
258 configuration but was irrelevant in theirs, cannot be captured.

259 By coupling the gas-side approach of Camassa *et al.* (2017) with a second-order WRIBL  
260 description of the liquid film, our WRIBL-LW model remedies the different limitations  
261 discussed above. Our model is aimed at moderate confinement levels, where the gas flow  
262 is turbulent and the gas pressure is relevant. In that sense, it complements the model  
263 of Dietze & Ruyer-Quil (2013), for superconfined laminar liquid-gas flows, and those of  
264 Demekhin (1981) and Tseluiko & Kalliadasis (2011), for weakly-confined falling liquid films  
265 sheared by a turbulent gas flow, where the effect of  $P_G$  is negligible. For completeness, we  
266 point out that our model does not rely on the quasi-laminar assumption (Alekseenko *et al.*  
267 2009; Trifonov 2010a; Tseluiko & Kalliadasis 2011; Vellingiri *et al.* 2015). We will show  
268 that it accurately predicts the dynamics of Kapitza waves under the effect of a counter-current  
269 turbulent gas flow, in good agreement with experiments.

270 Our manuscript is structured as follows. In §2, we introduce our experimental setup  
271 for studying surface waves in gas-sheared falling liquid films. In §3, we present our low-  
272 dimensional WRIBL-LW model (subsections 3.1 and 3.2), and the numerical methods  
273 underlying our linear and nonlinear computations therewith (subsection 3.4). Section 4  
274 concerns linear stability calculations based on the full RANS equations in the gas, where  
275 the liquid-side description is based either on the WRIBL model (subsection 4.1) or on the  
276 full Navier-Stokes equations (subsection 4.2). Section 6 presents our results concerning the  
277 gas-effect on linear and nonlinear wave dynamics. We first focus on waves resulting from  
278 the long-wave Kapitza instability (subsection 6.1), and then discuss upward-travelling short-  
279 wave ripples (subsection 6.2). Conclusions are drawn in §7, followed by appendices A and  
280 B, containing validation results.



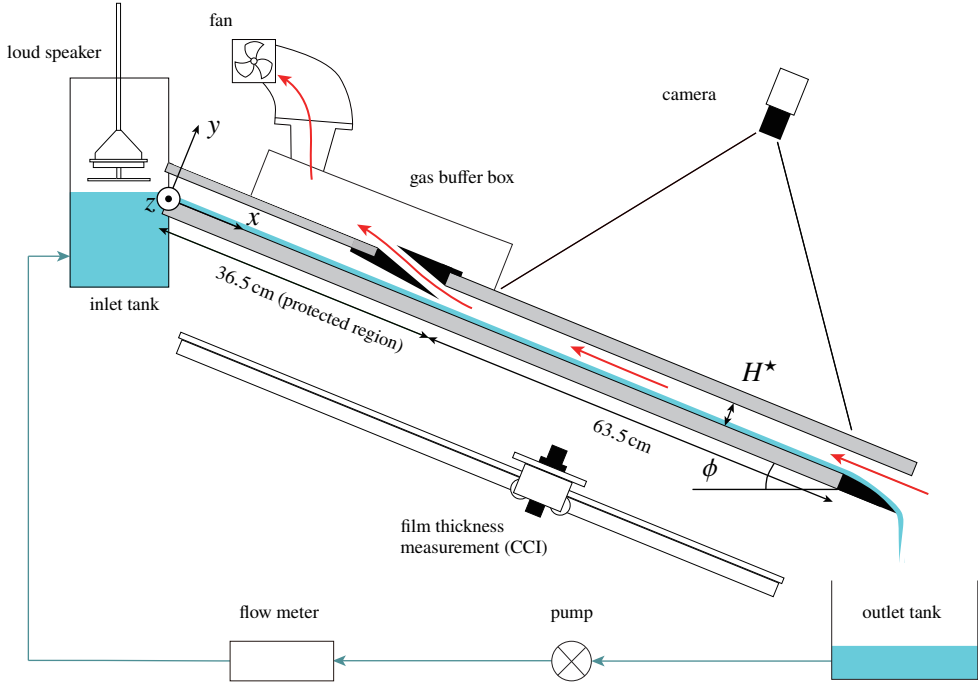


Figure 1: Sketch of our experimental setup. A falling liquid film of water flows down a glass plate inclined at an angle  $\phi=5^\circ$  and enters in contact with a counter-current turbulent air flow within a rectangular channel of height  $H^*=13$  mm and width  $W^*=27$  mm. A loudspeaker is used to force Kapitza waves on the surface of the liquid film, which grow and saturate within a protected region of the setup.

## 281 2. Experiments

282 Figure 1 sketches the setup used for our experiments. A liquid film (index L) of water flows  
 283 down a glass plate inclined at  $\phi=5^\circ$ , and enters into contact with a counter-current turbulent  
 284 gas flow (index G) of air confined within a rectangular channel of height  $H^*=13$  mm and  
 285 width  $W^*=27$  cm. This setup is a slightly modified version of the setup used in the work of  
 286 Mergui *et al.* (2023), where  $H^*=5$  mm and the gas flow was laminar.

287 The liquid flow rate  $q_L^*$  is controlled through a gear pump and measured with an error of  
 288  $\pm 3\%$  using a conductance flow meter (IFM electronic, SM6000). In the current manuscript,  
 289 we focus on two liquid-side regimes:  $Re_L \sim 33$  and  $Re_L \sim 45$ . A loudspeaker integrated into  
 290 the upstream liquid reservoir enables the forcing of Kapitza waves with prescribed frequency  
 291  $f_0^*$  on the surface of the liquid film. These waves are allowed to grow and saturate within a  
 292 protected region spanning from  $x^*=0$  to  $x^*=36.5$  cm, before entering the gas-sheared  
 293 section of the setup ( $36.5 \text{ cm} \leq x^* \leq 100 \text{ cm}$ ). In our experiments,  $f_0^*$  is chosen such as to maximize  
 294 the linear growth rate of the Kapitza waves, yielding a train of regular waves within the  
 295 protected region. Also, the forcing amplitude is adjusted so that the waves reach a saturated  
 296 amplitude before entering the gas-sheared section.

297 The gas flow rate  $q_G^*$  is controlled through a fan, and quantified via a calibration curve  
 298 (relating the fan power to  $q_G^*$ ) obtained from gas velocity measurements in the dry channel.  
 299 Details of the procedure are given in Mergui *et al.* (2023). An error on  $Re_G$  of 3% was  
 300 estimated for all our experiments. For a given liquid flow rate, the fan power was varied from  
 301 zero up until breakdown of the experiment due to flooding, when liquid droplets accumulated  
 302 in the gas buffer box. At zero fan power, the gas is subject to an aerostatic pressure drop,



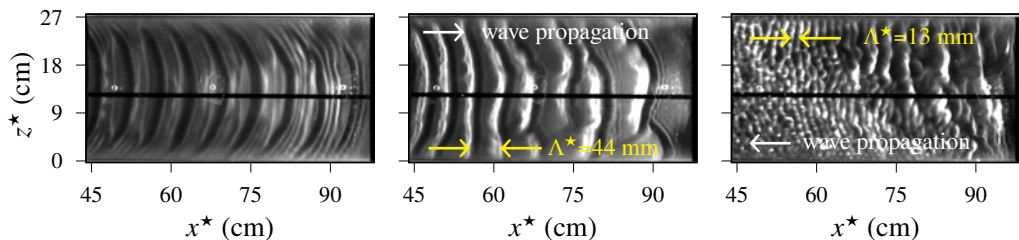


Figure 2: Transition of the wavy falling liquid film under a counter-current gas flow: water/air,  $Re_L^{as}=44.7$ ,  $Re_L=43.1$ ,  $f_0^*=3$  Hz. Shadowgraphs of the liquid-gas interface for increasingly strong fan power. Left: zero fan power (aerostatic configuration), regularly-spaced Kapitzza waves; middle:  $Re_G=-5830$ , coalescence of Kapitzza waves; right:  $Re_G=-6760$ , coexistence of Kapitzza waves with upward-travelling short ripples.

303 which is imposed by the quiescent ambient air. In this case, which we will designate as  
 304 *aerostatic configuration*, the gas flows downward under the shearing action of the falling  
 305 liquid film, i.e.  $q_G^* > 0$ . Conversely, in the case of a counter-current gas flow, we have  $q_G^* < 0$ .  
 306 Thus, we consider  $q_G^*$ , and the gas Reynolds number  $Re_G$ , as signed quantities.

307 In our counter-current experimental runs,  $Re_G$  was typically varied from  $Re_G=-3000$  to  
 308  $Re_G=-6800$ , after an initial measurement under aerostatic conditions. Due to evaporation, the  
 309 liquid temperature typically decreased by a few Kelvin between the aerostatic and counter-  
 310 current configurations. As  $q_L^*$  remained fixed during each run, a corresponding variation of  
 311  $Re_L$  occurred due to changes in the fluid properties. To account for this, we have monitored  
 312 the liquid temperature  $T_{inlet}$  in the inlet tank over the course of each experiment, using a  
 313 thermocouple. The temperature decrease was observed as soon as the counter-current air  
 314 flow was imposed, but the temperature varied little upon increasing the gas flow rate after  
 315 that. Thus, when reporting experimental data, we will give  $Re_L^{as}$ , which corresponds to the  
 316 aerostatic configuration, and  $Re_L$ , which corresponds to the counter-current configuration.

317 Representative values of the density and kinematic viscosity of water and air for our  
 318 counter-current experiments ( $T_{inlet} \approx 19^\circ\text{C}$ ) are  $\rho_L=998.3$  kg/m<sup>3</sup>,  $\nu_L=1.03 \times 10^{-6}$  m<sup>2</sup>/s, and  
 319  $\rho_G=1.21$  kg/m<sup>3</sup>,  $\nu_G=14.9 \times 10^{-6}$  m<sup>2</sup>/s. The surface tension of our water was measured once  
 320 and for all at  $T=19.9^\circ\text{C}$  with a Drop Shape Analyzer (Krüss), yielding  $\sigma=71$  mN m<sup>-1</sup>. Based  
 321 on this, we obtain  $Ka=\sigma/\rho_L/\nu_L^{4/3}/g^{1/3}=3174$  for the Kapitzza number. Conversely, for our  
 322 experiments in the aerostatic configuration ( $T_{inlet} \approx 21^\circ\text{C}$ ), we obtain  $Ka=3394$ .

323 Two methods were applied to characterize the gas-effect on the dynamics of nonlinear sur-  
 324 face waves (see Kofman *et al.* (2014) and Mergui *et al.* (2023) for details): (1) shadowgraphy  
 325 of the wavy liquid-gas interface, using an sCMOS camera (PCO, pco.edge 5.5) with 100 Hz  
 326 framerate; (2) pointwise measurements of the film thickness time trace, using a confocal  
 327 chromatic imaging (CCI) technique (Cohen-Sabban *et al.* 2001; Lel *et al.* 2005) with 400 Hz  
 328 acquisition frequency and an accuracy of  $\pm 1$   $\mu\text{m}$  (Stil S.A., CL-MG CL4 line sensor).

329 Figures 2 and 3 show typical data obtained with these two methods. Figure 2 represents  
 330 shadowgraphs for an experiment, where the fan power was increased step by step (from left  
 331 to right panel), while maintaining  $q_L^*$  and  $f_0^*=3$  Hz fixed. Each shadowgraph represents the  
 332 entire width of the channel and almost the entire length of the gas-sheared section of the setup,  
 333 i.e.  $44 \text{ cm} \leq x^* \leq 100 \text{ cm}$ . At zero fan power (leftmost panel), regularly-spaced Kapitzza waves  
 334 with quasi-two-dimensional wave fronts are observed. Applying and increasing a counter-  
 335 current gas flow rate, first causes coalescence events (middle panel), and then the emergence  
 336 of upward-travelling short ripples that coexist with the long Kapitzza waves (rightmost panel).  
 337 This dynamics will be the focus of section 6.

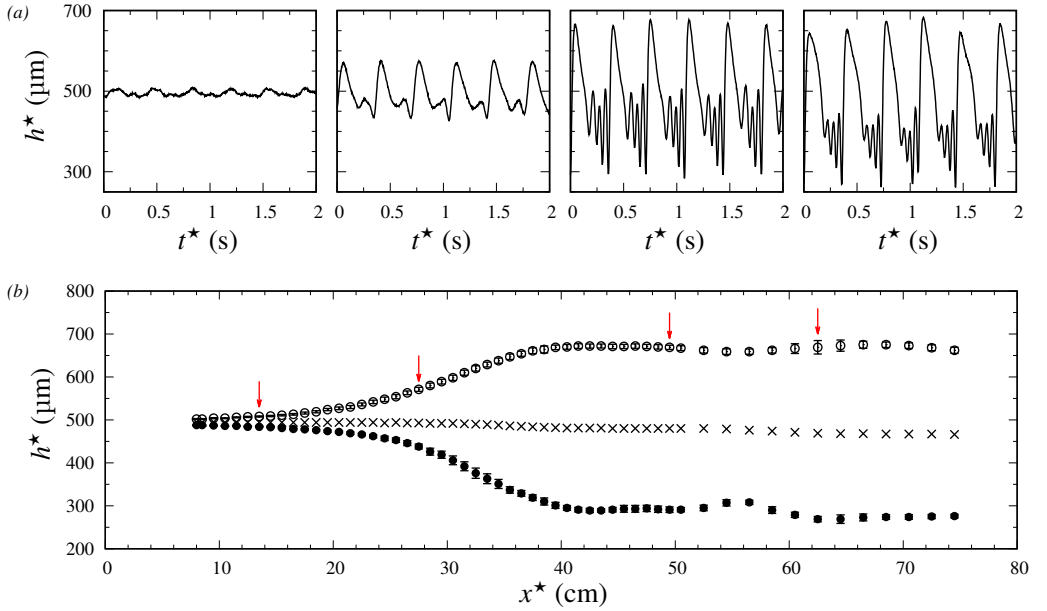


Figure 3: Typical CCI film thickness measurements in the aerostatic configuration: water/air,  $Re_L^{as}=33.7$ ,  $f_0^*=2.8$  Hz. (a) Film thickness time traces measured at different positions. From left to right:  $x^*=13.5$  cm, 27.5 cm, 49.5 cm, and 62.5 cm; (b) spatial profiles of averaged quantities (at least 100 waves). Open/filled circles: ensemble-averaged wave height  $h_{max}^*$  and minimum film thickness  $h_{min}^*$ , crosses: time-averaged film thickness  $\bar{h}^*$ . Error bars indicate standard deviation and red arrows mark positions for panel a.

338 Figure 3 represents measurement data obtained with the CCI technique for the aerostatic  
 339 configuration at  $Re_L^{as}=33.7$  and  $f_0^*=2.8$  Hz. In panel 3a, we have plotted time traces of the  
 340 film thickness  $h^*$  at streamwise positions representative for the regimes of linear growth,  
 341 nonlinear growth, and saturation of Kapitza waves. These time traces evidence the formation  
 342 of characteristic precursory capillary ripples. Panel 3b represents spatial profiles of the  
 343 ensemble-averaged (over at least 100 waves) maximum film thickness  $h_{max}^*$ , minimum film  
 344 thickness  $h_{min}^*$ , and time-averaged (over at least 100 wave periods) film thickness  $\bar{h}^*$ . Error  
 345 bars illustrate the standard deviation. To obtain these profiles, the CCI probe was displaced  
 346 incrementally using a rail (figure 1).

### 347 3. Low-dimensional WRIBL-LW model

348 We consider the flow in figure 4. A two-dimensional laminar falling liquid film of thickness  
 349  $h(x, t)$  flows along an inclined plane under the action of gravity, while being sheared by a  
 350 counter-current turbulent gas flow. The gas flow is confined by a second wall at  $y^*=H^*$  (the  
 351 star superscript denotes dimensional quantities throughout), which is not represented. We  
 352 impose a symmetry condition at the center line of the average gas layer, i.e.  $y^*=D^*$ . In the  
 353 case of a symmetrical vertical configuration with liquid films lining both walls (Vlachos *et al.*  
 354 2001), this condition is satisfied analytically, and we have  $D^*=H^*/2$ . In the case of an  
 355 inclined configuration with a dry upper wall, which is the one considered here, the symmetry  
 356 condition remains a reasonable approximation, provided the liquid holdup  $\bar{h}^*/H^*$ , where  
 357  $\bar{h}^*$  designates the average film thickness, is not too large. In the current work,  $\bar{h}^*/H^*<0.1$ ,  
 358 and thus the symmetry condition is acceptable. In that case,  $D^*=(H^*+\bar{h}^*)/2$ . Moreover, due

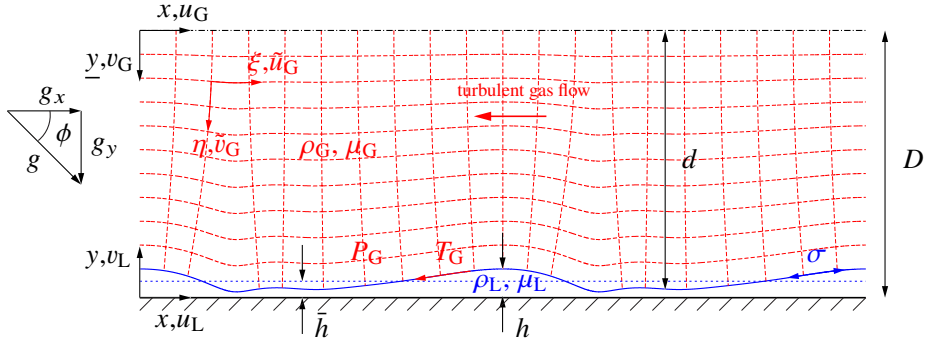


Figure 4: Falling liquid film (subscript L) on an inclined wall subject to a counter-current turbulent gas flow (subscript G). The flow is confined by an upper wall (not shown) at  $y^*=H^*$  (stars denote dimensional quantities) and a symmetry condition is imposed at the center line of the average gas layer  $y^*=D^*$ . Gas-liquid coupling is expressed via the tangential gas shear stress  $T_G$  and the gas pressure  $P_G$  at the film surface  $y^*=h^*$ . Red dashed lines illustrate orthogonal curvilinear coordinate system  $(\eta, \xi)$ , where  $\eta=y\bar{d}/d$ .

359 to the inter-phase coupling conditions we will apply in our gas-side description (frozen-  
 360 interface assumption) and the nature of our calculations (linear stability analysis and long-  
 361 wave asymptotic expansion), the symmetry condition at  $y^*=D^*$  holds analytically, even when  
 362 the upper wall is dry. This will be further explained in sections 3.2 and 4.1.

363 Following previous works (Halpern & Grotberg 2003; Tseluiko & Kalliadasis 2011;  
 364 Samanta 2014; Camassa *et al.* 2017), we relax the inter-phase coupling conditions and apply  
 365 a weakly-coupled treatment of the two-phase flow. The liquid film (section 3.1) is modelled  
 366 with the WRIBL method (Kalliadasis *et al.* 2012), where the effect of the gas enters via the  
 367 tangential gas shear stress  $T_G$  and the gas pressure  $P_G$  acting at the film surface  $y^*=h^*$  (figure  
 368 4), neglecting the normal gaseous viscous stress. These inter-phase coupling quantities  
 369 are obtained from the gas-side model (section 3.2), which is derived via long-wave (LW)  
 370 asymptotic expansion, following Camassa *et al.* (2017).

### 371 3.1. Liquid-side WRIBL model

372 The liquid film (subscript L), with density  $\rho_L$ , dynamic viscosity  $\mu_L$ , and surface tension  $\sigma$ ,  
 373 is governed by the dimensionless continuity and Navier-Stokes equations written in Cartesian  
 374 coordinates  $x$  and  $y$  (figure 4):

$$375 \quad \partial_x u_L + \partial_y v_L = 0, \quad (3.1a)$$

$$377 \quad \epsilon(\partial_t u_L + u_L \partial_x u_L + v_L \partial_y u_L) = -\epsilon \partial_x p + \frac{1}{\text{Re}_L} (\epsilon^2 \partial_{xx} u_L + \partial_{yy} u_L) + \frac{\sin(\phi)}{\text{Fr}^2}, \quad (3.1b)$$

$$379 \quad \epsilon^3(\partial_t v_L + u_L \partial_x v_L + v_L \partial_y v_L) = -\epsilon \partial_y p_L + \frac{1}{\text{Re}_L} (\epsilon^4 \partial_{xx} v_L + \epsilon^2 \partial_{yy} v_L) - \epsilon \frac{\cos(\phi)}{\text{Fr}^2}, \quad (3.1c)$$

380 where  $\text{Re}_L = \rho_L \mathcal{U}_L \mathcal{L} / \mu_L$  and  $\text{Fr} = \mathcal{U}_L / \sqrt{\mathcal{L}g}$  denote the liquid Reynolds number and Froude  
 381 number, and where we have applied the following scaling:

$$382 \quad u_L = \frac{u_L^*}{\mathcal{U}_L}, \quad v_L = \frac{v_L^*}{\epsilon \mathcal{U}_L}, \quad x = \epsilon \frac{x^*}{\mathcal{L}}, \quad y = \frac{y^*}{\mathcal{L}}, \quad t = \epsilon t^* \frac{\mathcal{U}_L}{\mathcal{L}}, \quad p_L = \frac{p_L^*}{\rho_L \mathcal{U}_L^2}. \quad (3.1d)$$

383 Here, we have introduced the long-wave parameter  $\epsilon = \mathcal{L} / \Lambda^*$ , which relates the cross-stream  
 384 length scale  $\mathcal{L}$  to the streamwise length scale given by the wavelength  $\Lambda^*$ . For the purpose  
 385 of the current derivation, it suffices to say that the scales  $\mathcal{L}$  and  $\mathcal{U}_L$  are representative of

386 the film thickness  $h^*$  and streamwise liquid velocity  $u_L^*$ . In section 3.3, we will rescale our  
387 problem and make the final choice for  $\mathcal{L}$  and  $\mathcal{U}_L$ .

388 The system is closed with the boundary conditions at  $y=0$ :

$$389 \quad u_L = v_L = 0, \quad (3.1e)$$

390 the kinematic condition:

$$391 \quad v_L|_{y=h} = u_L|_{y=h} \partial_x h + \partial_t h, \quad (3.1f)$$

392 and the inter-phase stress coupling conditions at  $y=h$ :

$$393 \quad -\partial_y u_L \frac{1}{1 + \epsilon^2 \partial_x h^2} (-\epsilon^4 \partial_x h^2 \partial_x v_L - 4\epsilon^2 \partial_x h \partial_x u_L + \epsilon^2 \partial_x v_L) = \frac{\Pi_\mu \Pi_u}{\Pi_L} T_G, \quad (3.1g)$$

395

$$396 \quad \epsilon P_L + \frac{2}{1 + \epsilon^2 \partial_x h^2} \frac{1}{\text{Re}_L} (\epsilon^4 \partial_x h^2 \partial_x u_L - \epsilon^4 \partial_x h \partial_x v_L - \epsilon^2 \partial_x u_L - \epsilon^2 \partial_x h \partial_y u_L) \\ - \epsilon^3 \text{We} \partial_{xx} h = \frac{1}{\text{Re}_G} \frac{\Pi_\rho \Pi_u^2}{\Pi_L} P_G, \quad (3.1h)$$

397 where  $\text{We} = \sigma / \rho_L / \mathcal{L} / \mathcal{U}_L^2$  denotes the Weber number. The liquid-gas coupling enters through  
398  $T_G$  and  $P_G$ , which are scaled as follows:

$$399 \quad T_G = \frac{\mathcal{L}_G}{\mu_G \mathcal{U}_G} T_G^*, \quad P_G = \frac{\epsilon}{\mu_G \mathcal{U}_G} P_G^*, \quad (3.2)$$

400 where  $\mathcal{L}_G$ ,  $\mathcal{U}_G$ , and  $\epsilon = \mathcal{L}_G / \Lambda^* = \epsilon \Pi_L$  denote the gas-side cross-stream length scale, velocity  
401 scale, and long-wave parameter, which will be defined in section 3.2. As a result, the gas  
402 Reynolds number  $\text{Re}_G = \rho_G \mathcal{U}_G \mathcal{L}_G / \mu_G$ , the velocity scale ratio  $\Pi_u = \mathcal{U}_G / \mathcal{U}_L$ , the length scale  
403 ratio  $\Pi_L = \mathcal{L}_G / \mathcal{L}$ , and the viscosity and density ratios  $\Pi_\mu = \mu_G / \mu_L$  and  $\Pi_\rho = \rho_G / \rho_L$  enter (3.1g)  
404 and (3.1h).

405 Next, we apply the WRIBL approach to derive two evolution equations involving the local  
406 instantaneous liquid flow rate  $q(x, t)$  and the film thickness  $h(x, t)$ . In principle, we follow  
407 the same steps as Samanta (2014), only that we account for the gas pressure  $P_G$ , which plays  
408 an important role in our current configuration, allow  $P_G$  and  $T_G$  to vary in space and time,  
409 and account for turbulence in the gas.

410 First, the governing equations (3.1) are truncated at  $\mathcal{O}(\epsilon^2)$ , except for inertial terms, which  
411 are truncated at  $\mathcal{O}(\text{Re}_L \epsilon)$ . Next, we eliminate  $p$  from (3.1b) via an integrated form of (3.1c)  
412 using (3.1h). Then, we substitute for the streamwise velocity  $u$  ( $v$  is obtained from equation  
413 3.1a) the following decomposition:

$$414 \quad u_L = \hat{u}_L + \epsilon u_L^{(1)}, \quad (3.3)$$

415 where the base profile  $\hat{u}_L$  is governed by:

$$416 \quad \partial_{yy} \hat{u}_L = \text{const.}, \quad \partial_y \hat{u}_L|_{y=h} = \frac{\Pi_\mu \Pi_u}{\Pi_L} T_G, \quad \hat{u}_L|_{y=0} = 0, \quad (3.4) \\ \int_0^{h(x,t)} \hat{u}_L dy = q_L(x, t).$$

417 Finally, the unknown  $\mathcal{O}(\epsilon)$  velocity correction  $\epsilon u_L^{(1)}$  is eliminated from the problem by  
418 multiplying the truncated form of (3.1b) with a weight function  $w(y)$ , integrating the result  
419 across the film thickness  $h(x, t)$ , and applying the tangential inter-phase coupling condition

420 (3.1g). The weight function  $w$  satisfies:

$$421 \quad \partial_{yy}w = \text{const.}, \quad w|_{y=0} = 0, \quad \partial_y w|_{y=h} = 0. \quad (3.5)$$

423 As a final result, we obtain the integral momentum equation for the liquid film:

$$\begin{aligned}
 \partial_t q_L + \frac{17}{7} \frac{q_L}{h} \partial_x q_L - \frac{9}{7} \frac{q_L^2}{h^2} \partial_x h &= \frac{5}{6} \text{We} h \partial_{xxx} h + \frac{5}{6} \text{Fr}^{-2} h \{ \sin(\phi) - \cos(\phi) \partial_x h \} \\
 &+ \text{Re}_L^{-1} \left\{ -\frac{5}{2} \frac{q_L}{h^2} + 4 \frac{q_L}{h^2} \partial_x h^2 - \frac{9}{2h} \partial_x q_L \partial_x h - 6 \frac{q_L}{h} \partial_{xx} h + \frac{9}{2} \partial_{xx} q_L \right\} \\
 &+ \frac{\Pi_\mu \Pi_u}{\Pi_L} T_G \left\{ \text{Re}_L^{-1} \left[ \frac{5}{4} + \frac{h}{6} \partial_{xx} h + \frac{1}{2} \partial_x h^2 \right] - \frac{5}{112} q_L \partial_x h - \frac{19}{336} \partial_x q_L h \right\} \\
 &- \frac{19}{672} \frac{\Pi_\mu^2 \Pi_u^2}{\Pi_L^2} h^2 \partial_x h T_G^2 - \frac{5}{6} \text{Re}_G^{-1} \frac{\Pi_\rho \Pi_u^2}{\Pi_L} h \partial_x P_G \\
 &+ \frac{\Pi_\mu \Pi_u}{\Pi_L} \left\{ \partial_x T_G \left[ \text{Re}_L^{-1} \frac{3}{4} h \partial_x h - \frac{15}{224} h q_L \right] - \frac{25}{1344} \frac{\Pi_\mu \Pi_u}{\Pi_L} h^3 T_G \partial_x T_G - \frac{h^2}{48} \partial_t T_G \right\}, \quad (3.6a)
 \end{aligned}$$

425 to which is added an integral continuity equation obtained by integrating (3.1a) across the  
426 liquid film and applying (3.1f):

$$427 \quad \partial_t h + \partial_x q_L = 0. \quad (3.6b)$$

428 In the limit  $T_G = \partial_x P_G = 0$ , (3.6a) reduces to equation (41) from Ruyer-Quil & Manneville  
429 (2000). In the limit  $\partial_x T_G = \partial_t T_G = \partial_x P_G = 0$ , it collapses with equation (3.9) from Samanta  
430 (2014), except for a typo in the  $T_G \partial_x h^2$  term of that reference. Here, we will neglect the terms  
431 involving  $\partial_x T_G$  and  $\partial_t T_G$ , but we will account for the space and time variation of  $T_G(x, t)$  and  
432  $P_G(x, t)$  in the remaining terms. This amounts to a quasi-developed approach. **See appendix**  
433 **C for a justification of this approximation.**

434 Versus the model of Tseluiko & Kalliadasis (2011), which is based on a linear repre-  
435 sentation of the gas response, our model accounts for the gas pressure  $P_G$ , which plays a  
436 role for the confinement considered here. It also accounts for streamwise viscous diffusion  
437 in the liquid, which is known to affect the dynamics of precursory capillary ripples  
438 (Ruyer-Quil & Manneville 2002).

### 439 3.2. Gas-side asymptotic long-wave (LW) model

440 We represent the turbulent flow of the gas (subscript G), with density  $\rho_G$  and dynamic  
441 viscosity  $\mu_G$ , in two dimensions via the (dimensionless) Reynolds-averaged continuity and  
442 steady Navier-Stokes (RANS) equations, written here in the Cartesian gas-side coordinates  
443  $x$  and  $\underline{y}$  (see figure 4):

$$444 \quad \partial_x u_G + \partial_{\underline{y}} v_G = 0, \quad (3.7)$$

$$\begin{aligned}
 446 \quad \underline{\epsilon} (u_G \partial_x u_G + v_G \partial_{\underline{y}} u_G) &= -\frac{1}{\text{Re}_G} \partial_x P_G + \frac{\Pi_L}{\Pi_u^2} \frac{\sin(\phi)}{\text{Fr}^2} + \frac{1}{\text{Re}_G} \left\{ \partial_{\underline{y}\underline{y}} u_G + \underline{\epsilon}^2 \partial_{xx} u_G \right\} \\
 447 \quad &+ \frac{1}{\text{Re}_G} \left\{ \partial_{\underline{y}} \left( \frac{\mu_t}{\mu_G} \partial_{\underline{y}} u_G \right) + \underline{\epsilon}^2 \partial_x \left( \frac{\mu_t}{\mu_G} \partial_x u_G \right) \right\}, \quad (3.8a)
 \end{aligned}$$

448 
$$\underline{\epsilon}^3 (u_G \partial_x v_G + v_G \partial_y v_G) = - \frac{1}{\text{Re}_G} \partial_y p_G + \underline{\epsilon} \frac{\Pi_L \cos(\phi)}{\Pi_u^2 \text{Fr}^2} + \frac{1}{\text{Re}_G} \left\{ \underline{\epsilon}^2 \partial_{yy} v_G + \underline{\epsilon}^4 \partial_{xx} v_G \right\} \quad (3.8b)$$

449 
$$+ \frac{1}{\text{Re}_G} \left\{ \underline{\epsilon}^2 \partial_y \left( \frac{\mu_t}{\mu_G} \partial_y v_G \right) + \underline{\epsilon}^4 \partial_x \left( \frac{\mu_t}{\mu_G} \partial_x v_G \right) \right\},$$

450

451 where  $\mu_t$  denotes the turbulent viscosity,  $\text{Re}_G = \rho_G \mathcal{U}_G \mathcal{L}_G / \mu_G$  is the gas Reynolds number,  
 452 and where we have applied the following scaling:

453 
$$u_G = \frac{u_G^*}{\mathcal{U}_G}, \quad v_G = \frac{v_G^*}{\underline{\epsilon} \mathcal{U}_G}, \quad x = \underline{\epsilon} \frac{x^*}{\mathcal{L}_G}, \quad y = \frac{y^*}{\mathcal{L}_G}, \quad p_G = p_G^* \frac{\underline{\epsilon} \mathcal{L}_G}{\mu_G \mathcal{U}_G}, \quad (3.9)$$

454 introducing the gas-side long-wave parameter  $\underline{\epsilon} = \mathcal{L}_G / \Lambda^*$ . For the gas-side reference scales,  
 455 we choose once and for all:

456 
$$\mathcal{L}_G = H^*, \quad \mathcal{U}_G = \frac{q_{G0}^*}{H^*}, \quad (3.10)$$

457 where  $q_{G0}^*$  is the nominal gas flow rate per unit width of the primary flow (subscript 0), and,  
 458 thus,  $\mathcal{U}_G$  corresponds to the superficial gas velocity. We have scaled pressure with a measure  
 459 for the viscous shear stress, in contrast to (3.1d), where the dynamic pressure was used.

460 The turbulent viscosity  $\mu_t$  is formulated via the mixing-length approach (Prandtl 1925):

461 
$$\frac{\mu_t}{\mu_G} = \text{Re}_G l_t^2 \left| \partial_y u_G \right|, \quad (3.11)$$

462 where  $l_t = l_t^* / \mathcal{L}_G$  denotes the dimensionless mixing length. At this point, a remark about  
 463 choosing a turbulent viscosity model, such as (3.11), is in order. Luchini & Charru (2019)  
 464 have shown that such models cannot fully reproduce the momentum redistribution induced  
 465 by wall perturbations to a parallel turbulent flow. Nonetheless, comparisons with different  
 466 experiments (Zilker *et al.* 1977; Frederick & Hanratty 1988) have shown that turbulent-  
 467 viscosity models based on the van Driest equation, which will be introduced in (3.22), capture  
 468 satisfactorily the linear (Russo & Luchini 2016) and nonlinear (Tseluiko & Kalliadasis 2011;  
 469 Camassa *et al.* 2017) responses of the wall shear stress. Thus, such models allow to adequately  
 470 account for the inter-phase coupling in our current configuration.

471 We assume a large gas/liquid velocity contrast  $\Pi_u \gg 1$ , which warrants two simplifications.  
 472 First, we have neglected time derivatives in (3.8), as:

473 
$$O \left\{ \frac{\partial_t u_G^*}{u_G^* \partial_x u_G^*} \right\} = \frac{1}{\Pi_u} \ll 1, \quad (3.12)$$

474 assuming that the time scale is dictated by the waviness of the liquid film, i.e.  $\mathcal{T} = \Lambda^* / \mathcal{U}_L$ .  
 475 Second, we set zero-velocity conditions at the film surface  $y=d$ :

476 
$$u_G = v_G = 0. \quad (3.13a)$$

477 Thus, from the point of view of the gas, the film surface is represented as a frozen wavy wall  
 478 (Tseluiko & Kalliadasis 2011). Our system is closed via a symmetry condition at  $y=0$ :

479 
$$\partial_y u_G = v_G = 0. \quad (3.13b)$$

480 The ultimate aim of the gas-side model, to be derived next, is to obtain the inter-phase  
 481 coupling quantities in (3.6a), which are evaluated at  $y=d$ , implying  $l_t=0$ :

482 
$$P_G = p_G, \quad (3.14a)$$

484

$$T_G = \frac{T_G^*}{\mu_G \mathcal{U}_G / \mathcal{L}_G} = -\partial_{\underline{y}} u_G - \{\epsilon^2 \partial_x d^2 - 1\}^{-1} \left\{ 2\epsilon^2 \partial_x d \partial_{\underline{y}} v_G \right. \\ \left. + 2\epsilon^2 \partial_x d \partial_x u_G + \epsilon^2 \partial_x v_G - \epsilon^4 \partial_x d^2 \partial_x v_G \right\}. \quad (3.14b)$$

486

487

Following Camassa *et al.* (2017), we introduce the curvilinear coordinates  $\eta$  and  $\xi$  (see figure 4), which will facilitate the account of turbulence:

488

$$\eta = \frac{\bar{d}}{d} y, \quad \xi = x + \underline{\epsilon} F(\xi, \eta), \quad (3.15)$$

489

where  $\bar{d}$  denotes the spatial average of  $d$ , and where orthogonality implies:

490

$$\partial_\eta F = \underline{\epsilon} \frac{d}{\bar{d}^2} \partial_\xi d \frac{1}{\underline{\epsilon} \partial_\xi F - 1}. \quad (3.16)$$

491

Red dashed lines in figure 4 represent curves of constant  $\eta$  and  $\xi$ , where:

492

$$\partial_x y \Big|_\eta = -\partial_y x \Big|_\xi = \frac{y}{\bar{d}} \partial_x d. \quad (3.17)$$

493

494

Next, we recast the governing equations (3.8) and (3.13) in the curvilinear coordinate system (tilde symbol), using the projection rules:

495

$$u_G = \tilde{u}_G + O(\underline{\epsilon}^2), \quad v_G = \tilde{v}_G + \frac{\partial_\xi d}{\bar{d}} \eta \tilde{u}_G + O(\underline{\epsilon}), \quad (3.18)$$

496

$$\partial_x = \partial_\xi - \eta \frac{\partial_\xi d}{\bar{d}} \partial_\eta + O(\underline{\epsilon}), \quad \partial_y = \frac{\bar{d}}{d} \partial_\eta + O(\underline{\epsilon}^2), \quad (3.19)$$

497

498

and truncate the result at  $O(\underline{\epsilon}^1)$ . Upon eliminating the pressure variable  $p$  in (3.8a) via an appropriate integration of (3.8b), we obtain:

499

$$\frac{\partial_\xi d}{\bar{d}} \partial_\xi \tilde{u}_G + \partial_\xi \tilde{u}_G + \frac{\bar{d}}{d} \partial_\eta \tilde{v}_G = 0, \quad (3.20a)$$

501

$$\underline{\epsilon} \tilde{u}_G \partial_\xi \tilde{u}_G + \underline{\epsilon} \frac{\bar{d}}{d} \tilde{v}_G \partial_\eta \tilde{u}_G = -\frac{1}{\text{Re}_G} \partial_\xi P_G + \frac{\Pi_L}{\Pi_u^2} \frac{1}{\text{Fr}^2} (\sin(\phi) + \underline{\epsilon} \cos(\phi) \partial_\xi d) \\ + \frac{1}{\text{Re}_G} \frac{\bar{d}^2}{d^2} \left\{ \partial_{\eta\eta} \tilde{u}_G + \partial_\eta \left[ \frac{\tilde{\mu}_t}{\mu_G} \partial_\eta \tilde{u}_G \right] \right\}, \quad (3.20b)$$

502

503

where  $P_G = p_G|_{\eta=\bar{d}}$ , and  $\tilde{\mu}_t$  satisfies:

504

$$\frac{\tilde{\mu}_t}{\mu_G} = \frac{d}{\bar{d}} \text{Re}_G \tilde{l}_t^2 |\partial_\eta \tilde{u}_G|, \quad (3.21)$$

505

with  $\tilde{l}_t = l_t \bar{d} / d$ .

506

507

508

509

In this curvilinear formulation, the variation of the mixing length  $\tilde{l}_t$  is expressed in terms of  $\eta$ , i.e. normal to the film surface, and thus correlations for parallel flows can be used. Following Tseluiko & Kalliadasis (2011), we employ the van Driest equation (Van Driest 1956):

510

$$\tilde{l}_t = \kappa (\bar{d} - \eta) \left\{ 1 - \exp \left[ \sqrt{|T_{G0}|} \frac{\text{Re}_G}{A} (\eta - \bar{d}) \right] \right\}, \quad (3.22)$$

511

where  $A=26$ ,  $\kappa=0.41$  is the von Karman constant, and  $T_{G0}$  denotes the primary-flow tangential



512 stress, obtained by evaluating (3.30) in the limit  $\underline{\epsilon}=0$ , which intervenes in the traditional  
513 scaling based on the friction velocity  $\mathcal{U}^+$ :

$$514 \quad \mathcal{U}^+ = \{\rho_G^{-1} |T_{G0}^*|\}^{\frac{1}{2}}, \quad \mathcal{L}^+ = \frac{\mu_G}{\rho_G \mathcal{U}^+}. \quad (3.23)$$

515 Finally, the boundary conditions (3.13) become:

$$516 \quad \tilde{u}_G|_{\eta=\bar{d}} = \tilde{v}_G|_{\eta=\bar{d}} = 0, \quad \partial_\eta \tilde{u}_G|_{\eta=0} = \tilde{v}_G|_{\eta=0} = 0. \quad (3.24)$$

517 The BVP given by (3.20) and (3.24) is solved order by order based on a regular expansion  
518 in  $\underline{\epsilon}$  around  $\underline{\epsilon}=0$  (Camassa *et al.* 2017):

$$519 \quad \tilde{u}_G = \tilde{u}_G^{(0)} + \underline{\epsilon} \tilde{u}_G^{(1)} + O(\underline{\epsilon}^2), \quad (3.25a)$$

$$520 \quad \tilde{v}_G = \tilde{v}_G^{(0)} + \underline{\epsilon} \tilde{v}_G^{(1)} + O(\underline{\epsilon}^2), \quad (3.25b)$$

$$521 \quad P_G = P_G^{(0)} + \underline{\epsilon} P_G^{(1)} + O(\underline{\epsilon}^2). \quad (3.25c)$$

523 The zeroth-order problem is obtained by inserting (3.25a) into (3.20) and (3.24) and then  
524 truncating at  $O(\underline{\epsilon}^0)$ . We anticipate a solution in the form of the product ansatz:

$$525 \quad \tilde{u}_G^{(0)} = g_0(\xi) U_0(\eta) = \frac{\bar{d}}{d} U_0(\eta), \quad (3.26)$$

526 which leads to the variable-separated zeroth-order momentum equation:

$$\frac{d^3}{\bar{d}^3} \left\{ \frac{1}{\text{Re}_G} \partial_\xi P_G^{(0)} - \frac{\Pi_L}{\Pi_u^2} \frac{1}{\text{Fr}^2} \sin(\phi) \right\} = \frac{1}{\text{Re}_G} \partial_{\eta\eta} U_0 + \partial_\eta \left\{ \tilde{l}_r^2 \text{sgn}(\partial_\eta U_0) (\partial_\eta U_0)^2 \right\} = C_0, \quad (3.27a)$$

528 subject to the boundary conditions:

$$529 \quad U_0|_{\eta=\bar{d}} = \partial_\eta U_0|_{\eta=0} = 0, \quad (3.27b)$$

530 where we have employed the signum function  $\text{sgn}$  to substitute  $|\partial_\eta U_0| = \text{sgn}(\partial_\eta U_0) \partial_\eta U_0$ ,  
531 and where the separation constant  $C_0$  is obtained from the gauge condition:

$$532 \quad \int_0^{\bar{d}} \tilde{u}_G^{(0)} d\bar{y} = \int_0^{\bar{d}} U_0 d\eta = \frac{q_{G0}}{2} = \frac{1}{2}. \quad (3.27c)$$

534 At the next order, i.e.  $O(\underline{\epsilon}^1)$ , we obtain in a similar way:

$$\frac{d^2}{\bar{d}^2} \left\{ \frac{1}{\text{Re}_G} \partial_\xi P_G^{(1)} \frac{d}{\partial_\xi d} - \frac{\Pi_L}{\Pi_u^2} \frac{1}{\text{Fr}^2} \cos(\phi) d \right\} = U_0^2 + \frac{1}{\text{Re}_G} \partial_{\eta\eta} U_1$$

$$535 \quad + \partial_\eta \left\{ \tilde{l}_r^2 \text{sgn}(\partial_\eta U_0) \partial_\eta U_0 \partial_\eta U_1 \right\} = C_1, \quad (3.28a)$$

536

$$537 \quad U_1|_{\eta=\bar{d}} = \partial_\eta U_1|_{\eta=0} = 0, \quad (3.28b)$$

538

$$539 \quad \int_0^{\bar{d}} \tilde{u}_G^{(1)} d\bar{y} = \int_0^{\bar{d}} U_1 d\eta = 0, \quad (3.28c)$$

540 where we have employed the product ansatz:

$$541 \quad \tilde{u}_G^{(1)} = g_1(\xi) U_1(\eta) = \frac{\partial_\xi d}{d} U_1(\eta), \quad (3.29)$$

542 and where the separation constant  $C_1$  is obtained from (3.28c).

543 The two BVPs (3.27) and (3.28) are solved numerically for  $U_0$ ,  $U_1$ ,  $C_0$ , and  $C_1$  via the  
544 continuation software `Auto07P` (Doedel 2008). The solution is obtained for a given  $\bar{d}$  on  
545 a fixed domain spanning  $0 \leq \eta \leq \bar{d}$ . Based on this, the coupling quantities  $T_G$  and  $\partial_x P_G$ ,  
546 which appear in the liquid-side model (3.6a), are readily constructed at  $O(\underline{\epsilon}^1)$ :

$$547 \quad T_G = -\frac{\bar{d}}{d} \partial_\eta \tilde{u}_G \Big|_{\eta=\bar{d}} + O(\underline{\epsilon}^2) = -\frac{\bar{d}}{d} \left\{ \partial_\eta \tilde{u}_G^{(0)} \Big|_{\eta=\bar{d}} + \underline{\epsilon} \partial_\eta \tilde{u}_G^{(1)} \Big|_{\eta=\bar{d}} \right\} + O(\underline{\epsilon}^2), \quad (3.30a)$$

$$548 \quad = -\frac{\bar{d}^2}{d^2} \left\{ \partial_\eta U_0 \Big|_{\eta=\bar{d}} + \frac{\partial_{x^*} d^*}{\bar{d}} \partial_\eta U_1 \Big|_{\eta=\bar{d}} \right\} + O(\underline{\epsilon}^2),$$

$$549 \quad \partial_x P_G = \partial_\xi P_G^{(0)} + \underline{\epsilon} \partial_\xi P_G^{(1)} + O(\underline{\epsilon}^2) \quad (3.30b)$$

$$550 \quad = \text{Re}_G \left\{ \frac{\bar{d}^3}{d^3} \left( C_0 + C_1 \frac{\partial_{x^*} d^*}{\bar{d}} \right) + \frac{\Pi_L}{\Pi_u^2} \frac{1}{\text{Fr}^2} (\sin(\phi) + \cos(\phi) \partial_{x^*} d^*) \right\} + O(\underline{\epsilon}^2),$$

552 where we have used the velocity expansion (3.25a):

$$553 \quad \tilde{u}_G = \frac{\bar{d}}{d} U_0 + \frac{\partial_{x^*} d^*}{d} U_1 + O(\underline{\epsilon}^2). \quad (3.31)$$

554 Importantly, at fixed  $\bar{d}$ ,  $T_G$  and  $\partial_x P_G$  (3.30) depend only on  $d=D-h/\Pi_L$ , which varies with  $x$   
555 and  $t$ . By contrast, Samanta (2014) assumed  $T_G=\text{const}$  and  $\partial_x P_G=0$ .

556 In contrast to the gas-side description of Demekhin (1981) and Tseluiko & Kalliadasis  
557 (2011), (3.30) is obtained from a long-wave and not from a small-wave-amplitude expansion.  
558 Thus, it works better when the liquid holdup is larger, whereas the cited models work better  
559 when the liquid holdup is small, i.e.  $h^*/\bar{d}^* \rightarrow 0$ .

560 As a result of our frozen-interface assumption ( $\Pi_u \gg 1$ ) expressed via (3.13), one would  
561 obtain exactly the same relations for the functions  $U_0$  and  $U_1$  appearing in (3.30), should  
562 one apply no slip and no penetration conditions at  $y^*=H^*$  instead of a symmetry condition  
563 at  $y^*=D^*$ . This is because the BVPs for  $U_0$  (3.27) and  $U_1$  (3.28) would remain symmetrical  
564 in that case. Thus, up to the order of expansion of our WRIBL-LW model, our symmetry  
565 condition (3.13b) is valid without loss of generality.

### 566 3.3. Rescaling

567 For the remainder of the manuscript, we rescale streamwise lengths by setting  $\epsilon=\underline{\epsilon}=1$ , and  
568 we choose:

$$569 \quad \mathcal{L} = \mathcal{L}_G = H^*, \quad \mathcal{U}_L = \frac{q_{L0}^*}{H^*}, \quad \mathcal{U}_G = \frac{q_{G0}^*}{H^*}. \quad (3.32)$$

570 This implies  $\Pi_L=1$ , i.e. all lengths are now scaled with the channel height  $H^*$ . We recall that  
571  $q_{L0}^*$  and  $q_{G0}^*$  are the primary-flow liquid and gas flow rates per unit width, and, thus,  $\mathcal{U}_L$  and  
572  $\mathcal{U}_G$  are the superficial velocities. The corresponding Reynolds numbers are:

$$573 \quad \text{Re}_L = \frac{q_{L0}^*}{\nu_L}, \quad \text{Re}_G = \frac{q_{G0}^*}{\nu_G}, \quad (3.33)$$

574 where  $\nu_L=\mu_L/\rho_L$  and  $\nu_G=\mu_G/\rho_G$ .

575 At some places, we will rescale quantities with the natural scales:

$$576 \quad \mathcal{L}_\nu = \nu_L^{2/3} g^{-1/3}, \quad \mathcal{U}_\nu = (\nu_L g)^{1/3}, \quad \mathcal{T}_\nu = \frac{\mathcal{L}_\nu}{\mathcal{U}_\nu} = \nu_L^{1/3} g^{-2/3}. \quad (3.34)$$

577

## 3.4. Model computations

578 We perform three types of numerical computations based on our WRIBL-LW model (3.6),  
 579 (3.30): linear stability calculations, nonlinear computations of travelling-wave solutions  
 580 (TWS), and nonlinear computations of spatially-evolving falling liquid films.

581 To obtain the linear stability formulation, we perturb the dependent variables  $q_L$  and  $h$   
 582 around their primary flow values  $q_{L0}$  and  $h_0$ :

$$583 \quad q_L = q_{L0} + \check{q}_L(x, t) = q_0 + \hat{q} \exp\{i(kx - \omega t)\}, \quad (3.35a)$$

$$584 \quad h = h_0 + \check{h}(x, t) = h_0 + \hat{h} \exp\{i(kx - \omega t)\}, \quad (3.35b)$$

585 where the check mark denotes infinitesimal perturbations,  $\omega$  denotes the angular frequency,  
 586 and  $\hat{q}_L = \hat{h}\omega/k$  follows from (3.6b). Surface waves resulting from the Kapitza instability grow  
 587 spatially, but a counter-current gas flow can cause the onset of absolute instability (AI). Both  
 588 phenomena can be captured via a spatial stability formulation (Vellingiri *et al.* 2015). Thus,  
 589 we will usually (but not exclusively) assume  $k \in \mathbb{C}$  and  $\omega \in \mathbb{R}$ , with:

$$590 \quad k = k_r + ik_i, \quad (3.36)$$

591 where  $k_r = 2\pi/\Lambda$  is the physical wavenumber and  $-k_i$  is the spatial growth rate.

592 The film surface perturbation (3.35b) translates to the gas-side problem via:

$$593 \quad d = d_0 + \check{d} = d_0 + \hat{d} \exp\{i(kx - \omega t)\}, \quad \hat{d} = -\frac{\hat{h}}{\Pi_L}. \quad (3.37)$$

594 Inserting this in (3.30) and then linearizing, yields the linear responses of the inter-phase  
 595 coupling quantities:

$$596 \quad T_G = T_{G0} + \check{T}_G = T_{G0} + \hat{T}_G \exp\{i(kx - \omega t)\}, \quad (3.38a)$$

$$597 \quad P_G = P_{G0} + \check{P}_G = P_{G0} + \hat{P}_G \exp\{i(kx - \omega t)\}, \quad (3.38b)$$

599 with:

$$600 \quad T_{G0} = -\partial_\eta U_0|_{d_0}, \quad \hat{T}_G = \frac{\hat{d}}{d_0} \left\{ 2 \partial_\eta U_0|_{d_0} + \Pi_L ik \partial_\eta U_1|_{d_0} \right\}, \quad (3.39)$$

601

$$602 \quad \partial_x P_{G0} = \text{Re}_G \left\{ C_0 + \frac{\Pi_L \sin(\phi)}{\Pi_u^2 \text{Fr}^2} \right\}, \quad \hat{P}_G = -\text{Re}_G \frac{\hat{d}}{ik} \left\{ 3 \frac{C_0}{d_0} - \Pi_L \frac{C_1}{d_0} - \frac{\Pi_L^2 \cos(\phi)}{\Pi_u^2 \text{Fr}^2} \right\}. \quad (3.40)$$

603

603 Introducing (3.35) and (3.38) into (3.6), and linearizing once again, yields the dispersion  
 605 relation for the spatial stability problem:

$$606 \quad \text{DR} = -i\omega^2 + ik\omega \frac{17}{7} \frac{q_{L0}}{h_0} - ik^2 \frac{9}{7} \frac{q_{L0}^2}{h_0^2} + \frac{5}{6} \text{Fr}^{-2} \left\{ ik^2 \cos(\phi) h_0 - k \sin(\phi) \right\}$$

$$- i^3 k^4 \frac{5}{6} \text{We} h_0 + \frac{5}{2} \frac{1}{\text{Re}_L} \frac{1}{h_0^2} \left\{ \omega - k \frac{2q_{L0}}{h_0} \right\} + i^2 k^3 \frac{6}{\text{Re}_L} \frac{q_{L0}}{h_0} - i^2 k^2 \omega \frac{9}{2} \frac{1}{\text{Re}_L}$$

$$+ \frac{\Pi_\mu \Pi_u}{\Pi_L} \left\{ T_{G0} \left[ ik\omega \frac{19}{336} h_0 - i^2 k^3 \frac{1}{6} \frac{1}{\text{Re}_L} h_0 + ik^2 \frac{5}{112} q_{L0} \right] + k \frac{5}{4} \frac{1}{\text{Re}_L} \frac{1}{\Pi_L} \frac{\hat{T}_G}{\hat{d}} \right\}$$

$$+ ik^2 \frac{19}{672} \frac{\Pi_\mu^2 \Pi_u^2}{\Pi_L^2} h_0^2 T_{G0}^2 + k \frac{5}{6} \frac{\Pi_\rho \Pi_u^2}{\Pi_L} \frac{1}{\text{Re}_G} \left\{ \partial_x P_{G0} - \frac{h_0}{\Pi_L} ik \frac{\hat{P}_G}{\hat{d}} \right\} = 0, \quad (3.41)$$

607 where  $\hat{d}$  will cancel, due to  $\hat{T}_G \propto \hat{d}$  and  $\hat{P}_G \propto \hat{d}$  according to (3.39) and (3.40).

608 To compute nonlinear travelling-wave solutions (TWS), we recast (3.6a) into an ODE in  
609 terms of the wave coordinate  $\gamma = x - ct$ :

$$610 \quad h''' = \text{NL}(h, h', h''; \bar{h}, c, q_L^{\text{MF}}), \quad (3.42a)$$

$$611 \quad q_L^{\text{MF}} = q_L - hc = \bar{q}_L - \bar{h}c, \quad (3.42b)$$

612 where primes denote differentiation w.r.t.  $\gamma$ , bars signify averaging over the wavelength  
613  $\Lambda$  in terms of  $\gamma$ ,  $c$  denotes the nonlinear wave speed, and the subscript MF refers to the  
614 moving reference frame. Further, (3.42b) is the integral form of (3.6b), which we have used  
615 to eliminate  $q$  from (3.42a). The system is closed through periodicity boundary conditions:

$$616 \quad h^{(j)} \Big|_{\gamma=0} = h^{(j)} \Big|_{\gamma=\Lambda}, \quad j = 0, 1, 2, \quad (3.42c)$$

617 and it is solved for a fixed value of  $\bar{q}_L$ , enforced through the integral condition:

$$618 \quad \Lambda^{-1} \int_0^\Lambda q_L d\gamma = \bar{q}_L. \quad (3.43)$$

619 We do this numerically via the continuation software `Auto07P`, after recasting (3.42a) into a  
620 dynamical system. First, we continue the fixed-point solutions ( $h' = h'' = h''' = 0$ ) of (3.42a) at  
621  $q_L = q_{L0}$  and  $h = h_0$  in terms of  $c$ , until reaching the Hopf bifurcation of the Kapitza instability.  
622 Then, starting from this point, periodic solutions are continued in terms of a selected control  
623 parameter, e.g. the liquid Reynolds number  $\text{Re}_L$ . The BVPs associated with the turbulent gas  
624 flow, (3.27) and (3.28), are solved simultaneously. In addition, we solve the linear dispersion  
625 relation (3.41) for the spatially most-amplified angular frequency  $\omega_{\max}$ :

$$627 \quad \text{DR}(\omega_{\max}, k) = 0, \quad \partial_\omega k_i \Big|_{\omega=\omega_{\max}} = 0. \quad (3.44)$$

628 By imposing  $f = f_{\max} = \omega_{\max}/2\pi$ , TWS most-likely to emerge in an experiment can be tracked.

629 To compute the spatial evolution of nonlinear Kapitza waves, we solve (3.6a) and (3.6b)  
630 numerically on an open domain with inlet/outlet conditions. Details of the numerical scheme  
631 are given in appendix F3 of Kalliadasis *et al.* (2012). In particular, we apply a second-  
632 order central-differences spatial discretization and a quasi-linearized Crank-Nicolson time  
633 integration. At the liquid outlet, we impose the soft boundary conditions of Richard *et al.*  
634 (2016). At the liquid inlet, we explicitly prescribe  $h$  and  $q$  at the first two grid points ( $i_x = 1, 2$ ),  
635 based on the primary flow:

$$636 \quad h \Big|_{i_x=1} = h \Big|_{i_x=2} = h_0, \quad (3.45a)$$

$$637 \quad q_L \Big|_{i_x=1} = q_L \Big|_{i_x=2} = q_{L0} [1 + F(t)], \quad (3.45b)$$

639 where the function  $F(t)$  allows to apply a tailored inlet forcing:

$$640 \quad F(t) = \varepsilon_1 \sin(2\pi f t) + \varepsilon_2 \sum_{k=1}^N \sin(2\pi k \Delta f t + \varphi_{\text{rand}}), \quad \Delta f = 2 f_c / N. \quad (3.46)$$

641 The first term in (3.46) constitutes a harmonic perturbation of frequency  $f$  and the second  
642 one mimics white noise through a series of  $N=1000$  Fourier modes that are shifted by a  
643 random phase shift  $\varphi_{\text{rand}} = \varphi_{\text{rand}}(k) \in [0, 2\pi]$  and that span a frequency range of twice the  
644 linear cut-off frequency  $f_c$  (Chang *et al.* 1996a). When  $\varepsilon_1 = 0$ , the inlet perturbation consists  
645 of only white noise. This setting will be used to simulate the natural, noise-driven, evolution  
646 of a wavy film as it would occur in a real system. In other computations, we will apply  
647 additional coherent inlet forcing by setting  $\varepsilon_1 > 0$ .

#### 648 4. Linear stability analysis based on full RANS equations

649 The long-wave asymptotic expansion underlying the gas-side representation (3.30) in our  
 650 WRIBL-LW model is truncated at order  $\underline{\epsilon}^1$ , whereas our liquid-side representation (3.6) is  
 651 consistent up to order  $\epsilon^2$ . To validate linear stability predictions based on this model, and  
 652 to go beyond its limitations, we introduce two linear stability formulations that are based on  
 653 the full RANS equations in the gas (4.3). The first formulation (section 4.1) relies on the  
 654 WRIBL model in the liquid (3.6), and we designate this approach as WRIBL-OS, where OS  
 655 refers to the Orr-Sommerfeld equation. The second formulation (section 4.2) relies on the  
 656 full Navier-Stokes equations in the liquid (3.1), and we designate that approach as OS-OS.

##### 657 4.1. WRIBL-OS approach

658 In our WRIBL-OS approach, the linear response of the liquid film is governed by the  
 659 dispersion relation (3.41), but the perturbation amplitudes  $\hat{T}_G$  and  $\hat{P}_G$  are now obtained from  
 660 the full (steady) RANS equations (3.8). For this, we recast (3.8) in terms of the curvilinear  
 661 coordinates (3.15) and introduce the gas stream function  $\Psi$ :

$$662 \quad \tilde{u} = \frac{\hat{d}}{d} \partial_\eta \Psi, \quad \tilde{v} = -\partial_\xi \Psi, \quad (4.1)$$

663 which we perturb, along with  $p_G$  and  $d$ , around the primary flow (subscript 0):

$$664 \quad \Psi = \Psi_0 + \check{\Psi} = \Psi_0 + \psi(\eta) \exp \{i(k\xi - \omega t)\}, \quad (4.2a)$$

$$665 \quad p_G = p_{G0} + \check{p}_G = p_{G0} + \hat{p}_G(\eta) \exp \{i(k\xi - \omega t)\}, \quad (4.2b)$$

$$666 \quad d = d_0 + \check{d} = d_0 + \hat{d} \exp \{i(k\xi - \omega t)\}, \quad (4.2c)$$

668 where  $k = k_r \in \mathbb{R}$ , and the time dependence is included formally to account for the the  
 669 unsteadiness of the liquid film. Upon linearization and subtraction of the primary flow,  
 671 we obtain the linearized curvilinear RANS equations in  $\xi$ -direction:

$$672 \quad \text{OS}_\xi : \quad \text{Re}_G ik \left\{ \psi' \Psi_0' - \frac{\hat{d}}{d_0} \Psi_0'' - \psi \Psi_0'' \right\} + \text{Re}_G \tilde{l}_t |\Psi_0''| \left\{ \tilde{l}_t' \left[ k^2 \left( -2\psi + 3 \frac{\hat{d}}{d_0} \eta \Psi_0' \right) - 4\psi'' \right. \right. \\ \left. \left. + 6 \frac{\hat{d}}{d_0} \Psi_0'' \right] + \tilde{l}_t \left[ -2\psi''' + 6 \frac{\hat{d}}{d_0} \Psi_0''' - 2 \frac{\Psi_0''''}{\Psi_0''} \psi'' + k^2 \left( -\psi' + \frac{3}{2} \frac{\hat{d}}{d_0} \Psi_0' + \frac{3}{2} \frac{\hat{d}}{d_0} \eta \Psi_0'' \right. \right. \right. \\ \left. \left. \left. - \frac{\Psi_0''''}{\Psi_0''} \psi + \frac{3}{2} \frac{\hat{d}}{d_0} \eta \frac{\Psi_0'''' \Psi_0'}{\Psi_0''} \right) \right] \right\} = -ik \hat{p}_G + \psi''' - 3 \frac{\hat{d}}{d_0} \Psi_0''' - k^2 \left\{ \psi' - \frac{\hat{d}}{d_0} \Psi_0' - \frac{\hat{d}}{d_0} \eta \Psi_0'' \right\}, \quad (4.3a)$$

674 and in  $\eta$  direction:

$$675 \quad \text{OS}_\eta : \quad \text{Re}_G k^2 \left\{ \psi \Psi_0' - \frac{\hat{d}}{d_0} \eta \Psi_0'^2 \right\} + \text{Re}_G \tilde{l}_t |\Psi_0''| ik \left\{ 2\tilde{l}_t' \frac{\hat{d}}{d_0} \eta \Psi_0'' + \tilde{l}_t \left[ -2\psi'' + 2 \frac{\hat{d}}{d_0} \Psi_0'' \right. \right. \\ \left. \left. + 2\eta \frac{\hat{d}}{d_0} \Psi_0''' + k^2 \left( -\psi + \frac{3}{2} \frac{\hat{d}}{d_0} \eta \Psi_0' \right) \right] \right\} = -\hat{p}'_G - ik^3 \left\{ -\psi + \frac{\hat{d}}{d_0} \eta \Psi_0' \right\} \\ - ik \left\{ \psi'' - 2 \frac{\hat{d}}{d_0} \Psi_0'' - \frac{\hat{d}}{d_0} \eta \Psi_0''' \right\}, \quad (4.3b)$$

676 where primes denote differentiation w.r.t.  $\eta$ . The pressure perturbation amplitude  $\hat{p}_G$  can be  
677 removed from (4.3a) and (4.3b) via:

$$678 \quad \text{OS} : \quad \partial_\eta \text{OS}_\xi - ik \text{OS}_\eta, \quad (4.3c)$$

679 where OS is the final gas-side Orr-Sommerfeld equation, involving only  $\psi$  and its derivatives.  
680 The problem is closed with the boundary conditions (3.24):

$$681 \quad \psi''|_{\eta=0} = 0, \quad \psi|_{\eta=0} = 0, \quad \psi'|_{\eta=d_0} = 0, \quad \psi|_{\eta=d_0} = 0. \quad (4.3d)$$

682 We solve (4.3) numerically for  $\psi$  with the continuation software Auto07P, starting from  
683 the analytically tractable laminar long-wave limit ( $\tilde{l}_t=k=0$ ). The amplitudes of the linear  
684 perturbations of the inter-phase coupling quantities:

$$685 \quad \check{T}_G = \hat{T}_G \exp \{i(k\xi - \omega t)\}, \quad \check{P}_G = \hat{P}_G \exp \{i(k\xi - \omega t)\}, \quad (4.4)$$

686 can be readily obtained by recasting (3.14) in curvilinear coordinates, inserting (4.2), and  
687 linearizing:

$$688 \quad \hat{T}_G = -\psi''|_{\eta=d_0} + 2\frac{\hat{d}}{d_0} \Psi_0''|_{\eta=d_0}, \quad (4.5a)$$

689

$$690 \quad ik\hat{P}_G = \left\{ \psi'''|_{\eta=d_0} - 3\frac{\hat{d}}{d_0} \Psi_0'''|_{\eta=d_0} + k^2\hat{d} \Psi_0''|_{\eta=d_0} \right\}. \quad (4.5b)$$

691 We point out that  $\psi \propto \hat{d}$  and, thus,  $\hat{d}$  once again cancels from (3.41), as it should. Also, the  
692 spatial variations prescribed in (3.37) and (4.2) are equivalent in the linear limit  $\hat{d} \rightarrow 0$ ,  
693 where the curvilinear coordinates collapse with the Cartesian ones. Thus,  $\partial_x \check{P}_G = \partial_\xi \check{P}_G$ .

694 Panels 5a and 5b represent spatial linear stability predictions obtained with our WRIBL-  
695 OS approach, based on (3.41) and (4.3c), for parameters according to the experiments of  
696 Kofman *et al.* (2017) in an  $H^*=19$  mm channel. According to panel 5a, the maximum of the  
697 growth rate dispersion curve increases with increasing counter-current gas flow rate, up until  
698 forming a pinch point at  $\text{Re}_G=-8490$ , where the AI limit is reached (curve with crosses).

699 This destabilization of the liquid film is caused by the inter-phase pressure coupling, as can  
700 be deduced by confronting panel 5a with panel 5b, where we have represented corresponding  
701 growth rate curves in the limit  $\Pi_\rho=0$ . In that case, the gas-effect enters only via  $T_G$ , and we  
702 observe a stabilization of the liquid film at large  $|\text{Re}_G|$  (compare crosses and pentagons).  
703 Models that do not account for the gas pressure  $P_G$ , e.g. the weak-confinement first-order  
704 WRIBL model of Tseluiko & Kalliadasis (2011), may thus give qualitatively incorrect linear  
705 stability predictions for the current configuration. The same observation also holds at weaker  
706 confinement, as shown by confronting panels 5c and 5d, where we have chosen  $H^*=40$  mm.

707 As a result of our frozen-interface assumption ( $\Pi_u \gg 1$ ) expressed through the last two  
708 equations in (4.3d), one would obtain exactly the same linear stability problem (4.3) should  
709 one apply no slip and no penetration conditions at  $y^*=H^*$  instead of a symmetry condition  
710 at  $y^*=D^*$ . This is because the primary gas flow would remain symmetrical about the center  
711 line of the gas layer. Thus, for all linear stability calculations based on the gas-side OS BVP  
712 (4.3), our symmetry condition (4.3d) is valid analytically.

713

#### 4.2. OS-OS approach

714 Linear stability calculations based on our WRIBL-LW and WRIBL-OS approaches may be  
715 limited to long-wave instability modes. To capture short-wave instability modes (section 6.2),  
716 we introduce a stability formulation based on the full Navier-Stokes equations (3.1) in the  
717 liquid and the full RANS equations (4.3) in the gas.

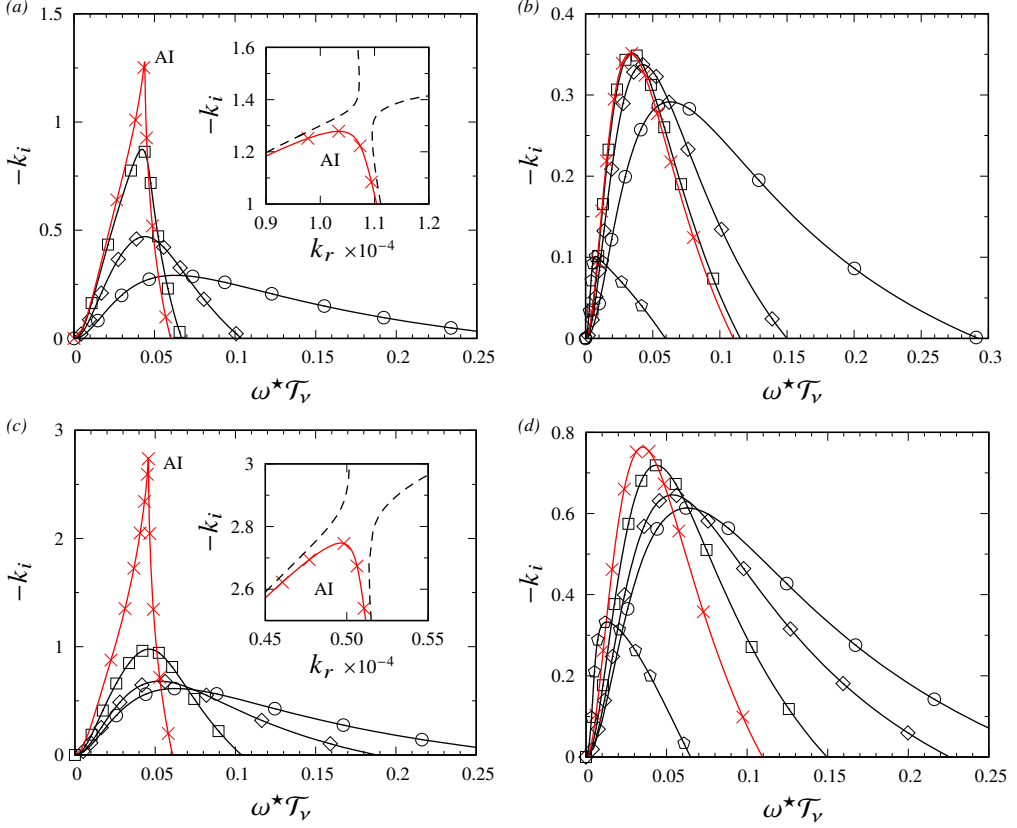


Figure 5: Spatial linear stability calculations with WRIBL-OS approach. Parameters based on experiments of Kofman *et al.* (2017):  $Ka=3174$  (water and air I in table 1),  $\phi=5^\circ$ ,  $Re_L=45$ . Circles: passive-gas limit,  $\Pi_\rho=\Pi_\mu=0$  in (3.41).  $|Re_G|$  increases in the order: [diamonds, squares, crosses, pentagons]. (a,c) Full model; (b,d)  $\Pi_\rho=0$  in (3.41). (a,b)  $H^*=19$  mm; (c,d)  $H^*=40$  mm. (a)  $Re_G=[-6234, -8145, -8490$  (AI)]. Dashed:  $Re_G=-8500$ ; (b)  $Re_G=[-6234, -8145, -8490, -15000]$ ; (c)  $Re_G=[-8145, -15000, -20430$  (AI limit)]. Dashed:  $Re_G=-20440$ ; (d)  $Re_G=[-8145, -15000, -20430, -35000]$ . We have rescaled  $\omega$  with  $\mathcal{T}_v=2.207 \times 10^{-3}$  s (3.34).

718 The gas-side linear response is governed by the same equations as in the WRIBL-OS  
 719 approach, i.e. (4.3) and (4.5), and we focus here on deriving those governing the liquid-side  
 720 linear response. For this, we perturb the film thickness as:

$$721 \quad h = h_0 + \check{h} = h_0 + \hat{h} \exp \{ ik(x - ct) \}, \quad (4.6)$$

722 assuming a temporal stability formulation this time, i.e.  $k \in \mathbb{R}$  and  $c=c_r + i c_i \in \mathbb{C}$ , where  $c_r$   
 723 denotes the wave speed and  $kc_i$  the temporal growth rate.

724 We start with the full governing equations (3.1). Considering these in the limit of fully  
 725 developed flow with  $h=h_0$ , yields the liquid primary flow:

$$726 \quad u_{L0} = \frac{1}{2} Re_L \left\{ \Pi_\rho \partial_x p_{G0} - \frac{\sin(\phi)}{Fr^2} \right\} (y^2 - 2yh_0) + \frac{\Pi_\mu \Pi_u}{\Pi_L} T_{G0} y, \quad (4.7a)$$

727

$$728 \quad \partial_y p_{L0} = -\frac{\cos(\phi)}{Fr^2}. \quad (4.7b)$$



Fluids	$\rho$ (kg/m <sup>3</sup> )	$\nu$ (m <sup>2</sup> /s)	$\sigma$ (N/m)	Ka	$T$ (°C)	figures
Water	998.3	$1.03 \cdot 10^{-6}$	0.071	3174	19	5, 6, 8, 9, 11-13,
Air I	1.209	$14.9 \cdot 10^{-6}$	-	-	19	18-21, 24-27
DMSO(83%)-water	1098.3	$2.85 \times 10^{-6}$	0.0484	509.5	25	22, 23
Glycerol(54%)-water	1000	$2.3 \times 10^{-6}$	0.0626	963	22	7
Air II	1.185	$15.6 \cdot 10^{-6}$	-	-	25	7, 22, 23
Methanol	791	$0.73 \cdot 10^{-6}$	0.022	1988	25	28, 29a
Helium	0.165	$12.1 \cdot 10^{-5}$	-	-	25	

Table 1: Fluid combinations used in our computations. The Kapitza number is defined as  $Ka = \sigma / \rho_L / g^{1/3} / \nu_L^{1/3}$ , where  $\sigma$ ,  $\rho_L$ , and  $\nu_L$  denote the surface tension, density and kinematic viscosity of the liquid, and  $g$  designates the gravitational acceleration.

729 Next, we introduce the liquid stream function  $\Phi$ :

$$730 \quad u_L = \partial_y \Phi, \quad v_L = -\partial_x \Phi, \quad (4.8)$$

731 which we perturb around the primary flow:

$$732 \quad \Phi = \Phi_0 + \check{\Phi} = \Phi_0 + \phi(y) \exp \{ik(x - ct)\}. \quad (4.9)$$

733 Substituting (4.8) and (4.9) into (3.1), linearizing w.r.t.  $\check{\Phi}$ , subtracting the primary flow, and  
734 applying standard manipulations, we obtain the liquid-side Orr-Sommerfeld equation:

$$735 \quad \phi^{iv} - 2k^2 \phi'' + k^4 \phi = ik \text{Re}_L \left\{ (c - u_{L0}) (k^2 \phi - \phi'') - \phi u''_{L0} \right\}, \quad (4.10a)$$

736 the boundary conditions at  $y=0$ :

$$737 \quad \phi'' = \phi = 0, \quad (4.10b)$$

738 and the inter-phase coupling conditions at  $y=h_0$ :

$$739 \quad \phi u''_{L0} + \tilde{c} \{ \phi'' + k^2 \phi \} = \Pi_\mu \Pi_u \tilde{c} \hat{T}_G, \quad (4.10c)$$

$$742 \quad -\frac{1}{\text{Re}_L} \{ 2k^2 \phi u'_{L0} + \tilde{c} [3k^2 \phi' - \phi'''] \} - ik \tilde{c} \{ -\tilde{c} \phi' - \phi u_{L0} \} \quad (4.10d)$$

$$+ ik \phi p'_{L0} = ik \frac{\Pi_\rho \Pi_u^2}{\text{Re}_G} \tilde{c} \hat{P}_G + ik^3 \text{We} \phi,$$

743 where primes denote differentiation w.r.t.  $y$ , and where we have introduced  $\tilde{c} = c - u_{L0}|_{y=h_0}$ .

744 The non-linearity involving  $\tilde{c}$  in (4.10d) can be eliminated via (4.10c). Further,  $\hat{T}_G$  and  $\hat{P}_G$   
745 are rescaled versions of the amplitudes in (4.5):

$$746 \quad \hat{T}_G = -\hat{h} \frac{\hat{T}_G}{\hat{d}}, \quad \hat{P}_G = \hat{h} \frac{\hat{P}_G}{\hat{d}}, \quad (4.11)$$

747 where  $\hat{d}$  is an arbitrary deflection amplitude used in the solution of the gas-side problem  
748 (4.3), and  $\hat{h}$  is directly linked to  $\phi$  via the kinematic condition (3.1f):

$$749 \quad \hat{h} = \frac{\phi|_{y=h_0}}{\tilde{c}}. \quad (4.12)$$

750 The rescaling in (4.11) allows to solve the gas- and liquid-side problems sequentially.

751 We solve the two-phase BVP comprising (4.3) and (4.10) by expanding the stream  
 752 function amplitudes  $\phi$  and  $\psi$  in terms of Chebyshev polynomials (Boomkamp *et al.* 1997;  
 753 Barmak *et al.* 2016b):

$$754 \quad \phi(\zeta) = c_{L0} + \sum_{j=1}^{N_p} c_{1j} T_j(\zeta), \quad \psi(\zeta) = c_{G0} + \sum_{j=1}^{N_p} c_{gj} T_j(\zeta), \quad (4.13)$$

755 where  $T_j$  are  $j$ th-degree Chebyshev polynomials of the first kind, defined on the interval  
 756  $\zeta \in [-1, 1]$ , with:

$$757 \quad \zeta = 2 \frac{y}{h_0} - 1 \quad \text{for } 0 \leq y \leq h_0, \quad (4.14)$$

$$758 \quad \zeta = 1 - 2 \frac{\eta}{d_0} \quad \text{for } 0 \leq \eta \leq d_0. \quad (4.15)$$

760 Thus, there are  $2(N_p + 1)$  unknown coefficients  $c_{kj}$ , which are fixed by the 8 conditions  
 761 in (4.10b), (4.10c), (4.10d), and (4.3d), and  $2(N_p + 1) - 8$  additional constraints obtained by  
 762 evaluating the ODEs (4.10a) and (4.3c) at the inner collocation points  $\zeta_2, \dots, \zeta_{N_p-2}$ , defined  
 763 according to:

$$764 \quad \zeta_i = \cos \left[ \frac{i\pi}{N_p} \right] \quad \forall i \in [0, N_p]. \quad (4.16)$$

765 Instead of solving for the coefficients  $c_{kj}$ , we solve directly for the  $2(N_p + 2)$  unknowns  
 766  $\phi(\zeta_i)$  and  $\psi(\zeta_i)$ , arranged into the solution vectors:

$$767 \quad \boldsymbol{\phi} = [\phi(\zeta_0), \dots, \phi(\zeta_{N_p})]^T, \quad \boldsymbol{\psi} = [\psi(\zeta_0), \dots, \psi(\zeta_{N_p})]^T. \quad (4.17)$$

768 Then, by making use of the Chebyshev differentiation matrix  $\mathbf{D}$  (Trefethen 2000):

$$769 \quad [\phi^{(i)}(\zeta_0), \dots, \phi^{(i)}(\zeta_{N_p})]^T = \mathbf{D}^i [\phi(\zeta_0), \dots, \phi(\zeta_{N_p})]^T, \quad (4.18)$$

$$771 \quad [\psi^{(i)}(\zeta_0), \dots, \psi^{(i)}(\zeta_{N_p})]^T = \mathbf{D}^i [\psi(\zeta_0), \dots, \psi(\zeta_{N_p})]^T, \quad (4.19)$$

772 where  $i=1, 2, 3, 4$ , and  $(i)$  indicates the order of differentiation w.r.t.  $\zeta$ , (4.10) is cast into a  
 773 generalized eigenvalue problem in matrix form:

$$774 \quad \underline{A}\boldsymbol{\phi} = \tilde{c} \underline{B}\boldsymbol{\phi}, \quad (4.20)$$

775 and (4.3) is cast into a linear system of equations:

$$776 \quad \underline{C}\boldsymbol{\psi} = \mathbf{b}, \quad (4.21)$$

777 introducing the coefficient matrices  $\underline{A}$ ,  $\underline{B}$ , and  $\underline{C}$ , and the inhomogeneity  $\mathbf{b}$ . With the help  
 778 of MATLAB (MATLAB 2015), we first solve (4.21) for  $\boldsymbol{\psi}$  by numerical inversion via the /  
 779 operator and then (4.20) for the eigenvalues  $\tilde{c}$  and eigenvectors  $\boldsymbol{\phi}$  via the eig function.

780 Using this approach, the full set of eigenmodes is computed at once. Thus, short-wave  
 781 instability modes, i.e. modes with  $c_i \neq 0$  at  $k=0$ , can be readily obtained. Once a mode has  
 782 been identified at a given wavenumber  $k$ , it can be tracked by advancing  $k$ , using the function  
 783 eig, which searches for eigenvalues in the vicinity of a previous solution.

784 In appendix A, we validate our OS-OS approach, (4.20) and (4.21), versus Vellingiri *et al.*  
 785 (2015) and Schmidt *et al.* (2016). Figure 6 confronts temporal linear stability predictions  
 786 from this approach (solid lines) with predictions from our WRIBL-OS approach (symbols),  
 787 for similar parameters as panel 5a. Agreement is good up to  $|\text{Re}_G| \sim 8000$ . Thus, our liquid-side  
 788 WRIBL description suffices to predict the gas-effect on the long-wave Kapitza instability.

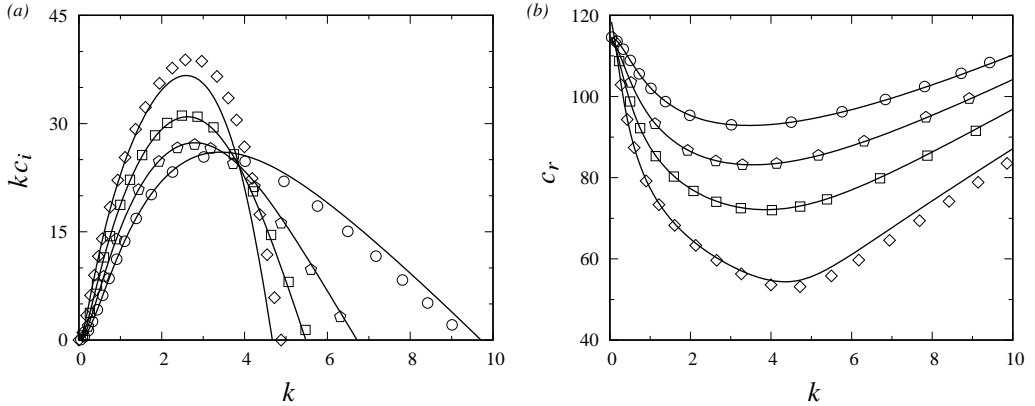


Figure 6: Temporal stability predictions from OS-OS (solid curves) and WRIBL-OS (open symbols) approaches. Similar parameters as in panel 5a:  $Ka=3174$ ,  $H^*=19$  mm,  $\phi=5^\circ$ ,  $Re_L=32.7$ . Circles: passive-gas limit ( $\Pi_\rho=\Pi_\mu=0$  in equation 3.41), pentagons:  $Re_G=4123$ , squares:  $Re_G=6173$ , diamonds:  $Re_G=8220$ . (a) Growth rate; (b) wave speed.

## 789 5. Model validation

790 To evaluate the linear and nonlinear predictions of our WRIBL-LW model, we confront these  
 791 with stability predictions from Vellingiri *et al.* (2015) and Samanta (2014), our own stability  
 792 calculations using the WRIBL-OS approach, and experiments from Kofman (2014).

793 By design, our WRIBL-LW model exactly predicts the neutral linear stability bound of  
 794 the long-wave Kapitza instability. We consider a temporal linear stability formulation and  
 795 expand the complex wave speed  $c=\omega/k$  in terms of  $k\in\mathbb{R}$  around the limit  $k=0$ :

$$796 \quad c = c_0 + kc_1 + O(k^2). \quad (5.1)$$

797 Inserting this into (3.41), and truncating order by order, we obtain  $c_0$  and  $c_1$ :

$$798 \quad c_0 = 2 u_{L0}|_{h_0} + \Pi_\mu \Pi_u T_{G0} \left\{ -h_0 + \frac{h_0^2}{d_0} \right\} + Re_L \Pi_\rho \Pi_u^2 \frac{h_0^3}{d_0} \left\{ -\frac{\partial_x P_{G0}}{Re_G} + \Pi_u^{-4} \frac{\sin(\phi)}{Fr^2} \right\}, \quad (5.2a)$$

$$799 \quad c_1 = i\mathcal{R}, \quad (5.2b)$$

801 where  $\mathcal{R}\in\mathbb{R}$  is written out in appendix B, and the primary flow yields:

$$802 \quad u_{L0}|_{h_0} = \frac{1}{2} \frac{Re_L}{Fr^2} \sin(\phi) h_0^2 + \Pi_\mu \Pi_u T_{G0} h_0 - \frac{1}{2} \Pi_\rho \Pi_u^2 \frac{Re_L}{Re_G} \partial_x P_{G0} h_0^2. \quad (5.3)$$

803 Thus, the asymptotic wave speed is given by  $c_0$ , the (temporal) growth rate by  $kc_1$ , and the  
 804 neutral stability bound by  $\mathcal{R}=0$ .

805 In the zero-confinement limit,  $h_0/d_0 \rightarrow 0$ ,  $c_0$  (5.2a) and  $c_1$  (5.2b) should collapse with the  
 806 expressions in equations (B4b) and (B7b) of Vellingiri *et al.* (2015). Applying this limit to  
 808 (5.1) and rescaling appropriately, we obtain:

$$809 \quad \underline{c} = \underline{c}_0 + \underline{k} \underline{c}_1 + O(\underline{k}^2) = 2 + \underline{T}_{G0} + i \underline{k} \left\{ \frac{4}{15} \underline{Re}_L (2 + \underline{T}_{G0}) - \frac{2}{3} \cot(\phi) [1 - \Pi_\rho] \right. \\ \left. + \frac{1}{3} \Pi_\rho \frac{Re_L}{\Pi_\mu^2} \frac{\underline{C}_1}{\underline{d}_0} + \frac{1}{2} \Pi_\mu \frac{1}{\underline{d}_0} \partial_{\underline{\eta}} \underline{U}_1 \Big|_{\underline{d}_0} \right\} + O(\underline{k}^2), \quad (5.4)$$

810 where the underline refers to the scaling of Vellingiri *et al.* (2015), i.e.  $\underline{\mathcal{L}}=h_0^*$  and

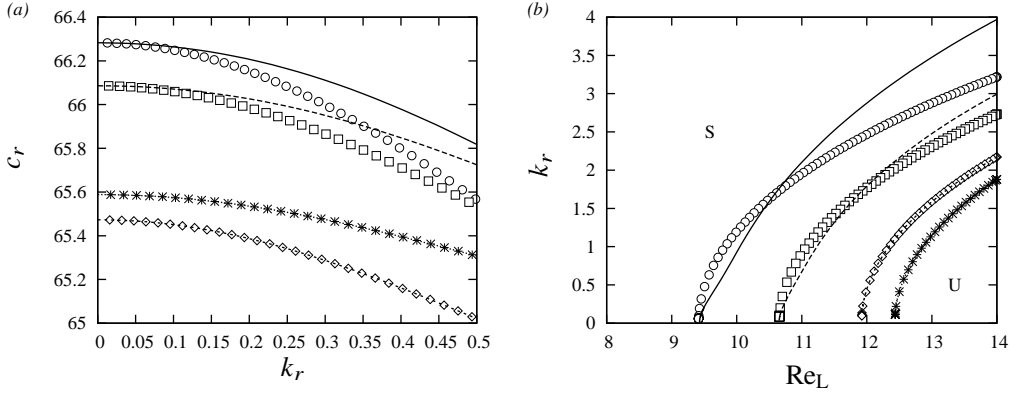


Figure 7: Spatial linear stability predictions obtained from WRIBL-LW (symbols) and WRIBL-OS (lines) calculations. Inclined falling liquid film sheared by a co-current gas based on parameters in Samanta (2014):  $Ka=963$  (glycerol-water and air II in table 1),  $\phi=4^\circ$ ,  $H^*=15$  mm,  $Re_G=2000$ . S/U indicate stable/unstable regions. Circles: full formulation; squares:  $\Pi_\rho=0$  in (3.41); diamonds:  $T_G=T_{G0}$ ,  $\Pi_\rho=0$ ; crosses:  $\Pi_\mu=\Pi_\rho=0$ . (a) Wave speed  $c_r=\omega/k_r$  around the long-wave limit  $k_r \rightarrow 0$ ; (b) neutral stability bound,  $k_i=0$ .

811  $\underline{\mathcal{U}}=\underline{\mathcal{U}}_G=\frac{1}{2}v_L^{-1}g \sin(\phi) h_0^{*2}$ . Our result matches that in the reference, except for three  
 812 additional terms: the gas-density correction in the  $\cot(\phi)$  term, and the last two terms within  
 813 the accolades, which stem from the linear perturbations of  $P_G$  and  $T_G$ . In the laminar limit:

$$814 \quad \underline{C}_1 = \frac{6}{35} d_0^2 T_{G0}^2, \quad \partial_{\underline{d}_0} \underline{U}_1 \Big|_{d_0} = \frac{4}{105} \frac{\Pi_\rho Re_L}{\Pi_\mu^3} d_0^3 T_{G0}^2, \quad (5.5)$$

815 and, thus, these terms do not necessarily vanish for  $1/d_0 \rightarrow 0$ . Thus, the gas pressure  $P_G$  can  
 816 affect stability even under weak confinement, in line with observations in panels 5c and 5d.

817 Figure 7 compares spatial linear stability predictions of our WRIBL-LW model (symbols)  
 818 with calculations using the WRIBL-OS approach (solid lines), for parameters based on figure  
 819 3 in Samanta (2014), which are inspired by the experiments of Liu & Gollub (1994) in a  
 820 water-glycerol film. We fix the channel height at  $H^*=15$  mm and apply a co-current turbulent  
 821 gas flow with  $Re_G=2000$ . Panel 7a represents dispersion curves of the linear wave speed  
 822  $c_r=k_r/\omega$  around the long-wave limit. We see that the two data sets converge as  $k \rightarrow 0$ . Further,  
 823 our WRIBL model accurately captures the long-wave instability threshold, as evidenced by  
 824 the neutral stability bounds plotted in panel 7b. Comparing the circles (full model) with the  
 825 diamonds (passive-gas limit  $\Pi_\rho=\Pi_\mu=0$ ), we see that the gas-effect is destabilizing, and this is  
 826 maintained in the limit  $\Pi_\rho=0$  (squares). By contrast, assuming  $T_G=\text{const}$  and  $\Pi_\rho=0$  (crosses),  
 827 according to the model of Samanta (2014), results in a qualitatively incorrect prediction of  
 828 gas-induced stabilization.

829 We now turn to the experimental conditions of Kofman (2014), who considered a falling  
 830 liquid film sheared by a turbulent counter-current gas flow. Figure 8 confronts linear spatial  
 831 growth rate dispersion curves from our WRIBL-LW model (panels 8a, 8c) with calculations  
 832 based on our WRIBL-OS approach (panels 8b, 8d). Comparing panels 8a and 8b, we see that  
 833 our WRIBL-LW model predicts the gas-effect on the maximum growth rate  $\{-k_i\}_{\max}$  and on  
 834 the associated angular frequency  $\{\omega\}_{\max}$  reasonably well. And, the AI limit is predicted with  
 835 a precision of 10 %, i.e.  $Re_G^{AI}=-9157$  from WRIBL-LW versus  $Re_G^{AI}=-8220$  from WRIBL-OS.  
 836 Panels 8c and 8d represent corresponding stability calculations in the limit  $\Pi_\rho=0$ . Versus  
 837 panels 8a and 8c, we observe a qualitative change in the gas-effect from destabilizing to  
 838 stabilizing (similar to figure 5), and our WRIBL-LW model accurately captures this feature.

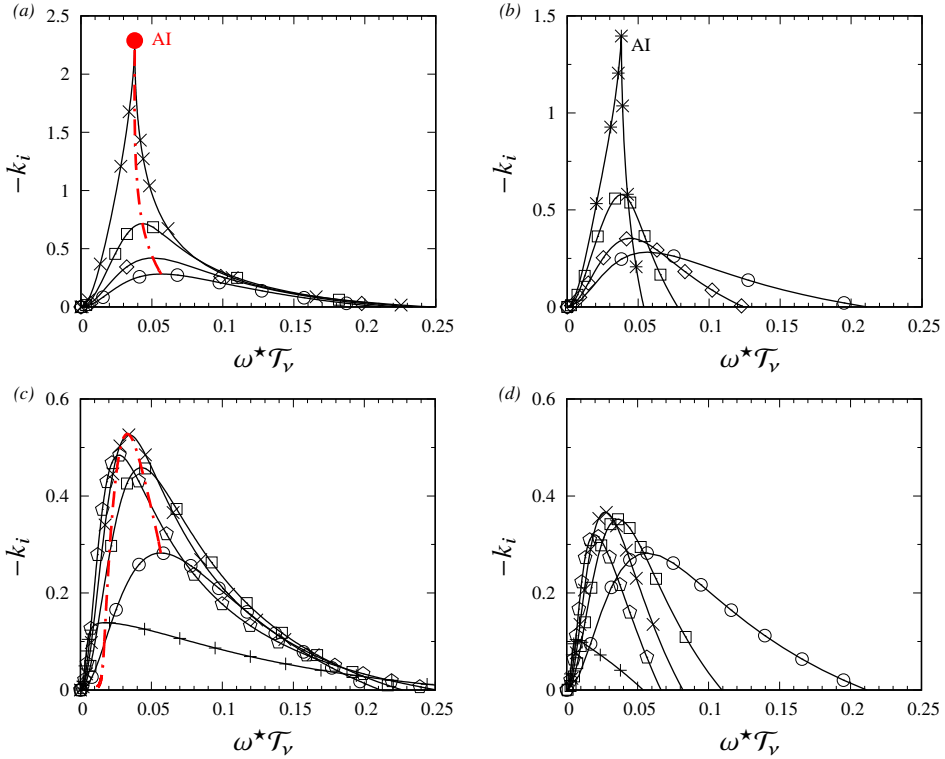


Figure 8: Spatial linear stability predictions from WRIBL-LW (panels *a,c*) and WRIBL-OS (panels *b,d*) approaches. Parameters according to experiments of Kofman (2014):  $Ka=3174$  (water and air I in table 1),  $H^*=19$  mm,  $\phi=5^\circ$ ,  $Re_L=32.7$ . Open circles: passive-gas limit,  $\Pi_\rho=\Pi_\mu=0$  in (3.41).  $|\text{Re}_G|$  increases in the order: [diamonds,squares,crosses/asterisks,pentagons,pluses]. (*a,b*) Full model; (*c,d*)  $\Pi_\rho=0$  in (3.41). (*a*)  $\text{Re}_G=[-4123,-6713,-9157]$ ; (*b*)  $\text{Re}_G=[-4123,-6713,-8220]$ ; (*c*)  $\text{Re}_G=[-6713,-9100,-11000,-15000]$ ; (*d*)  $\text{Re}_G=[-6713,-9100,-11000,-15000]$ . Red dot-dashed curves track growth rate maximum  $\{-k_i\}_{\max}$ . We have rescaled  $\omega$  with  $\tau_v=2.207 \times 10^{-3}$  s (3.34).

839 In contrast to Tseluiko & Kalliadasis (2011), our WRIBL-LW model can thus be applied to  
 840 confinement levels, where the gas pressure plays a role.

841 On the downside, our WRIBL-LW model cannot reproduce the strong gas-induced  
 842 reduction of the cut-off frequency predicted by the WRIBL-OS calculation in panel 8b. This  
 843 is due to truncating our asymptotic gas-side description (section 4.2) at  $\mathcal{O}(\epsilon^1)$ . However, it is  
 844 almost inconsequential for the prediction of nonlinear Kapitza waves. Figure 9 compares film  
 845 thickness time traces at a fixed streamwise position  $x$ , as obtained from open-domain (dashed  
 846 black) and TWS (solid green) computations with our WRIBL-LW model, with experimental  
 847 data (red open circles) from Kofman (2014). In these experiments, the counter-current gas  
 848 flow rate was increased up to  $|\text{Re}_G| \sim 7000$ . Our WRIBL-LW model accurately captures the  
 849 gas-effect on both the wave height and the number of precursory capillary ripples. The wave  
 850 number  $k$  of precursory ripples is several tenfold greater than the cut-off wave number  $k_c$  of  
 851 the Kapitza instability (Dietze 2016; Zhou & Prosperetti 2020). As a result, over-prediction  
 852 of the linear cut-off (panel 8a) does not translate to a significant nonlinear error (figure 9).

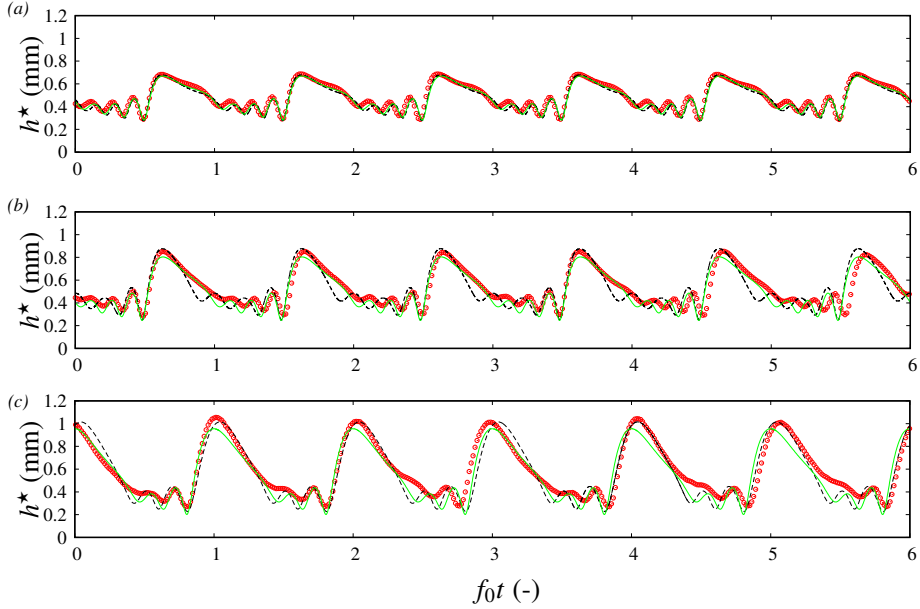


Figure 9: Nonlinear computations (solid and dashed lines) with our WRIBL-LW model (3.6) versus experiments (symbols) of Kofman (2014):  $Ka=3174$  (water and air I in table 1),  $H^*=19$  mm,  $\phi=5^\circ$ ,  $Re_L=32.7$ ,  $f_0^*=2.8$  Hz ( $\omega_0^* \mathcal{T}_v=0.039$ ). Film thickness time traces at fixed streamwise position. Solid green lines: TWS from numerical continuation; dashed black lines: open-domain computations with coherent inlet forcing ( $\varepsilon_1=0.01$ ,  $\varepsilon_2=0$ ). (a) Quiescent gas ( $\Pi_\rho=\Pi_\mu=0$  in computations); (b)  $Re_G=-4123$ ; (c)  $Re_G=-6713$ .

## 853 6. Results

854 Figure 10 shows top-view snapshots of one of our experiments, where we have successively  
 855 increased the counter-current gas flow rate from the second panel onward. Guided by this  
 856 experiment, using the different linear stability calculations as well as nonlinear computations  
 857 with our WRIBL-LW model, we wish to understand how the waviness of the falling liquid  
 858 film is altered under the effect of the gas flow. In particular, we are interested in the transition  
 859 from a regular train of long waves (first panel), via an increasingly disordered wave pattern  
 860 (e.g. tenth panel), until the occurrence of upward-travelling short ripples, which lead to a  
 861 breakdown of our experiment (last panel).

### 862 6.1. Gas-effect on Kapitza waves

863 This section is concerned with the linear (subsection 6.1.1) and nonlinear (subsections 6.1.2  
 864 and 6.1.3) gas-effect on the long-wave Kapitza instability. Waves resulting from this instability  
 865 are dominant at weaker counter-current gas flow rates in figure 10, i.e.  $|Re_G| \lesssim 6200$  (first ten  
 866 panels), and the linear instability becomes absolute in this range, as will be shown in figure  
 867 12.

#### 868 6.1.1. Linear gas-effect

869 We start by discussing the gas-effect on the threshold of the Kapitza instability. Panel 11a  
 870 represents the neutral stability bound,  $c_1=0$  according to (5.2b), in terms of  $Re_L$  and  $Re_G$ ,  
 871 for two inclination angles, i.e.  $\phi=5^\circ$  (black curves with circles), which corresponds to our  
 872 experiment in figure 10, and  $\phi=1^\circ$  (red curves with diamonds). For each  $\phi$ , we have plotted two  
 873 curves, one obtained from our WRIBL-LW model for turbulent gas flow conditions (filled  
 874 symbols), and another obtained from the fully-coupled governing equations (Tilley *et al.*



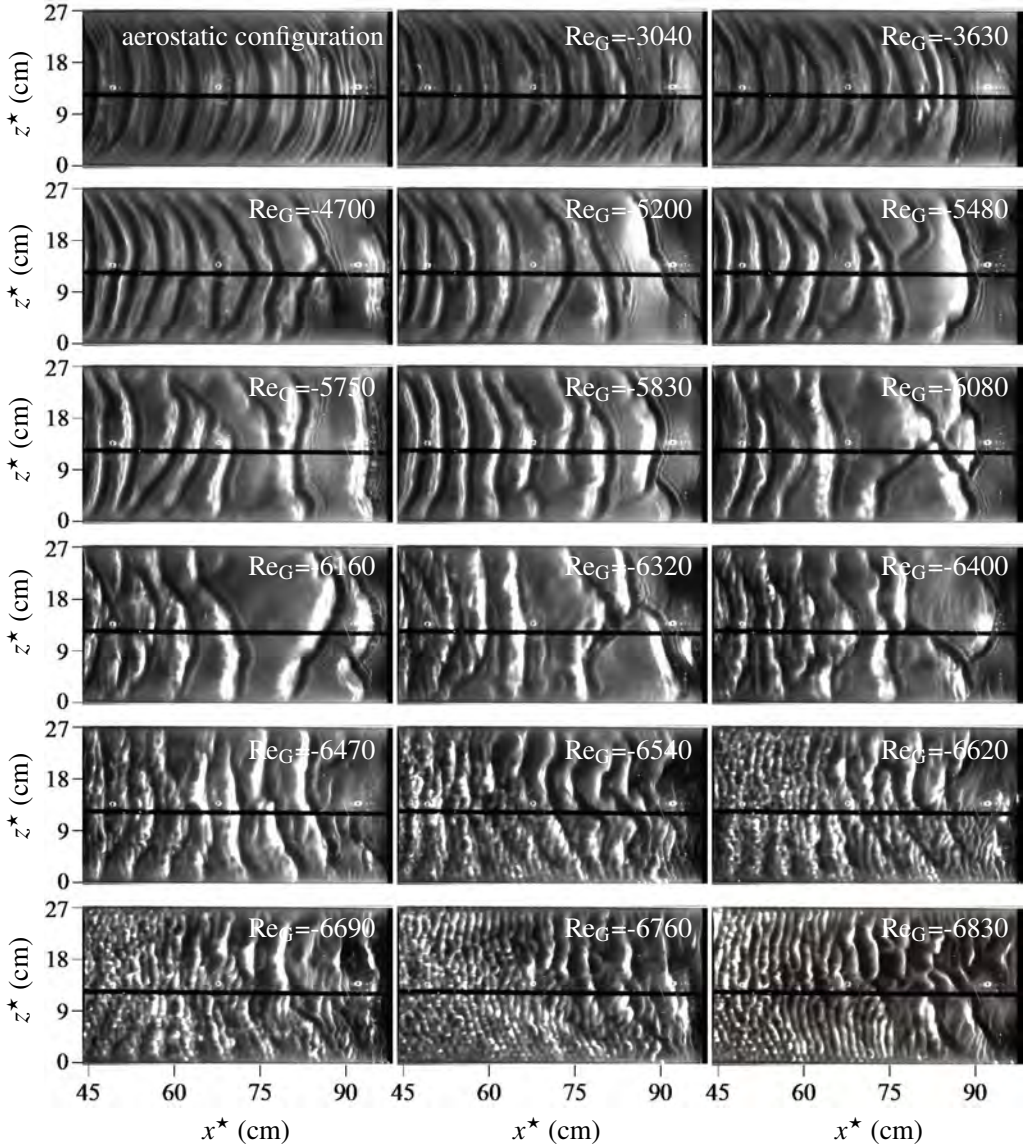


Figure 10: Top view snapshots from one of our experiments. Falling water film sheared by a counter-current air flow and subject to coherent inlet forcing:  $H^* = 13$  mm,  $\phi = 5^\circ$ ,  $Re_L^{as} = 44.7$ ,  $Re_L = 43.1$ ,  $f_0^* = 3.0$  Hz. First panel: aerostatic configuration; panel 2 and onward: counter-current turbulent gas flow with increasing  $|Re_G|$ . Absolute instability limit from linear stability calculation in figure 12:  $Re_G^{AI} = -5182$ .

875 1994) for laminar gas flow conditions (open symbols). Only the curve segments within the  
 876 appropriate  $Re_G$  range are represented with solid lines, and the laminar/turbulent transition  
 877 is highlighted via the shaded region.

878 For  $\phi = 5^\circ$  (black curves with circles), the linear effect of the counter-current gas flow is  
 879 destabilizing. Further, when the counter-current gas flow rate is sufficiently large, the falling  
 880 liquid film becomes unconditionally unstable (limit point marked by filled circle), i.e. for all  
 881  $Re_L$ , in agreement with previous works (Trifonov 2017; Kushnir *et al.* 2021). We find that



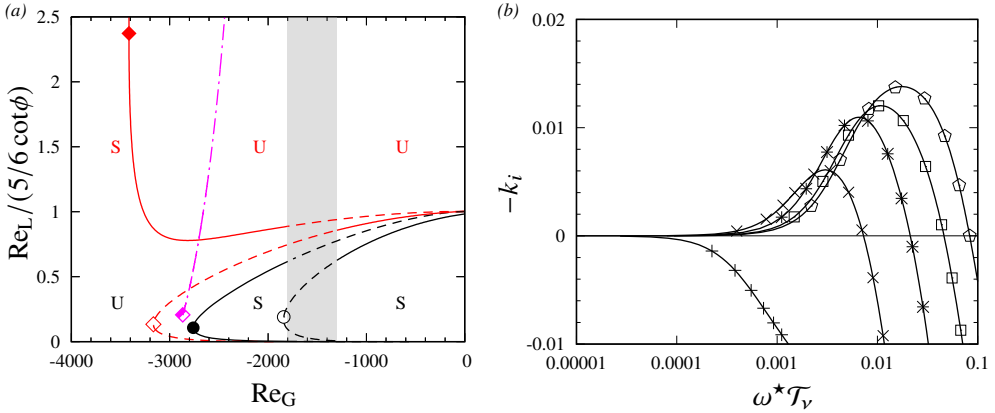


Figure 11: Gas-effect on threshold of long-wave Kapitza instability. Linear stability predictions for a falling liquid film sheared by a counter-current gas flow:  $Ka=3174$  (water and air I in table 1),  $H^*=13$  mm. (a) Neutral stability bounds. Black curves with circles:  $\phi=5^\circ$ , red curves with diamonds:  $\phi=1^\circ$ . Curves with filled symbols: WRIBL-LW/WRIBL-OS prediction for turbulent gas flow, curves with open symbols: fully-coupled prediction for laminar gas flow (Tilley *et al.* 1994), dot-dashed black curve: short-wave instability mode (section 6.2) at  $\phi=1^\circ$ , shaded zone: turbulence transition,  $Re_G \in [-1800, -1300]$ . S/U denote stable/unstable regions; (b) spatial growth rate dispersion curves from WRIBL-OS:  $\phi=1^\circ$ ,  $Re_L=1.5(5/6) \cot(\phi)$ . Pentagons:  $\Pi_\rho=\Pi_\mu=0$  in (3.41), squares to pluses:  $Re_G=-1000, -2000, -3000, -3600$ .

882 turbulence in the gas greatly delays this limit versus a laminar prediction (compare filled and  
883 open circle).

884 By contrast, for  $\phi=1^\circ$  (red curves with diamonds), we find a change in nature of the  
885 gas-effect, as a result of gas-side turbulence. While the gas-effect remains destabilizing in  
886 the laminar limit (red curve with open diamond), it switches to stabilizing when turbulence  
887 is accounted for (red curve with filled diamond). This is further illustrated in panel 11b,  
888 which represents dispersion curves of the linear spatial growth rate for increasing  $|Re_G|$  at  
889  $Re_L=1.5(5/6) \cot(\phi)$ . Thus, turbulence allows to achieve a gas-induced suppression of the  
890 Kapitza instability for the current confinement,  $H^* \sim 10$  mm, which is much weaker than the  
891 confinement studied in Lavallo *et al.* (2019),  $H^* \sim 1$  mm, where the gas flow was laminar.  
892 And, the counter-current gas flow can render the falling liquid film unconditionally stable to  
893 long-wave disturbances at the limit point marked by a filled diamond in panel 11a. However,  
894 as we will discover in section 6.2, the film can become unstable to a short-wave instability  
895 mode at small  $\phi$ , and the threshold for this mode (dot-dashed curve in panel 11a) lies below  
896 the neutral stability bound of the Kapitza instability for the parameters considered here. Thus,  
897 the falling liquid film cannot be fully stabilized in this case.

898 Gas-induced stabilization of the Kapitza mode is limited to small inclination angles, and  
899 plays no role in our current experiments, where the effect of the counter-current gas flow  
900 on the falling liquid film is destabilizing. In this case, it is interesting to determine the AI  
901 limit and to confront it with the  $Re_G$  range of our experiments. Figure 12 represents WRIBL-  
902 OS spatial linear stability predictions for the experimental parameters in figure 10. Upon  
903 increasing the counter-current gas flow rate (from circles to crosses), the  $-k_i$  versus  $\omega$  curve  
904 in panel 12a, and the  $c_r$  versus  $\omega$  curve in panel 12b, develop a cusp at  $Re_G=-5114$ . This cusp  
905 corresponds to a pinch point in the  $-k_i$  versus  $k_r$  curve (inset of panel 12a), which indicates  
906 the AI limit (Kupfer *et al.* 1987). Thus, the falling liquid film in figure 10 is absolutely  
907 unstable from the 5th panel onward, i.e. well before the breakdown of our experiment due to  
908 upward-travelling ripples ( $Re_G \sim -6800$ ). Consequently, AI does not seem to play a role in

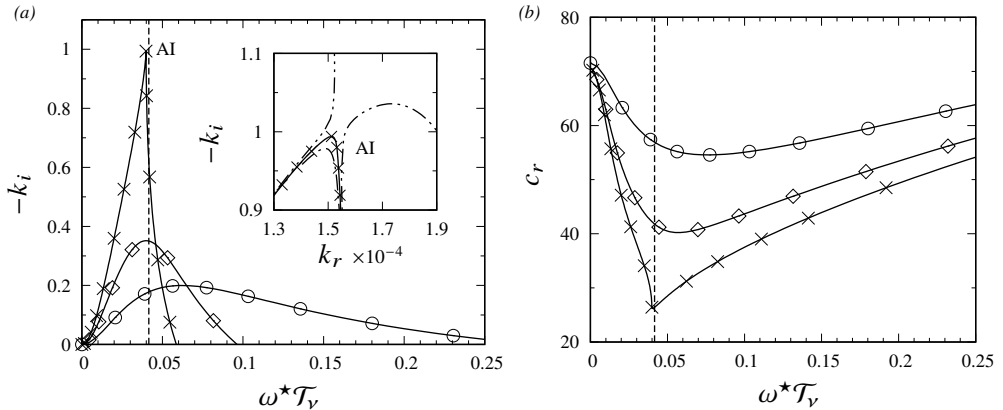


Figure 12: Transition to AI predicted by spatial linear stability analysis with our WRIBL-OS approach. Parameters according to experiment in figure 10:  $\text{Ka}=3174$  (water and air I in table 1),  $H^*=13$  mm,  $\phi=5^\circ$ ,  $\text{Re}_L=43.1$ . Circles:  $\Pi_\rho=\Pi_\mu=0$  in (3.41). Diamonds:  $\text{Re}_G=-4000$ , crosses:  $\text{Re}_G=-5181$ . (a) Growth rate  $-k_i$  versus  $\omega$ . Inset shows  $-k_i$  versus  $k_r$ . Dot-dashed:  $\text{Re}_G=-5180$ , dot-dot-dashed:  $\text{Re}_G=\text{Re}_G^{\text{AI}}=-5182$ ; (b) wave speed  $c_r=\omega/k_r$ . Vertical dashed: forcing frequency  $f_0^*=3$  Hz from figure 10. We have rescaled  $\omega$  with  $\mathcal{T}_v=2.207 \times 10^{-3}$  s (3.34).

909 the flooding onset. On the contrary, well-defined downward-travelling Kapitza waves persist  
 910 far beyond the AI limit (up to 10th panel in figure 10), and we will discuss the nonlinear  
 911 dynamics of these waves in the next subsections.

### 912 6.1.2. Nonlinear gas-effect: travelling-wave solutions (TWS)

913 We wish to know whether the nonlinear response of the wavy falling liquid film is in line with  
 914 the linear gas-effect discussed in the previous section. Figure 13 compares the wave height  
 915 (panels 13a, 13c) and wave speed (panels 13b, 13d) of nonlinear TWS obtained from our  
 916 WRIBL-LW model at fixed frequency  $f$  (solid curves), with experiments (symbols) from our  
 917 current work (panels 13a, 13b), where  $H^*=13$  mm, and from Kofman *et al.* (2017) (panels  
 918 13c, 13d), where  $H^*=19$  mm. The experimental wave height data in panel 13a were selected  
 919 from film thickness time trace measurements performed over the entire channel length, which  
 920 will be discussed in section 6.1.3 (figure 14 there). The wave speed data in panel 13b were  
 921 obtained via video image processing from our experiment in figure 10, where  $\text{Re}_L$  is slightly  
 922 different than in panel 13a.

923 Different solid curves in figure 13 correspond to different branches of TWS, which are  
 924 associated with different numbers of precursory capillary ripples (CR) and distinguished by  
 925 different filled symbols. For the experimental data points, the number of CR is distinguished  
 926 via corresponding open symbols. Error bars in panel 13a represent the standard deviation  
 927 of experimental film thickness time traces, which increases with increasing  $|\text{Re}_G|$  as a result  
 928 of wave coalescence events (section 6.1.3). Beyond a certain  $|\text{Re}_G|$ , coalescence entirely  
 929 destroys the coherence of the wave train and comparison with TWS is futile.

930 Overall, our WRIBL-LW predictions in panels 13a, 13b, 13c, and 13d are in reasonable  
 931 agreement with the experimental data. Both the gas-effect on the wave height and the wave  
 932 speed are captured quantitatively, when accounting for the number of CR.

933 Based on these predictions, we may make the following observations. Downward-traveling  
 934 TWS exist far beyond the AI limit, marked by open (WRIBL-LW calculation) and filled  
 935 (WRIBL-OS calculation) red arrows in panels 13a and 13c. Below the AI limit, the wave  
 936 height  $h_{\text{max}}$  increases with increasing  $|\text{Re}_G|$ , while the wave speed mainly decreases. And, we

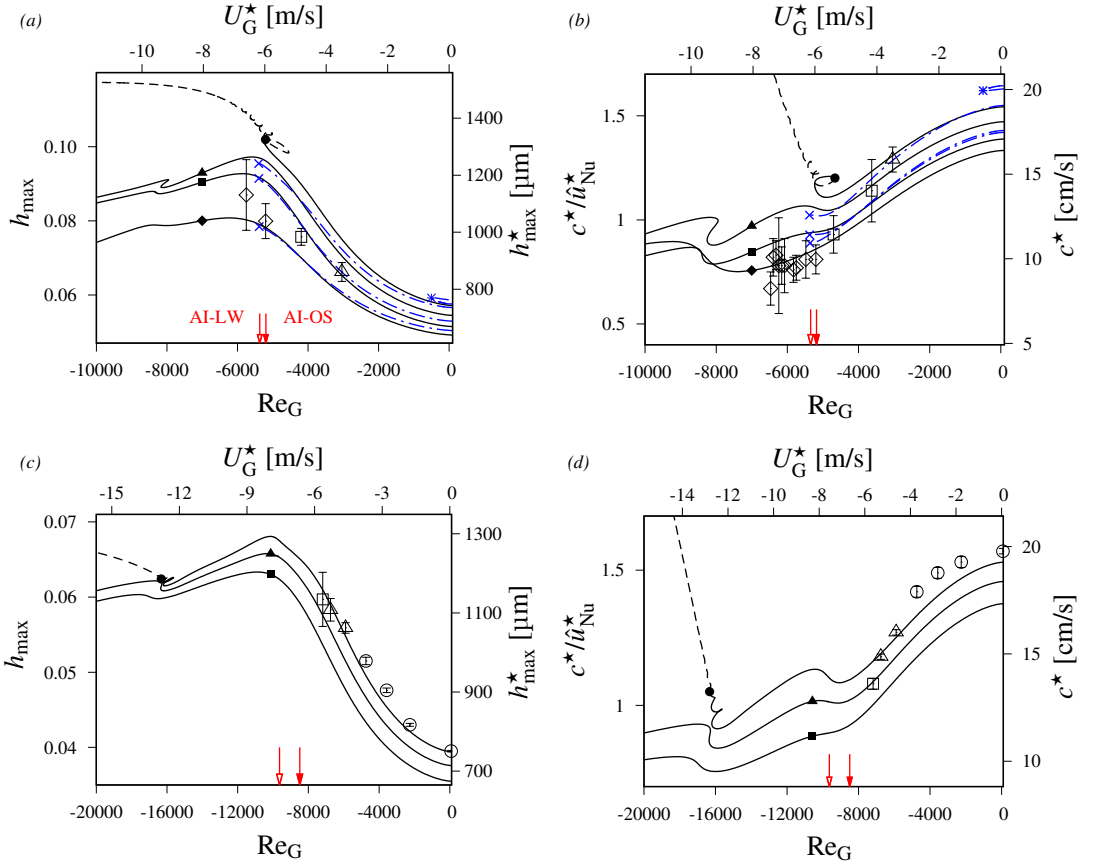


Figure 13: Gas-effect on nonlinear TWS obtained with our WRIBL-LW model (curves) versus experiments (empty symbols). Inclined falling liquid film sheared by counter-current turbulent gas flow:  $Ka=3174$  (water and air I in table 1),  $\phi=5^\circ$ . Filled/open symbols distinguish number of capillary ripples (CR). Diamonds: 0-CR, squares: 1-CR, triangles: 2-CR, circles: 3-CR, dashed:  $>3$ -CR. Solid curves:  $f^*=f_0^*$ , dot-dashed curves:  $f^*=f_{\max}^*$ . Crosses: AI limit, asterisk: nonlinear LP. Open/filled red arrows mark AI limit obtained from WRIBL-LW/WRIBL-OS. (a,c) Wave height; (b,d) wave speed scaled with  $\hat{u}_{\text{Nu}}^*=(3/2)q_{\text{L0}}^*/h_{\text{Nu}}^*$ , where  $h_{\text{Nu}}^*=(3q_{\text{L0}}^*\nu_{\text{L}}/g/\sin(\phi))^{1/3}$ . (a,b) Versus our experiments:  $H^*=13$  mm,  $f_0^*=3.0$  Hz. (a)  $\text{Re}_{\text{L}}=44.2 \pm 0.3$ . Filled arrow:  $\text{Re}_{\text{G}}^{\text{AI}}=-5194$ , empty arrow:  $\text{Re}_{\text{G}}^{\text{AI}}=-5366$ . (b)  $\text{Re}_{\text{L}}=43.1$ ; (c,d) versus experiments of Kofman *et al.* (2017):  $H^*=19$  mm,  $\text{Re}_{\text{L}}=45$ ,  $f_0^*=3.05$  Hz. Filled arrow:  $\text{Re}_{\text{G}}^{\text{AI}}=-8490$ , empty arrow:  $\text{Re}_{\text{G}}^{\text{AI}}=-9633$ .

937 have checked that the relative wave amplitude  $h_{\max}/\bar{h}$  (not shown here) also increases. Thus,  
 938 the non-linear gas-effect is destabilizing, in line with the linear effect discussed in section  
 939 6.1.1.

940 For the 0-CR, 1-CR, and 2-CR branches, the  $h_{\max}$  versus  $|\text{Re}_{\text{G}}|$  trend in panels 13a and  
 941 13c changes beyond the AI limit, i.e.  $h_{\max}$  now decreases with  $|\text{Re}_{\text{G}}|$  (except for small non-  
 942 monotonous regions). For the 3-CR branches (solid curves with filled circles), the trend  
 943 beyond the AI limit is more complicated, i.e.  $h_{\max}$  first decreases with  $|\text{Re}_{\text{G}}|$ , and then  
 944 increases, beyond  $|\text{Re}_{\text{G}}|=8000$  in panel 13a and beyond  $|\text{Re}_{\text{G}}|=16000$  in panel 13c. This  
 945 increase is associated with the formation of an increasing number of additional capillary  
 946 ripples (dashed curve segments) and a strong increase of the wave speed  $c$  is observed in

947 panels 13b and 13d, whereas  $c$  mostly decreases with  $|\text{Re}_G|$  for the other solution branches  
 948 (solid curves with filled diamonds, squares, and triangles).

949 Focusing now on the experimental data points (open symbols in panels 13a and 13b), we  
 950 observe that the number of CR decreases when increasing  $|\text{Re}_G|$  (from open circles to open  
 951 diamonds). According to the computations with our WRIBL-LW model (solid curves), this  
 952 corresponds to a switching of TWS branches in the direction of lowest wave speed. This is  
 953 surprising, because one would expect the fastest TWS to persist in an experiment at fixed  
 954  $\text{Re}_G$ . Additional effects must thus play a role in the wave selection.

955 In our experiment, saturated waves of fixed frequency  $f_0^*$  are formed before entering  
 956 into contact with the counter-current gas flow. In panels 13a and 13b we have compared  
 957 the gas-effect on such waves, i.e. TWS at  $f^*=f_0^*=3$  Hz (solid curves), with TWS at the  
 958 linearly most-amplified frequency, i.e.  $f^*=f_{\text{max}}^*$  (dot-dashed blue curves). Except for the  
 959 3-CR branch (dot-dashed curve with asterisk), both types of TWS behave quite similarly  
 960 until the AI limit (where the  $f_{\text{max}}^*$  branches break down). This is because  $f_{\text{max}}^*$  does not vary  
 961 much with  $\text{Re}_G$ , and, thus, the forcing frequency  $f_0^*$  chosen in the experiment remains close  
 962 to  $f_{\text{max}}^*$ . By contrast, in the case of the 3-CR branch, the most-amplified TWS are lost due  
 963 to a nonlinear limit point (filled blue circle), before the gas flow reaches the fully turbulent  
 964 regime ( $|\text{Re}_G| < 1800$ ).

### 965 6.1.3. Nonlinear gas-effect: spatio-temporal wave dynamics

966 In a spatially-evolving falling liquid film, the counter-current gas flow not only acts on  
 967 nonlinear Kapitza waves individually, but can trigger interactions between consecutive waves.  
 968 Thus, we study the gas-effect on the spatio-temporal dynamics of such waves.

969 Panel 14a summarizes spatial profiles of film thickness data obtained from our experiments  
 970 at  $\text{Re}_L^{\text{as}}=46$ ,  $\text{Re}_L=44.2 \pm 0.7$ , and  $f_0^*=3$  Hz, under increasing  $|\text{Re}_G|$ . Symbols represent the  
 971 ensemble average of the wave height  $h_{\text{max}}^*$  (over at least 100 waves) at a given streamwise  
 972 position  $x^*$ , and error bars represent the corresponding standard deviation. Filled symbols  
 973 identify the TWS data reported in panels 13a and 13b.

974 In the aerostatic configuration (open circles in panel 14a), the error bars are very short,  
 975 implying that waves are highly regular in time. However,  $h_{\text{max}}^*$  varies in space as the result  
 976 of the well-known secondary instability discovered by Liu & Gollub (1993).

977 In the counter-current configuration (from diamonds to triangles in panel 14a), we observe  
 978 that  $h_{\text{max}}^*$  in the lower half of the channel ( $x^* \gtrsim 50$  cm) significantly increases when  $|\text{Re}_G|$  is  
 979 increased. On the one hand, this is due to the gas-induced amplification of TWS discussed  
 980 in section 6.1.2. On the other hand, the standard deviation of the  $h_{\text{max}}^*$  data significantly  
 981 increases as  $|\text{Re}_G|$  is increased. This is the signature of wave coalescence events that can  
 982 suddenly increase the wave height. Figure 15 represents a sequence of snapshots illustrating  
 983 such an event for  $\text{Re}_G=-5200$  (pentagons in panel 14a). The red solid and dashed yellow lines  
 984 highlight the fronts of two consecutive waves that eventually coalesce.

985 In panel 14a, we have marked the streamwise position beyond which such coalescence  
 986 events become prevalent via check marks on the corresponding error bars. This position,  
 987 which we will designate as  $x_c^*$ , is determined from the spatial evolution of the frequency  
 988 spectrum of  $h^*$ , as illustrated in panel 14b for  $\text{Re}_G=-5750$  (triangles in panel 14a). We see  
 989 that the spectrum evolves from that of a regular wave train, with clear peaks at the forcing  
 990 frequency  $f_0^*$  and its harmonics (left panel), to a form where the dominant frequency  $f_{\text{max}}^*$   
 991 is lower than the forcing frequency (right panel). The streamwise locations of the transition,  
 992 i.e. where  $f_{\text{max}}^*$  becomes smaller than  $f_0^*$  (middle panel), is defined as  $x_c^*$ .

993 Judging by the standard deviation of the  $h_{\text{max}}^*$  profiles in panel 14a, wave coalescence  
 994 becomes more prominent as  $|\text{Re}_G|$  is increased. We have seen in panel 13b that the counter-  
 995 current gas flow reduces the wave speed of TWS. At fixed wave frequency  $f^*$ , this leads to

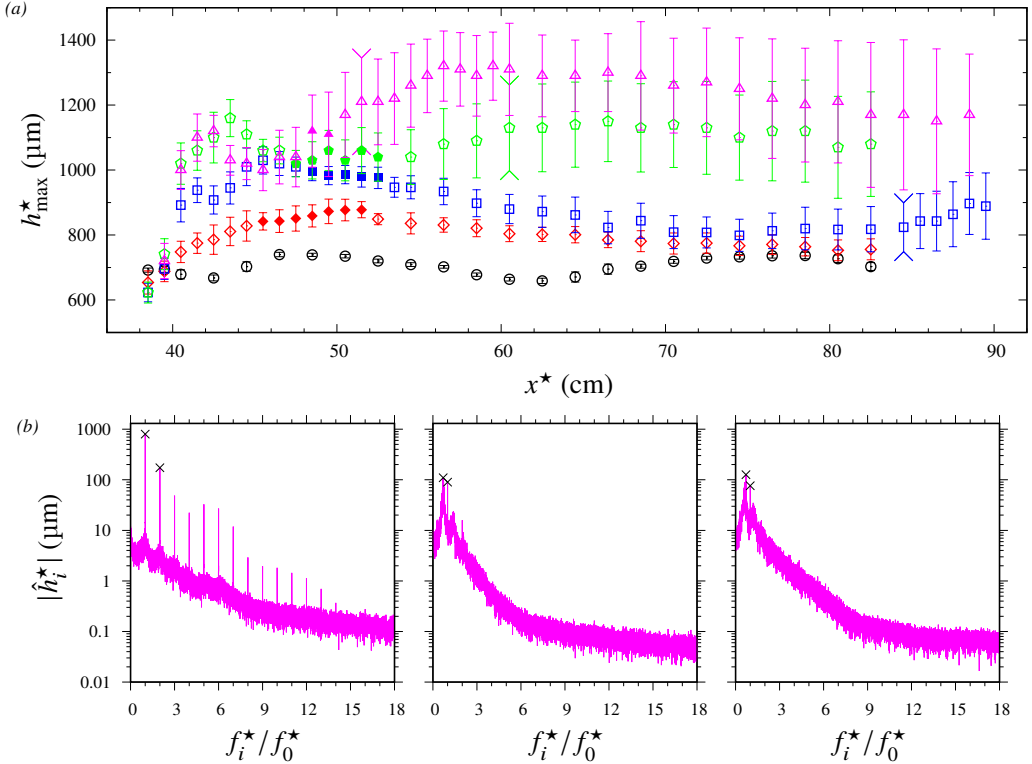


Figure 14: Gas-effect on streamwise evolution of the wavy liquid film. Compilation of our experiments: water/air,  $H^*=13$  mm,  $\phi=5^\circ$ ,  $\text{Re}_L^{\text{as}}=46$ ,  $\text{Re}_L=44.2\pm 0.3$ ,  $f_0^*=3$  Hz,  $\text{Re}_G^{\text{AI}}=-5194$ . (a) Ensemble-averaged wave height  $h_{\max}^*$ . Error bars represent standard deviation, and check marks mark start of coalescence-dominated region. Filled symbols mark data points used in panel 13a. Circles: aerostatic configuration; diamonds:  $\text{Re}_G=-3040$ ; squares:  $\text{Re}_G=-4190$ ; pentagons:  $\text{Re}_G=-5200$ ; triangles:  $\text{Re}_G=-5750$ ; (b) frequency spectra of the film height  $h^*$ :  $\text{Re}_G=-5750$ .  $|\hat{h}_i^*|$  denotes amplitude of Fourier mode with  $f_i^*$ . Crosses mark primary and secondary peaks. Left:  $x^*=41.5$  cm, middle:  $x^*=51.5$  cm, right:  $x^*=58.5$  cm.

996 a reduction of the wave separation distance, thus favoring wave interaction and coalescence.  
 997 Figure 16 provides a direct comparison of wave trains for two of the experiments from  
 998 panel 14a. Panel 16a confronts film thickness time traces measured at  $x^*=82.5$  cm for the  
 999 aerostatic configuration (solid black curve) and for the counter-current configuration at  $\text{Re}_G=-$   
 1000 5750 (dashed red curve). Whereas the former represents a regular train of waves responding  
 1001 well to the forcing frequency, the latter displays clear signs of coalescence-induced wave  
 1002 coarsening, leading to large-amplitude tsunami waves with a wave height much greater than  
 1003 the TWS in panel 13a. Panels 16b and 16c represent corresponding frequency spectra for  
 1004 the two data sets. Whereas the forcing frequency  $f_0^*=3$  Hz is dominant in the spectrum for  
 1005 the aerostatic configuration (panel 16b), a lower frequency emerges for the counter-current  
 1006 configuration, where periodicity is entirely lost (panel 16c).

1007 In figure 17, we have plotted the starting location  $x_c^*$  of the coalescence-dominated region  
 1008 versus  $\text{Re}_G$ , based on all of our experiments for two values of  $\text{Re}_L$ . The error bars on  $x_c^*$   
 1009 correspond to the increment with which the  $x$ -position was varied in the experimental runs  
 1010 reported in panel 14a. According to figure 17, coalescence is greatly precipitated by the  
 1011 (turbulent) counter-current gas flow and this effect is stronger, the lower the liquid flow rate.

1012 The nonlinear wave phenomena discussed in figures 14 to 17 do not seem to be disrupted by

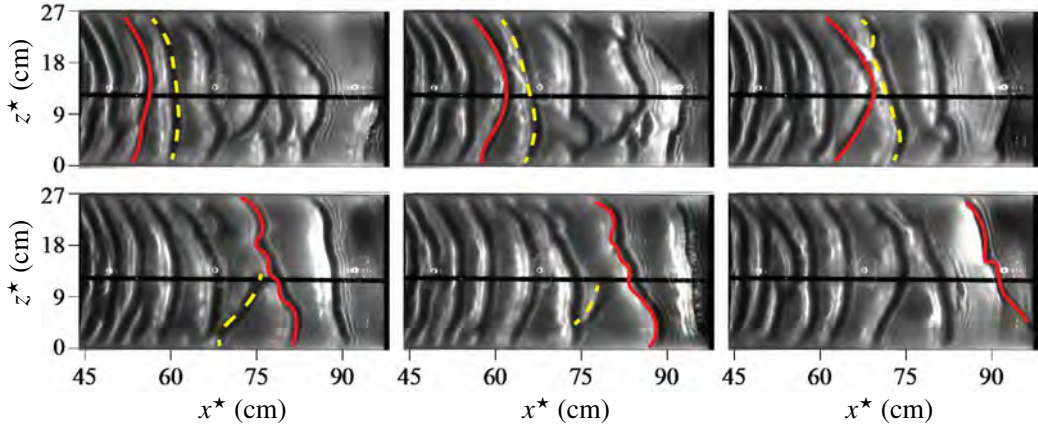


Figure 15: Wave coalescence event. Top view snapshots from our experiment in figure 10 (parameters similar to pentagons in panel 14a):  $Re_L=43.1$ ,  $Re_G=-5200$ . Time increases from top left to bottom right with an increment of 0.48 s. Solid red and dashed yellow lines highlight two consecutive wave fronts.

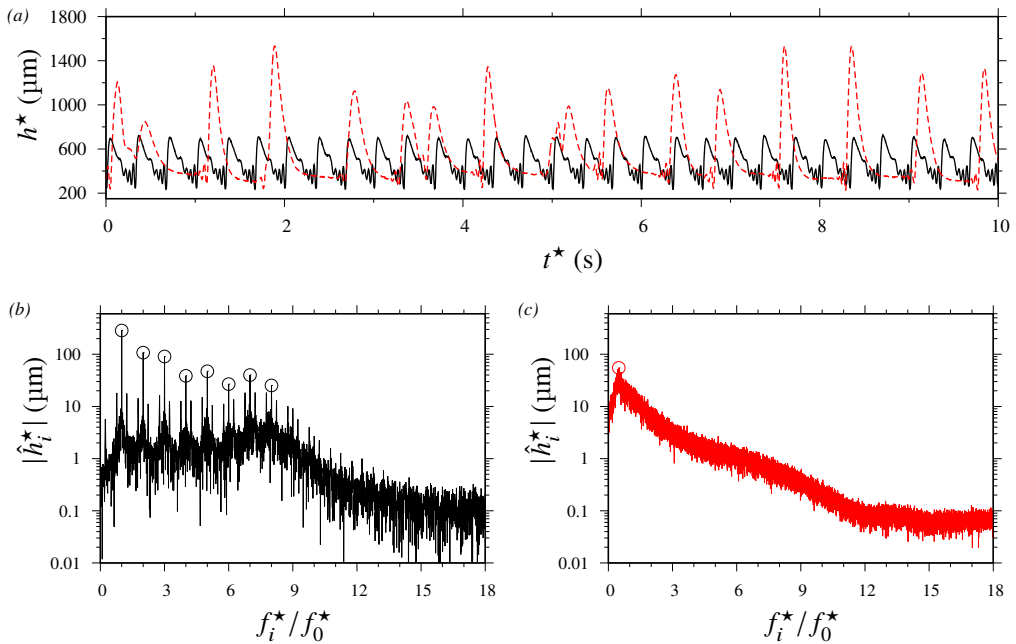


Figure 16: Wave trains for two data sets from panel 14a. (a) Film thickness time traces at  $x^*=82.5$  cm. Solid: aerostatic configuration (circles in panel 14a),  $Re_L^{as}=46.0$ ; dashed: counter-current configuration (triangles in panel 14a),  $Re_L=44.2$ ,  $Re_G=-5750$ ; (b,c) corresponding frequency spectra.  $|\hat{h}_i^*|$  is the amplitude of the Fourier mode with  $f_i^*$ . (b) Aerostatic configuration. Open circles mark peaks at  $f_0^*$  and its harmonics; (c) counter-current configuration. Open circle marks global peak at most amplified frequency  $f_{max}^*/f_0^*=0.49$ .

1013 AI, even though we have considered values of  $|Re_G|$  quite far beyond the AI limit, i.e.  $Re_G^{AI}=-$   
 1014 5194 at  $Re_L=44.2$ . This is favored by the protected zone used in our experiments, where  
 1015 Kapitza waves are allowed to complete their linear and nonlinear growth in a quiescent gas,  
 1016 and where the Kapitza instability remains convective. Only after having attained a saturated



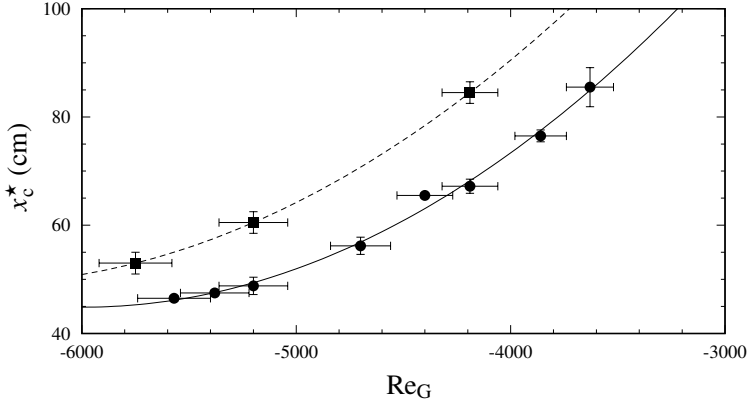


Figure 17: Gas-effect on the starting position  $x_c^*$  of the coalescence-dominated region. Compilation of our experiments: water/air,  $H^*=13$  mm,  $\phi=5^\circ$ ,  $f_0^*=3$  Hz. Circles:  $Re_L=32.5 \pm 0.6$ , squares:  $Re_L=44.3 \pm 0.3$ , curves: polynomial fits to guide the eye.

1017 nonlinear state, these waves come into contact with the gas flow, and, consequently, the AI  
1018 is bypassed.

1019 Next, we employ open-domain computations with our WRIBL-LW model to study the  
1020 linear and nonlinear spatio-temporal evolution of Kapitza waves that feel the gas-effect  
1021 from the start. In these computations, the turbulent counter-current gas flow is applied over  
1022 the entire domain length. Of course, our WRIBL-LW model can only capture long-wave  
1023 instabilities, such as the Kapitza instability, which we focus on in the current section.

1024 We start by studying the gas-effect on the dynamics of naturally-evolving Kapitza waves,  
1025 which are more relevant for industrial applications. Here, the liquid flow rate  $q$  at the  
1026 liquid inlet is subject to a noisy perturbation according to (3.46), with  $\varepsilon_1=0$ ,  $\varepsilon_2=5 \times 10^{-5}$ .  
1027 Figure 18 represents snapshots of our open-domain WRIBL-LW computations for parameters  
1028 according to three of the experiments in panel 14a (circles, squares, and triangles there).  
1029 In panels 18a (aerostatic configuration) and 18b ( $Re_G=-4190$ ), the AI limit  $Re_G^{AI}=-5114$   
1030 (obtained from WRIBL-LW model) has not been reached, and we observe the same  
1031 phenomena as in our experiments from figure 14. In particular, the counter-current gas  
1032 flow exacerbates coalescence events, leading to large-amplitude tsunami waves, which  
1033 move very rapidly and absorb numerous smaller waves in their path. This gas-assisted  
1034 coarsening dynamics is illustrated in panel 19a, representing a spatio-temporal diagram for  
1035 the computation in panel 18b (see also supplementary movie MovieFig18b).

1036 A very different dynamics unfolds when  $|Re_G|$  is increased beyond the AI limit, as shown  
1037 in panels 18c and 19b, which correspond to  $Re_G=-5750$  (see also supplementary movie  
1038 MovieFig18c). Here, coalescence events are absent, and a highly regular train of saturated-  
1039 amplitude solitary waves develops. The height  $h_{max}$  of these waves is significantly smaller  
1040 than that of the tsunami waves in panel 18b, thus limiting the risk of flooding. At the  
1041 same time,  $h_{max}$  is large enough that a significant wave-induced intensification of heat and  
1042 mass transport can be expected (Dietze 2019). Thus, AI is not necessarily dangerous in our  
1043 configuration. On the contrary, the unbounded linear spatial growth rate associated with  
1044 AI represents an effective linear wave selection mechanism that produces highly-regular  
1045 nonlinear surfaces waves of the absolute frequency  $f_{AI}^*=3.35$  Hz from ambient noise ( $f_{AI}^*$   
1046 is obtained from a WRIBL-LW calculation based on panel 12a). Thereby, nonlinear effects,  
1047 which set in very close to the liquid inlet, allow the Kapitza waves to travel downstream,  
1048 notwithstanding the temporal nature of the linear growth. As far as we know, such a dynamics



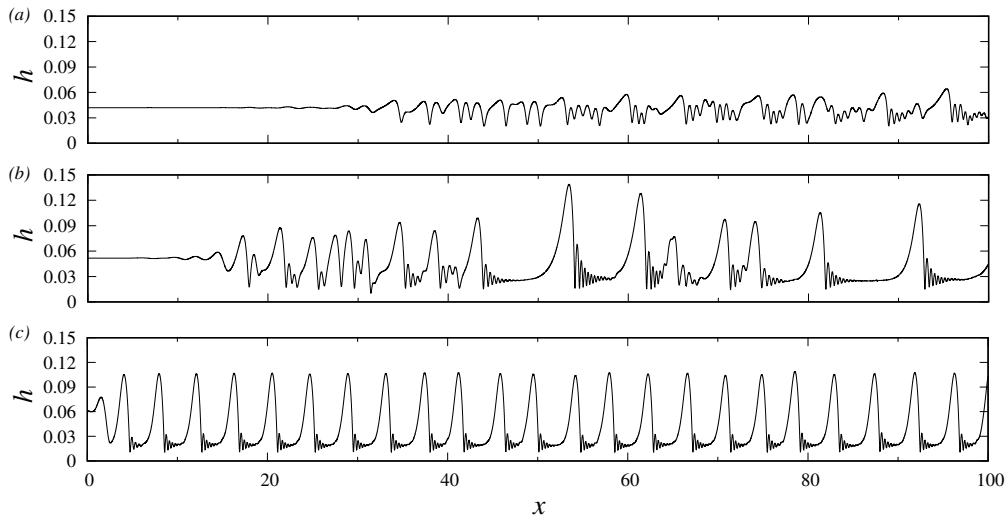


Figure 18: Gas-effect on spatial evolution of naturally-evolving Kapitza waves. Open-domain computations using our WRIBL-LW model on a domain of length  $L^*=1.50$  m. The gas flow is applied over the entire domain length. Noisy inlet perturbation according to (3.46):  $\varepsilon_1=0$ ,  $\varepsilon_2=5 \times 10^{-5}$ . Parameters according to experiments in panel 14a (circles, squares, and triangles there):  $Ka=3174$  (water and air I in table 1),  $H^*=13$  mm,  $\phi=5^\circ$ ,  $Re_L=43.1$ . (a)  $\Pi_\rho=\Pi_\mu=0$  in (3.6a); (b)  $Re_G=-4190$ ; (c)  $Re_G=-5750$ . The AI limits, obtained from WRIBL-LW and WRIBL-OS, are  $Re_G^{AI}=-5347$  and  $Re_G^{AI}=-5182$ .

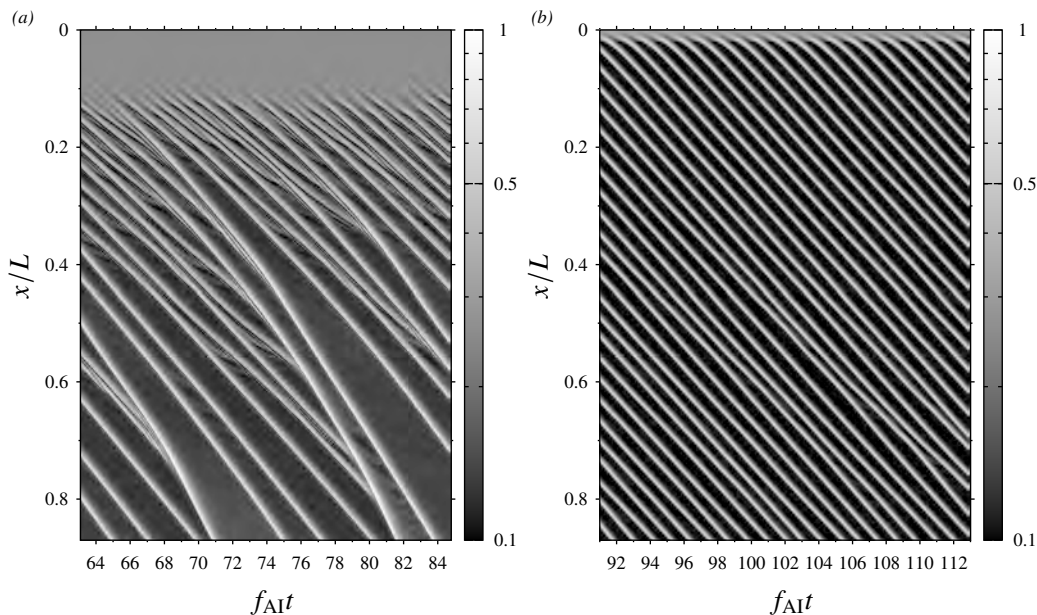


Figure 19: Spatio-temporal diagrams of the normalized film height  $h/h_{\max}$  for the computations in panels 18b and 18c. (a)  $Re_G=-4190$ ; (b)  $Re_G=-5750$ . The AI frequency is  $f_{AI}^*=3.35$  Hz, as obtained from linear stability analysis based on our WRIBL-LW model.

1049 has not been shown before, and we have checked that it persists at  $Re_G=-6500$  (not shown  
 1050 here), i.e. far beyond the value of  $|Re_G|$  in panel 19b .

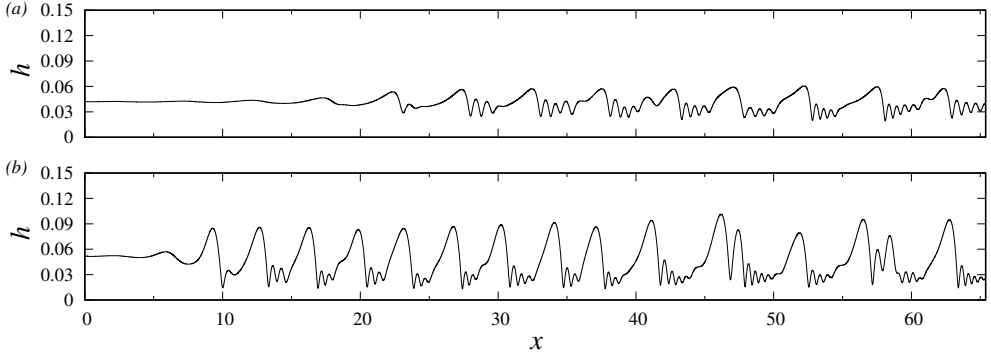


Figure 20: Computations according to panels 18a and 18b, but with additional coherent inlet forcing (3.46):  $f_0^* = 3$  Hz,  $\varepsilon_1 = 0.01$ ,  $\varepsilon_2 = 5 \times 10^{-5}$ . (a)  $\Pi_\rho = \Pi_\mu = 0$  in (3.6a); (b)  $\text{Re}_G = -4190$ .

1051 By contrast, it is very hard to produce a regular wave train below the AI limit via coherent  
 1052 inlet forcing. This is demonstrated in figure 20, which represents similar computations to  
 1053 figure 18, only that we have additionally applied a harmonic inlet perturbation at frequency  
 1054  $f_0^* = 3$  Hz, using  $\varepsilon_1 = 0.01$  and  $\varepsilon_2 = 5 \times 10^{-5}$  in (3.46). Although the applied coherent forcing  
 1055 produces a regular wave train in the aerostatic configuration (panel 20a), coalescence events  
 1056 cannot be avoided for  $\text{Re}_G = -4190$  (panel 20b). We have not shown the corresponding  
 1057 computation beyond the AI limit (see panel 21b for this), because it produces almost exactly  
 1058 the same wave train as in panel 18c.

1059 Figure 21 summarizes the wave characteristics of our different WRIBL-LW open-domain  
 1060 computations from figures 18 and 20 by plotting the maximum wave height  $h_{\max}$  versus the  
 1061 streamwise position  $x$ . Error bars represent the range of temporal variation of  $h_{\max}$  at a given  
 1062 position. We see that AI-induced wave selection allows to (1) reduce the maximum wave  
 1063 height in the lower portion of the domain by about 40%, and (2) to suppress its variance  
 1064 over the entire domain length. For completeness, the pentagons in panel 21b report results  
 1065 from our computation with additional coherent inlet forcing for the parameters in panel 18c,  
 1066 i.e. beyond the AI limit, evidencing that the wave train is not meaningfully altered by this  
 1067 additional forcing.

#### 1068 6.1.4. Standing ripples in a vertically-falling liquid film

1069 Our nonlinear spatio-temporal WRIBL-LW computations in section 6.1.3 did not reveal any  
 1070 evidence of the gas-induced oscillatory secondary instability (OI) discovered by Lavalle *et al.*  
 1071 (2020) for the configuration of a vertically falling liquid film sheared by a superconfined  
 1072 counter-current laminar gas flow. In a spatially evolving regular train of surface waves  
 1073 formed by coherent inlet forcing at frequency  $f_0$ , this instability leads to a periodic spatial  
 1074 modulation of the wave height, which entails an intensification of mixing.

1075 To check whether this dynamics can be recovered in our current weak-confinement  
 1076 setting with a turbulent counter-current gas flow, we perform open-domain WRIBL-LW  
 1077 computations for the same liquid-side parameters as in figure 3a of Lavalle *et al.* (2020), i.e.  
 1078  $\text{Ka} = 509.5$ ,  $\phi = 90^\circ$ ,  $\text{Re}_L = 15$ , and  $f_0^* = 16$  Hz. Further, we set  $\varepsilon_1 = 0.01$  and  $\varepsilon_2 = 0$  in (3.46), and  
 1079 we apply the counter-current gas flow over the entire domain length  $L^* = 0.84$  m. In terms of  
 1080 confinement, we set  $H^* = 10$  mm, in contrast to  $H^* = 1$  mm used by Lavalle *et al.* (2020). The  
 1081 forcing frequency  $f_0^* = 16$  Hz corresponds to the linearly most-amplified value in the limit  
 1082 ( $\Pi_\rho = \Pi_\mu = 0$ ), which is quite different from the AI frequency  $f_{\text{AI}}^* = 26.8$  Hz, as obtained from  
 1083 our WRIBL-LW model. We search for signs of the OI by increasing  $|\text{Re}_G|$ .

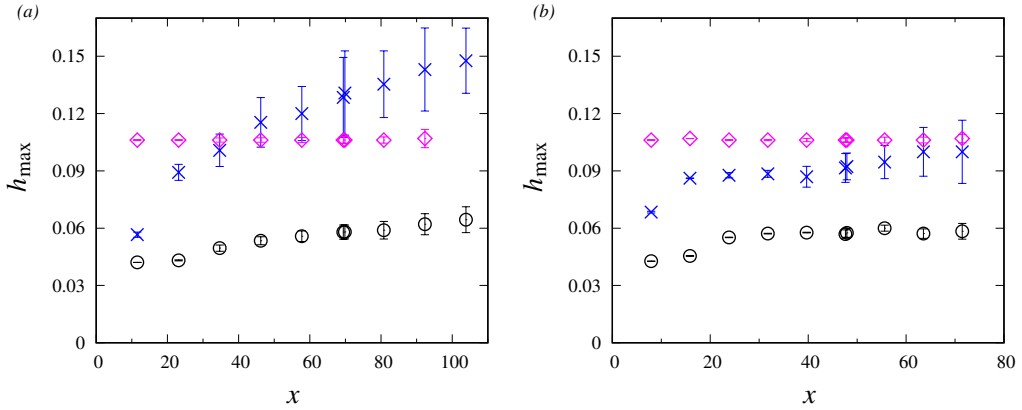


Figure 21: Summary of wave data from our computations in figures 18 and 20. Maximum wave height  $h_{\max}$  versus the streamwise location. Circles:  $\Pi_\rho = \Pi_\mu = 0$ ; crosses:  $\text{Re}_G = -4190$ ; diamonds:  $\text{Re}_G = -5750$ . Naturally-evolving versus forced waves. (a) Noisy inlet perturbation:  $\varepsilon_1 = 0$ ,  $\varepsilon_2 = 5 \times 10^{-5}$  in (3.46); (b) additional coherent inlet forcing:  $f_0^* = 3.0$  Hz,  $\varepsilon_1 = 0.01$ ,  $\varepsilon_2 = 5 \times 10^{-5}$  in (3.46).

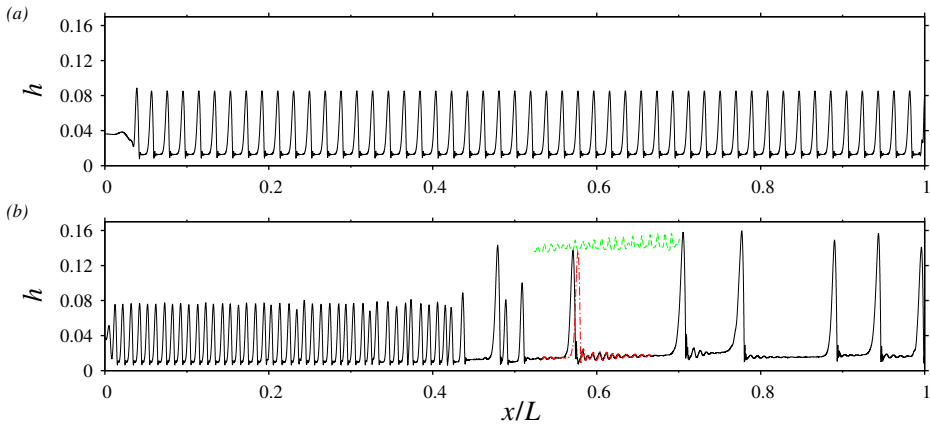


Figure 22: Vertically-falling liquid film sheared by a turbulent counter-current gas flow. Liquid-side conditions according to panel 3a in Lavalle *et al.* (2020):  $\text{Ka} = 509.46$  (DMSO-water and air II in table 1),  $\text{Re}_L = 15$ ,  $f_0^* = 16$  Hz,  $\text{Re}_G^{\text{AI}} = -6500$ . WRIBL computation on an open domain of length  $L^* = 0.843$  m. Snapshots of the film height profile  $h(x)$  at  $f_0 t = 61.4$ . (a) At AI limit:  $\text{Re}_G = \text{Re}_G^{\text{AI}} = -6500$ ; (b) beyond AI limit:  $\text{Re}_G = -7500$ . Dot-dashed red:  $f_0 t = 61.6$ , green dashed: Lagrangian path of a wave crest.

1084 Figure 22 reports results of computations for two values of  $|\text{Re}_G|$ . The first computation  
 1085 (panel 22a) corresponds exactly to the AI limit  $\text{Re}_G = \text{Re}_G^{\text{AI}} = -6500$  and represents the same  
 1086 features as other computations at lower  $|\text{Re}_G|$  (not shown here): an unaltered regular wave  
 1087 train of frequency  $f = f_0$  persists over the entire domain length.

1088 In the second computation (panel 22b), where the AI limit has been surpassed ( $\text{Re}_G = -$   
 1089 7500), a more interesting dynamics unfolds. Here, a quite regular wave train of frequency  
 1090  $f = f_{\text{AI}}$  emerges near the liquid inlet, as a result of linear wave selection at the AI frequency.  
 1091 However, the coherent inlet forcing at frequency  $f_0$  competes with this wave selection, leading  
 1092 to a slight perturbation of the wave train, which grows spatially and eventually disrupts the  
 1093 wave train. As a result, large-amplitude tsunami waves form due to coalescence events. These  
 1094 waves travel extremely fast and absorb all smaller waves travelling in front.

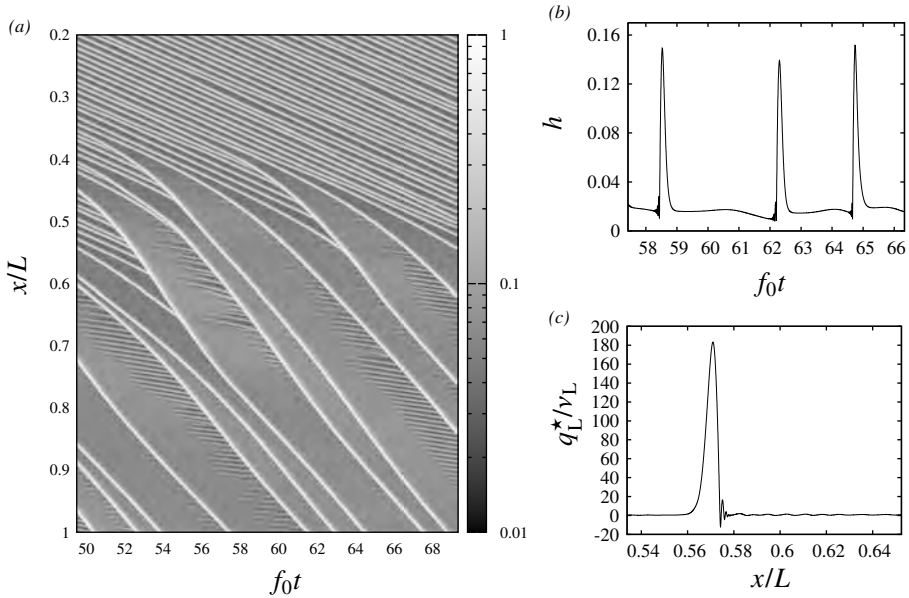


Figure 23: Standing ripples beyond the AI limit  $\text{Re}_G^{\text{AI}}=-6500$ . Computation from panel 22b:  $\text{Re}_G=-7500$ . (a) Spatio-temporal diagram of the normalized film height  $h/h_{\max}$ ; (b) film height time trace  $h(t)$  at  $x/L=0.6$ ; (c) spatial profile of the liquid flow rate  $q_L(x)$  at  $f_0 t=61.4$ .

1095 This gas-induced coarsening dynamics, which is well illustrated by the spatio-temporal  
 1096 diagram in panel 23a, leads to long portions of thin residual film in between two consecutive  
 1097 tsunami waves. There, the liquid flow rate  $q_L(x, t)$  is very small (see  $q_L$  profile in panel 23c),  
 1098 and thus  $|\text{Re}_G|$  is even further beyond the AI limit than for the primary flow  $q_{L0}$ . This leads to  
 1099 the formation of small-amplitude ripples on the residual film. We call these *standing ripples*  
 1100 because they are almost fixed in space, as evidenced by several features in figures 22 and 23.

1101 Firstly, the dot-dashed red profile segment in panel 22b, which corresponds to a slightly  
 1102 later time than the main profile, shows no significant translation of the ripples. Secondly,  
 1103 the wave fronts of the standing ripples in the spatio-temporal plot in panel 23a are almost  
 1104 horizontal. Thirdly, the film height time trace in panel 23b does not show any signature of  
 1105 the ripples in between two main wave humps.

1106 The standing ripples are felt like a surface roughness by the tsunami waves propagating  
 1107 over the residual film. This leads to a spatial modulation of the film height  $h_{\max}$ , similar to  
 1108 falling liquid films flowing on a corrugated substrate (Dietze 2019), where they have been  
 1109 shown to intensify mixing and inter-phase mass transfer. This modulation is evidenced by  
 1110 the dashed green curve in panel 22b, which represents the Lagrangian path of the crest of  
 1111 one of the tsunami waves as it propagates through the domain. The absolute nature of the  
 1112 standing ripples and their interaction with the large tsunami waves is further illustrated in the  
 1113 supplementary movie [MovieFig23](#).

1114 In conclusion, although we have not found any sign of the OI reported by Lavalley *et al.*  
 1115 (2020) for our confinement level, we nonetheless observe a similar gas-induced spatial  
 1116 modulation of the Kapitza waves, albeit due to an entirely different mechanism.

## 1117 6.2. Upward-travelling ripples: a new short-wave instability

1118 We now turn to the upward-travelling ripples observed for  $|\text{Re}_G| \gtrsim 6200$  in our experiment  
 1119 of figure 10 (see last eight panels there). These ripples eventually lead to a breakdown of

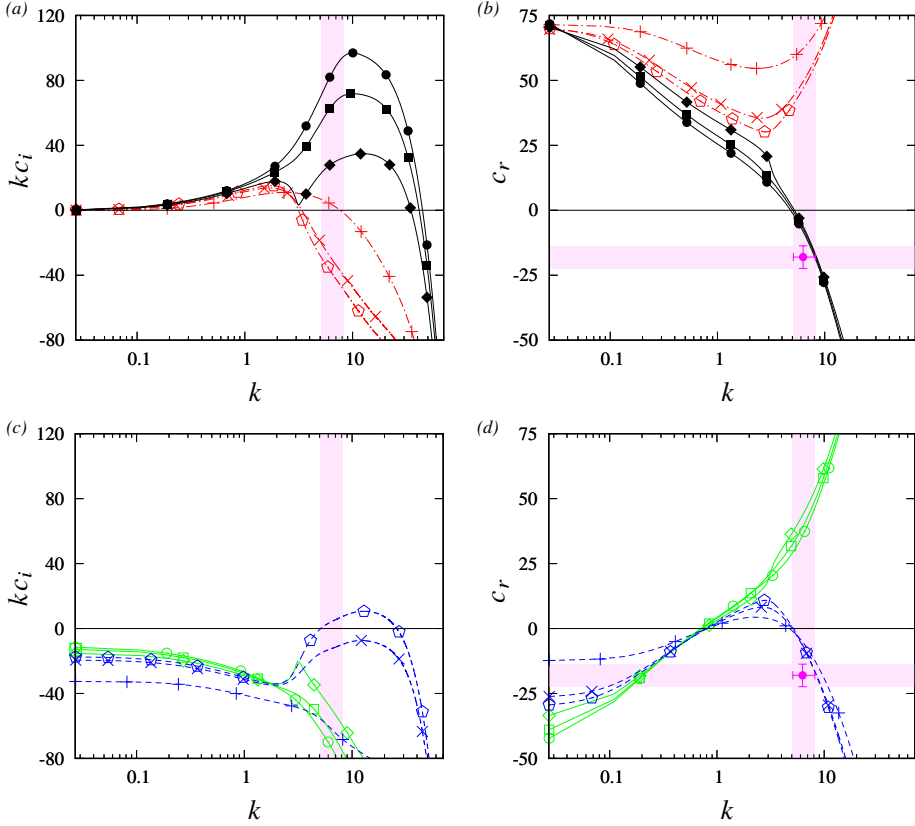


Figure 24: New short-wave instability mode. Falling liquid film sheared by a turbulent counter-current gas flow:  $Ka=3174$  (water and air I in table 1),  $H^*=13$  mm,  $\phi=5^\circ$ ,  $Re_L=43.1$ ,  $Re_G^{AI}=-5182$ . Temporal linear stability predictions using the OS-OS approach. Dashed blue: new short-wave mode, dot-dashed red: long-wave Kapitza mode, solid black with filled symbols: unstable merged mode, solid green with open symbols: stable merged mode. Pluses:  $\Pi_\rho=\Pi_\mu=0$  in (3.41); crosses:  $Re_G=-4700$ ; pentagons:  $Re_G=-5200$ ; diamonds:  $Re_G=-5750$ ; squares:  $Re_G=-6400$ ; circles:  $Re_G=-6760$ . (a,c) Growth rate; (b,d) wave speed. Shaded magenta bands and filled magenta circle with error bars represent our experiment from figure 10:  $Re_L=43.1$ ,  $Re_G=-6760$ ,  $\Lambda_{ripples}^*=(13 \pm 3)$  mm,  $c_{ripples}^*=(-6.2 \pm 1.5)$  cm s $^{-1}$ .

1120 our experiment due to the accumulation of liquid droplets in the gas loop, and, thus, can  
 1121 be considered as the onset of flooding. In the current section, we seek to identify the origin  
 1122 of these ripples via linear stability calculations using our OS-OS approach, which allows to  
 1123 capture long- and short-wave instability modes.

1124 Figure 24 represents temporal OS-OS linear stability predictions for parameters from the  
 1125 experiment. The different symbols correspond to five different values of  $Re_G$ , according  
 1126 to the 4<sup>th</sup> ( $Re_G=-4700$ ), 5<sup>th</sup> ( $Re_G=-5200$ ), 7<sup>th</sup> ( $Re_G=-5750$ ), 12<sup>th</sup> ( $Re_G=-6400$ ), and 17<sup>th</sup>  
 1127 ( $Re_G=-6760$ ) panel in figure 10. The last panel in figure 10 ( $Re_G=-6830$ ) corresponds to the  
 1128 breakdown of our experiment, and is not considered here.

1129 Panels 24a and 24c represent growth rate dispersion curves for different instability modes  
 1130 and panels 24b and 24d the corresponding dispersion curves for the linear wave speed.  
 1131 We have separated the different plots into two panel pairs in order to better distinguish  
 1132 the different modes. Red dot-dashed curves in panel 24a belong to the long-wave Kapitza

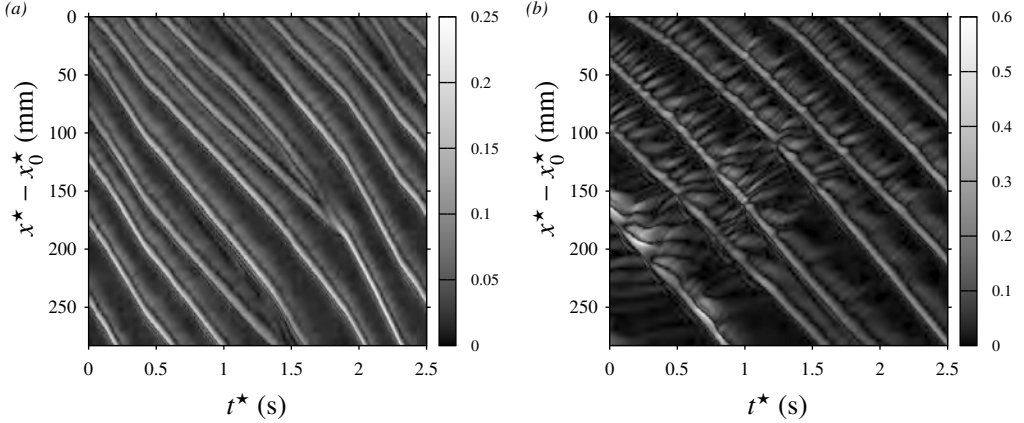


Figure 25: First signature of upward-travelling ripples in our experiments. Spatio-temporal diagrams of the film surface slope  $\|\nabla h\|$  for parameters in figure 10, obtained with the synthetic Schlieren technique (Kofman *et al.* 2014):  $H^*=13$  mm,  $\phi=5^\circ$ ,  $\text{Re}_L=43.1$ ,  $f_0^*=3$  Hz,  $x_0^*=48$  cm,  $z^*=13$  cm. (a)  $\text{Re}_G=-5200$ : ripples start to appear in between Kapitza wave humps; (b)  $\text{Re}_G=-6080$ : ripples deform crests of Kapitza waves.

1133 mode, which we have discussed in section 6.1. The growth rate of this mode increases with  
 1134 increasing  $|\text{Re}_G|$  (from pluses to pentagons), while its cut-off wave number decreases.

1135 The blue dashed curves in panel 24c belong to a new short-wave instability mode, which  
 1136 emerges upon increasing  $|\text{Re}_G|$  beyond  $|\text{Re}_G|=4837$  (between crosses and pentagons). We  
 1137 call this new instability mode a short-wave mode, because the growth rate  $kc_i$  is positive  
 1138 only within a finite span of the wavelength  $\Lambda=2\pi/k$ , and because the maximum growth rate  
 1139 is observed at a large wave number, i.e.  $k_{\max}\sim 10$  versus  $k_{\max}\sim 2$  for the long-wave Kapitza  
 1140 instability mode. The short-wave mode appears for  $|\text{Re}_G|\gg 1800$ , and this suggests that  
 1141 turbulence in the gas is required to generate this instability mode. This may explain why  
 1142 previous stability investigations (Schmidt *et al.* 2016; Trifonov 2017), where the gas flow  
 1143 was assumed laminar, did not find the short-wave mode.

1144 At  $\text{Re}_G=-5200$  (pentagons in figure 24), the growth rate of the short-wave mode (panel  
 1145 24c) has surpassed that of the Kapitza mode (panel 24a). However, our experiments in figure  
 1146 10 do not show any clear signature of the short-wave mode, except maybe slight modulations  
 1147 on the crests of the first two wave fronts (see e.g. 8th panel in figure 10). This can be  
 1148 attributed to the protected zone in our current experimental setup, where Kapitza waves are  
 1149 allowed to develop in a virtually quiescent atmosphere, before entering the gas-sheared zone.  
 1150 In other words, the gas-induced short-wave instability mode has to compete with saturated  
 1151 fully-nonlinear Kapitza waves. We demonstrate this via an additional set of experiments that  
 1152 was focused on detecting the first signs of ripples for the parameters in figure 10. Figure 25  
 1153 shows spatio-temporal diagrams of the film surface slope obtained from these experiments,  
 1154 using the synthetic Schlieren technique (Moisy *et al.* 2009; Kofman *et al.* 2014). In panel  
 1155 25a,  $\text{Re}_G=-5200$ , wave fronts of upward-travelling ripples are clearly visible in between  
 1156 downward-travelling Kapitza waves. However, these ripples cannot yet compete with the  
 1157 large-amplitude Kapitza wave humps, and thus remain hidden in the dark inter-wave regions  
 1158 of figure 10.

1159 Upon increasing  $\text{Re}_G$  further (diamonds in figure 24), the short-wave mode and the Kapitza  
 1160 mode merge into a new unstable merged mode (open diamonds in panel 24a), which initially  
 1161 displays a two-humped growth rate dispersion curve, and a new stable merged mode (filled  
 1162 diamonds in panel 24c). Panel 26a shows the merging of the growth rate curves in detail.  
 1163 According to this, the long-wave portion of the long wave mode (red dot-dashed curves)



1164 merges with the short-wave portion of the short-wave mode (blue dashed curves), creating  
 1165 the unstable merged mode (solid black curve with filled diamonds). Vice versa, the short-  
 1166 wave portion of the long-wave mode merges with the long-wave portion of the short-wave  
 1167 mode, creating the stable merged mode (solid green curve with open diamonds).

1168 A direct consequence of the mode merging is a change in trend of the cut-off wave number  
 1169  $k_c$  versus  $\text{Re}_G$  when considering the growth rate curves originating at  $k=0$ ,  $kc_i=0$  in panel  
 1170 24a. Before the merging (pluses to pentagons), these curves are associated with the long-wave  
 1171 Kapitza instability, and  $k_c$  decreases with increasing  $|\text{Re}_G|$ . After the merging (diamonds to  
 1172 circles),  $k_c$  jumps to a much greater value and its trend is reversed. This could explain the  
 1173 sudden change in trend of the neutral stability bounds in figure 11 of Vellingiri *et al.* (2015),  
 1174 which we have reproduced with our WRIBL-OS approach in panel 29a of appendix A.

1175 As  $|\text{Re}_G|$  is increased beyond  $|\text{Re}_G|=5750$  in panel 24a (from diamonds to circles), the  
 1176 short-wave growth rate maximum of the unstable merged mode becomes dominant and  
 1177 attains very large values. It is here that upward-travelling ripples become strong enough to  
 1178 deform the crests of the Kapitza waves (see panel 25b), and thus become clearly visible  
 1179 in our experiments (last eight panels of figure 10). The shaded magenta band in panel 24a  
 1180 represents the experimental range of the wave number  $k$  for these ripples at  $\text{Re}_G=-6760$   
 1181 (next to last panel in figure 10), and this compares reasonably well with the most-amplified  
 1182 wave number  $k_{\max}$  of the corresponding unstable merged mode (curve with filled circles in  
 1183 figure 24a). Better agreement is expected without the protected region used in our current  
 1184 experimental setup. In our setup, short-wave ripples originate on the residual film in between  
 1185 two preexisting large-amplitude nonlinear Kapitza waves, which is not quite comparable to  
 1186 the primary flow underlying figure 24.

1187 The most important feature of the new short-wave instability mode observed in panels 24c  
 1188 and 24d is that it displays negative wave speeds ( $c_r < 0$  in panel 24d) in the range of unstable  
 1189 wave numbers. And, this property is endowed to the unstable merged mode in panel 24b. In  
 1190 particular, the linear wave speed  $c_r$  for  $\text{Re}_G=-6760$  (solid curve with open circles in panel  
 1191 24b) is negative across the entire wave number span of the upward-travelling ripples observed  
 1192 in the corresponding experiment (vertical shaded magenta band in panel 24b). Moreover,  
 1193 the ripple wave speed estimated from our experiments (filled magenta circle with error bars  
 1194 in panel 24b) agrees quite well with the linear wave speed. Thus, we are confident that the  
 1195 short-wave instability uncovered in figure 24 is at the origin of the upward-travelling ripples  
 1196 observed in our experiment of figure 10.

1197 Upward travelling linear waves linked to the short-wave mode, or the unstable merged  
 1198 mode, do not necessarily require a negative liquid velocity. This is shown in panel 26b,  
 1199 where we have plotted the primary-flow liquid velocity at the liquid-gas interface  $u_{L0}|_{y=h_0}$   
 1200 in terms of  $\text{Re}_G$  for the liquid-side parameters from figure 24. Here, we confront our current  
 1201 confinement (solid curve with symbols,  $H^*=13$  mm) with those of Kofman *et al.* (2017)  
 1202 (dot-dashed,  $H^*=19$  mm) and Mergui *et al.* (2023) (dashed,  $H^*=5$  mm). Focusing on the  
 1203 solid curve, where symbols mark  $|\text{Re}_G|$  values from panels 24b and 24d, we see that  $u_{L0}|_{y=h_0}$   
 1204 becomes negative far beyond the onset of the short-wave instability (between the square and  
 1205 circle in panel 26b). Thus, the gas-induced linear short waves can travel upward even though  
 1206 the liquid moves downward across the entire film thickness  $h_0$ .

1207 To further characterize the nature of the short-wave instability mode, figure 27 represents  
 1208 (normalized) profiles of the liquid-side (panel 27a) and gas-side (panel 27b) eigenfunctions,  
 1209  $\phi$  and  $\psi$  (4.13), for the most-amplified long-wave (red dot-dashed curves) and short-wave  
 1210 (blue dashed curves) instability modes at  $\text{Re}_G=-5200$  (pentagons in panels 24a and 24c).  
 1211 We see that  $\phi$  is maximal at the liquid gas interface,  $y=h_0$ , for both the long-wave and  
 1212 short-waves modes. We may thus conclude that the short-wave mode is an interfacial mode,



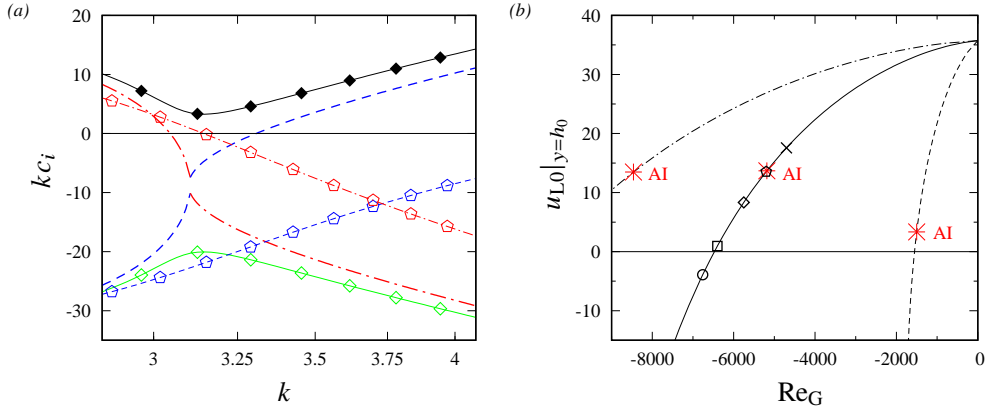


Figure 26: Details of OS-OS linear stability predictions from figure 24:  $Ka=3174$ ,  $Re_L=43.1$ ,  $H^*=13$  mm,  $\phi=5^\circ$ . (a) Merging between the short-wave and long-wave instability modes from panels 24a and 24c. Diamonds:  $Re_G=-5750$ , thick lines without symbols:  $-5680$ , pentagons:  $-5200$ ; (b) primary-flow liquid velocity at the film surface. Solid:  $H^*=13$  mm,  $Re_G^{AI}=-5182$ ; dot-dashed:  $H^*=19$  mm,  $Re_G^{AI}=-8461$ ; dashed:  $H^*=5$  mm,  $Re_G^{AI}=-1501$ . Asterisks indicate AI limit from WRIBL-OS spatial linear stability calculations.

1213 strengthening our assertion that it lies at the origin of the upward-travelling ripples observed in  
 1214 our experiments.

1215 Interestingly, the onset of the short-wave instability mode in panel 24c, i.e.  $Re_G=-5100$   
 1216 (between crosses and pentagons), is very close to the AI limit of the Kapitza instability  
 1217 observed in figure 12, i.e.  $Re_G^{AI}=-5115$ . This may explain why flooding predictions based on  
 1218 the AI limit (Vellingiri *et al.* 2015) are reasonably good, even though AI does not seem to  
 1219 produce any dangerous events in our experiments and nonlinear WRIBL-LW computations.

## 1220 7. Conclusion

1221 We have studied the effect of a confined turbulent counter-current gas flow on the linear and  
 1222 nonlinear dynamics of a wavy falling liquid film, focusing on regimes beyond the absolute  
 1223 instability (AI) limit of the Kapitza instability. We have done this via experiments and  
 1224 numerical computations based on a new low-dimensional model, which we have introduced  
 1225 and validated here. This model accurately captures the gas-induced transition to AI as well as  
 1226 the nonlinear gas-effect on travelling Kapitza waves. In addition, we have performed linear  
 1227 stability calculations based on the full Orr-Sommerfeld equations in the gas and the liquid.

1228 From our investigation, we may draw the following conclusions. (1) AI is not necessarily  
 1229 dangerous, i.e. no flooding events linked to Kapitza waves were observed even far beyond  
 1230 the AI limit. On the contrary, AI can act as an effective linear wave selection mechanism  
 1231 in a naturally evolving falling liquid film, leading to highly regular downward-travelling  
 1232 nonlinear waves, precluding dangerous coalescence events.

1233 (2) Flooding is eventually triggered by upward-traveling ripples, which were discovered  
 1234 in the experiments of Kofman *et al.* (2017) and reproduced here. We find that these ripples  
 1235 result from a short-wave interfacial instability associated with a negative linear wave speed.  
 1236 As far as we know, this short-wave instability has not yet been reported in the literature. On  
 1237 the contrary, the instability was not found in several previous stability investigations of falling  
 1238 liquid films (Schmidt *et al.* 2016; Trifonov 2017). In these investigations, the counter-current  
 1239 gas flow was assumed laminar, even though the gas Reynolds number  $Re_G$  was increased  
 1240 far beyond the turbulence threshold. We may thus surmise that Reynolds stresses associated

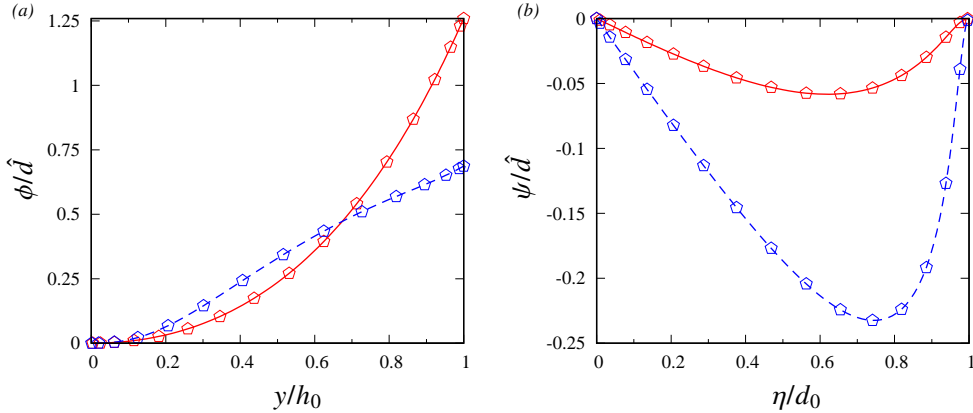


Figure 27: Eigenfunctions (4.13) for different instability modes from figure 24. Turbulent counter-current gas flow:  $\text{Re}_G = -5200$ . Linearly most-amplified short-wave (dashed blue lines,  $k=12.8$ ) and long-wave (solid red lines,  $k=1.6$ ) instability modes. (a) Liquid film,  $\phi$ ; (b) gas layer,  $\psi$ .

1241 with gas-side turbulence are essential for generating the short-wave instability, at least in the  
 1242 parameter range where ripples are observed experimentally.

1243 (3) The onset of the short-wave instability approximately coincides with the AI limit  
 1244 of the long-wave Kapitza instability. This could explain why predictions of the flooding  
 1245 threshold based on the AI limit have been found to agree reasonably well with experiments  
 1246 (Vellingiri *et al.* 2015), even though the trends of these two thresholds w.r.t. to the liquid  
 1247 Reynolds number are opposed.

1248 (4) At larger counter-current gas flow rates, the short-wave instability mode merges with  
 1249 the long-wave Kapitza mode, leading to a sudden and drastic increase of the cut-off wave  
 1250 number. This may explain the sudden change in the  $\theta$ -trend of the neutral stability curves  
 1251 reported in figure 11 of Vellingiri *et al.* (2015), which we have reproduced in figure 29a  
 1252 based on our own computations.

1253 (5) Absolute instability of the long-wave Kapitza mode and instability of the new short-  
 1254 wave mode can coincide in a certain parameter range (see panels 12a and 24c). It remains  
 1255 to be seen, how downward-travelling long waves generated by AI interact/compete with  
 1256 upward-travelling ripples generated by the short-wave instability in a naturally evolving  
 1257 falling liquid film. Unraveling the interaction between these two wave types, may be the key  
 1258 to understanding flooding in gas-sheared falling liquid films. In our current experiments, this  
 1259 could not be studied, as fixed-frequency saturated-amplitude nonlinear waves were allowed  
 1260 to develop in a protected region, before entering into contact with the counter-current gas  
 1261 flow. In this configuration, Kapitza waves are privileged until the growth rate of the merged  
 1262 instability mode (panel 24a) becomes dominant and upward-travelling ripples appear.

1263 Conversely, computations with our current WRIBL-LW model cannot capture the new  
 1264 short-wave instability. Although this is a limitation of the model, it allowed us to show that the  
 1265 long-wave AI alone does not produce any catastrophic events. An interesting goal for future  
 1266 work is to extend our model to overcome this limitation. For this, the gas-side representation,  
 1267 which currently relies on an  $O(\epsilon)$  long-wave approximation, needs to be improved. This will  
 1268 require relaxing our symmetry condition (3.13b). Velocimetry experiments similar to those  
 1269 of Cohen & Hanratty (1968), would allow to gauge the extent of asymmetry in the gas flow.

1270 By contrast, our  $O(\epsilon^2)$  liquid-side WRIBL representation is capable of capturing short  
 1271 waves, as evidenced by the precursory capillary ripples in figure 9, which have a smaller  
 1272 wavelength than the upward-travelling ripples. Also, our comparisons between WRIBL-OS

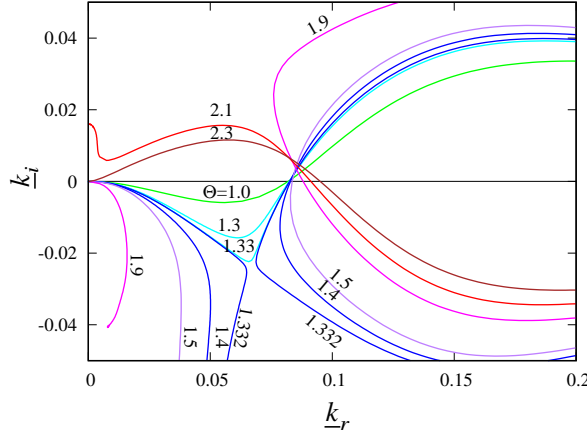


Figure 28: Validation of our WRIBL-OS approach (section 4.1). Spatial linear stability predictions for parameters in figure 15 of Vellingiri *et al.* (2015):  $Ka=2000$  (methanol and helium in table 1),  $\phi=90^\circ$ ,  $Re_0=3Re_L/\sin(\phi)=10$ ,  $H^*=30$  mm,  $\Pi_\rho=0$ , (3.6a) truncated at  $O(\epsilon)$ . Quantities are scaled with  $\underline{\mathcal{L}}=h_0^*$  and  $\underline{\mathcal{U}}=h_0^{*2}g \sin(\phi)/2\nu_L$ . The counter-current gas shear stress is quantified via  $\Theta=T_{G0}^*|\underline{\mathcal{L}}/\mu_L/\underline{\mathcal{U}}$ .

1273 and OS-OS linear stability calculations show good agreement (figures 6), including for the  
1274 short wave mode (figure 30).

1275 Finally, a detailed study of the new short-wave instability is necessary, and we intend to  
1276 pursue our work in this direction. For example, it should be verified whether the instability  
1277 also occurs for the conditions studied by Trifonov (2017) and Schmidt *et al.* (2016). And, the  
1278 mechanism of the instability should be elucidated. For example, how does it compare to the  
1279 Kelvin-Helmholtz instability and the generation of wind-driven waves?

## 1280 Appendix A. Validation of WRIBL-OS and OS-OS approaches

1281 In figure 28, we have used our WRIBL-OS approach from section 4.1 to reproduce the  
1282 growth rate dispersion curves obtained from temporal linear stability analysis in figure  
1283 15 of Vellingiri *et al.* (2015), for a vertically-falling liquid film sheared by an unconfined  
1284 counter-current turbulent gas flow. To recover the formulation used in that reference, we have  
1285 truncated our liquid-side WRIBL model (3.6a) at  $O(\epsilon)$ , set  $\Pi_\rho=0$ , and increased  $H^*$  until  
1286 it no longer affected our results. All quantities in figure 28 have been scaled with  $\underline{\mathcal{L}}=h_0^*$   
1287 and  $\underline{\mathcal{U}}=h_0^{*2}g \sin(\phi)/2\nu_L$ , according to Vellingiri *et al.* (2015). Thus, results are directly  
1288 comparable with data in figure 15 of that reference, exhibiting very good agreement.

1289 In figure 29, we have used our OS-OS approach from section 4.2 to reproduce several  
1290 temporal linear stability predictions from Vellingiri *et al.* (2015) and Schmidt *et al.* (2016). In  
1291 panel 29a, we have reproduced the neutral stability predictions in figure 11 of Vellingiri *et al.*  
1292 (2015), where a vertically-falling liquid film sheared by an unconfined turbulent counter-  
1293 current gas flow was considered. Crosses correspond to our OS-OS prediction and open  
1294 circles to calculations of Vellingiri *et al.* (2015). In the same figure, we have also plotted  
1295 predictions obtained from our WRIBL-OS approach (curves). To reproduce the unconfined  
1296 configuration considered in Vellingiri *et al.* (2015), we have once again increased  $H^*$  until  
1297 it no longer meaningfully affected our results.

1298 Agreement between crosses and circles in panel 29a is good, except for data at  
1299  $\Theta=T_{G0}^*\underline{\mathcal{L}}/\mu_L/\underline{\mathcal{U}}=3$ . This is where the trend of the cut-off wave number  $k$  in terms of the

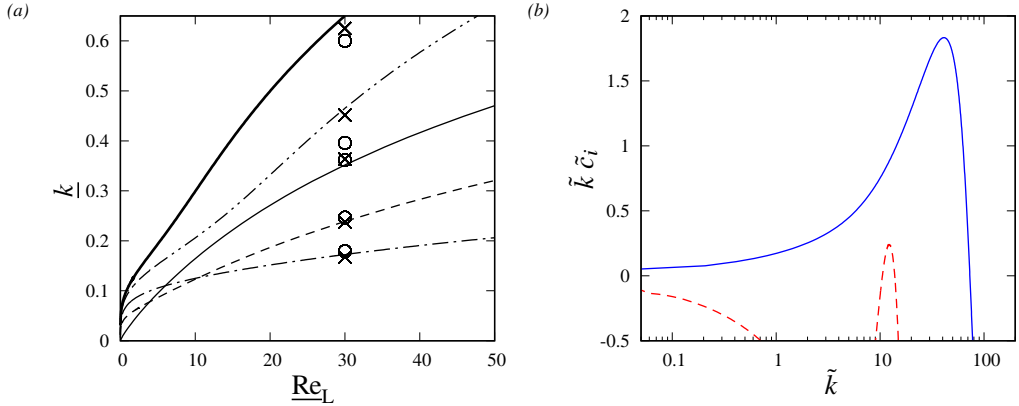


Figure 29: Validation of our WRIBL-OS (section 4.1) and OS-OS (section 4.2) approaches. Temporal linear stability predictions for a gas-sheared vertically-falling liquid film. (a) Neutral stability curves for parameters according to figure 11 in Vellingiri *et al.* (2015):  $Ka=2000$ ,  $H^*=300$  mm. Crosses: OS-OS; solid lines: WRIBL-OS; open circles: data from Vellingiri *et al.* (2015). Thin solid:  $\Theta=0$ ; dashed:  $\Theta=1$ ; dot-dashed:  $\Theta=2$ ; dot-dot-dashed:  $\Theta=3$ ; thick solid:  $\Theta=3.5$ . Same scaling as in figure 28; (b) growth rate dispersion curves for parameters according to panel 4e in Schmidt *et al.* (2016):  $H^*=10$  mm,  $\rho_L=1000$  kg/m<sup>3</sup>,  $\mu_L=0.5 \times 10^{-3}$  Pa s,  $\rho_G=1$  kg/m<sup>3</sup>,  $\mu_G=1 \times 10^{-6}$  Pa s,  $\sigma=1$  mN m<sup>-1</sup>,  $\delta_L=h_0^*/H^*=0.08$ ,  $\tilde{Fr}=\tilde{U}/\sqrt{g\tilde{L}}=3$ ,  $Re_L=6166$ ,  $Re_G=48322$ . Tildes indicate scaling with  $\tilde{L}=H^*$  and  $\tilde{U}=[\partial_x P_{G0}^* H^*/\rho_G]^{1/2}$ . Solid blue: long-wave Kapitza mode; dashed red: short-wave Tollmien-Schlichting mode.

1300 dimensionless gas shear stress  $\Theta$  changes. We believe that this is the result of the mode  
 1301 merging that we have observed in section 6.2. At thresholds where the stability behavior  
 1302 changes, large discrepancies between two calculations may occur as a result of small  
 1303 differences between the employed procedures. In particular, we have used a different set  
 1304 of curvilinear coordinates than Vellingiri *et al.* (2015). We believe that this explains the  
 1305 discrepancy between the cross and circle for  $\Theta=3$ .

1306 Interestingly, we have observed that our OS-OS predictions in panel 29a change signifi-  
 1307 cantly when setting  $\Pi_\rho=0$  (not shown). This confirms our conclusion based on equation (5.5)  
 1308 that  $P_G$  can affect stability even in the unconfined limit.

1309 In panel 29b, we have reproduced with our OS-OS approach the growth rate dispersion  
 1310 curves in figure 4e of Schmidt *et al.* (2016), where a vertically-falling liquid film sheared by a  
 1311 confined laminar ( $\tilde{l}_t=0$  in equations 3.27 and 3.28) counter-current gas flow was considered.  
 1312 All quantities have been scaled with  $\tilde{L}=H^*$  and  $\tilde{U}=[\partial_x P_{G0}^* H^*/\rho_G]^{1/2}$ , according to  
 1313 Schmidt *et al.* (2016). Thus, results are directly comparable with data in figure 4e of that  
 1314 reference, exhibiting very good agreement, both for the long-wave Kapitza mode (solid blue  
 1315 curve) and the Tollmien-Schlichting mode (dashed red curve).

## 1316 Appendix B. Neutral stability bound based on equation (5.2)

1317 In (5.2), we have introduced the first-order contribution  $c_1$ , arising in the long-wave expansion  
 1318 ( $k \rightarrow 0$ ) of the linear wave speed  $c$ :

$$1319 \quad c = c_0 + kc_1 + O(k^2),$$

$$1320 \quad c_1 = i\mathcal{R}.$$

1321 The neutral stability bound is given by  $\mathcal{R}=0$ , and the solution for  $\mathcal{R}$  obtained from our  
1322 WRIBL-LW model (3.6) is:

$$\begin{aligned}
 1323 \quad \mathcal{R} = & \frac{1}{3} \cos(\phi) \frac{\text{Re}_L}{\text{Fr}^2} h_0^3 \left\{ -1 + \frac{\Pi_\rho}{\Pi_u^2} \right\} & (B 1) \\
 1324 \quad & + \frac{\sin^2(\phi)}{\text{Fr}^4} \text{Re}_L^3 \left\{ \frac{2}{15} h_0^6 + \frac{2}{5} \frac{\Pi_\rho^2}{\Pi_u^4} \frac{h_0^8}{d_0^2} + \frac{10}{21} \frac{\Pi_\rho}{\Pi_u^2} \frac{h_0^7}{d_0} \right\} \\
 1325 \quad & + \Pi_\mu \frac{\sin(\phi)}{\text{Fr}^2} \text{Re}_L^2 T_{G0} \left\{ \frac{\Pi_\rho}{\Pi_u} \left[ \frac{7}{24} \frac{h_0^6}{d_0} + \frac{4}{5} \frac{h_0^7}{d_0^2} \right] + \Pi_u \left[ \frac{2}{15} h_0^5 + \frac{10}{21} \frac{h_0^6}{d_0} \right] \right\} \\
 1326 \quad & + \Pi_\mu^2 \Pi_u^2 \text{Re}_L T_{G0}^2 \left\{ \frac{7}{24} \frac{h_0^5}{d_0} + \frac{2}{5} \frac{h_0^6}{d_0^2} \right\} \\
 1327 \quad & - \Pi_\mu \Pi_\rho \frac{\text{Re}_L}{\text{Re}_G} \Pi_u^3 T_{G0} \partial_x P_{G0} \left\{ \frac{2}{15} h_0^5 + \frac{43}{56} \frac{h_0^6}{d_0} + \frac{4}{5} \frac{h_0^7}{d_0^2} \right\} \\
 1328 \quad & - \frac{\sin(\phi)}{\text{Fr}^2} \frac{\text{Re}_L^3}{\text{Re}_G} \partial_x P_{G0} \left\{ \Pi_\rho^2 \left[ \frac{10}{21} \frac{h_0^7}{d_0} + \frac{4}{5} \frac{h_0^8}{d_0^2} \right] + \Pi_\rho \Pi_u^2 \left[ \frac{4}{15} h_0^6 + \frac{10}{21} \frac{h_0^7}{d_0} \right] \right\} \\
 1329 \quad & + \frac{\text{Re}_L^3}{\text{Re}_G^2} \Pi_\rho^2 \Pi_u^2 \partial_x P_{G0}^2 \left\{ \frac{2}{15} h_0^6 + \frac{10}{21} \frac{h_0^7}{d_0} + \frac{2}{5} \frac{h_0^8}{d_0^2} \right\} \\
 1330 \quad & + \frac{1}{2} \Pi_\mu \Pi_u \frac{h_0^2}{d_0} \partial_\eta U_1|_{d_0} + \frac{1}{3} \Pi_\rho \Pi_u^2 \text{Re}_L \frac{h_0^3}{d_0} C_1, \\
 1331
 \end{aligned}$$

1332 where  $C_1$  and  $U_1$  are obtained by solving (3.27) and (3.28). Solutions for  $C_1$  and  $\partial_\eta U_1|_{d_0}$  in  
1333 the laminar limit are given in (5.5).

### 1334 Appendix C. Accounting for derivatives of $T_G$ and $P_G$ in (3.6a)

1335 We check to what extent the temporal and spatial derivatives of  $T_G$  and  $P_G$ , which appear in  
1336 (3.6a) and which we have neglected in our WRIBL-LW and WRIBL-OS computations, play  
1337 a role in the linear stability of a gas-sheared falling liquid film. Figure 30 represents linear  
1338 stability predictions obtained with three approaches for conditions according to figure 24.  
1339 Solid curves correspond to OS-OS calculations based on (4.20) and (4.21), dot-dashed curves  
1340 to WRIBL-OS calculations based on (3.41), and dashed curves to WRIBL-OS calculations  
1341 with account of the space and time derivatives of  $T_G$  and  $P_G$  in (3.6a).

1342 According to this, both WRIBL approaches accurately capture the gas-effect on the long-  
1343 wave Kapitza instability mode (red curves in panel 30a), and accounting for the derivatives  
1344 of  $T_G$  and  $P_G$  does not bear much benefit. By contrast, not surprisingly, the growth rate of  
1345 the new short-wave mode is less well predicted by both WRIBL approaches (blue curves in  
1346 panel 30a). Here, accounting for the derivatives of  $T_G$  and  $P_G$  (dashed blue curve) improves  
1347 predictions at intermediate  $k$ , but the standard WRIBL-OS approach performs better at large  
1348  $k$ . Finally, both WRIBL approaches produced quite good predictions of the merged instability  
1349 mode (panel 30b), whereby the standard WRIBL-OS approach behaves better.

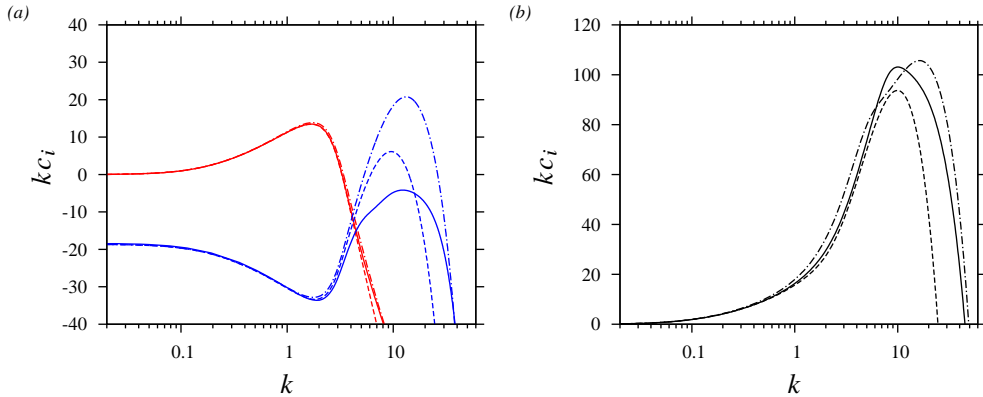


Figure 30: Accounting for temporal and spatial derivatives of  $T_G$  and  $P_G$  in (3.6a). Temporal linear stability predictions based on three approaches for conditions according to figure 24:  $Ka=3174$  (water and air I in table 1),  $H^*=13$  mm,  $\phi=5^\circ$ ,  $Re_L=43.1$ . Dot-dashed: WRIBL-OS (3.41), solid: OS-OS (4.20) and (4.21), dashed: WRIBL-OS including derivatives of  $T_G$  and  $P_G$  in (3.6a). (a)  $Re_G=-4700$ . Red: long-wave Kapitza mode, blue: short-wave mode; (b)  $Re_G=-6760$ : merged mode.

1350 In summary, accounting for the derivatives of  $T_G$  and  $P_G$  does not meaningfully improve  
 1351 predictions at low wave numbers  $k$ . And, at large  $k$ , it may even deteriorate them. This is  
 1352 because the WRIBL-OS description becomes unbalanced at large  $k$ , as a result of truncating  
 1353 the governing equations at different orders in the liquid (truncate at  $O(\epsilon^2)$  and neglect  
 1354  $O(\epsilon^2 Re_L)$  inertial corrections) and gas (full governing equations). Retaining supplementary  
 1355 terms in the governing equations has been shown to deteriorate long-wave model predictions  
 1356 in other configurations (Oron & Gottlieb 2004; Thompson *et al.* 2019). It is interesting to  
 1357 note that both the new short-wave (panel 30a) and merged (panel 30b) instability modes can  
 1358 be captured by the WRIBL approach.

1359 **Acknowledgements.** Johannes Amrani, Alban Aubertin, Lionel Auffray, and Rafael  
 1360 Pidoux contributed to building the experimental setup.

1361 **Declaration of Interests.** The authors report no conflict of interest.

## REFERENCES

- 1362 ALEKSEENKO, S. V., AKTERSHEV, S. P., CHERDANTSEV, A. V., KHARLAMOV, S. M. & MARKOVICH, D. M.  
 1363 2009 Primary instabilities of liquid film flow sheared by turbulent gas stream. *International Journal*  
 1364 *of Multiphase Flow* **35**, 617–627.
- 1365 ALEKSEENKO, S. V., ANTIPIN, V. A., BOBYLEV, A. V. & MARKOVICH, D. M. 2007 Application of PIV to  
 1366 velocity measurements in a liquid film flowing down an inclined cylinder. *Experiments in Fluids*  
 1367 **43** (2-3), 197–207.
- 1368 AZZOPARDI, B. J., MUDE, R. F., LO, S., MORVAN, H., YAN, Y. & ZHAO, D. 2011 *Hydrodynamics of*  
 1369 *Gas-Liquid Reactors: Normal Operation and Upset Conditions*. John Wiley & Sons.
- 1370 BANKOFF, S. G. & LEE, S. C. 1986 *A critical review of the flooding literature*, vol. 2, pp. 95–180. Springer  
 1371 Berlin Heidelberg.
- 1372 BARMAN, I., GELFGAT, A., ULLMAN, A. & BRAUNER, N. 2016a Stability of stratified two-phase flows in  
 1373 inclined channels. *Physics of Fluids* **28**, 084101.
- 1374 BARMAN, I., GELFGAT, A., VITOSHKIN, H., ULLMAN, A. & BRAUNER, N. 2016b Stability of stratified two-phase  
 1375 flows in horizontal channels. *Physics of Fluids* **28**, 044101.
- 1376 BOOMKAMP, P. A. M., BOERSMA, B. J., MIESEN, R. H. M. & BEIJNON, G. V. 1997 A Chebyshev collocation  
 1377 method for solving two-phase flow stability problems. *Journal of Computational Physics* **132**, 191–  
 1378 200.

- 1379 BROOKE BENJAMIN, T. 1957 Wave formation in laminar flow down an inclined plane. *J. Fluid Mech.* **2**,  
1380 554–574.
- 1381 BROOKE BENJAMIN, T. 1959 Shearing flow over a wavy boundary. *J. Fluid Mech.* **6**, 161–205.
- 1382 CAMASSA, R., OGROSKY, H. R. & OLANDER, J. 2017 Viscous film-flow coating the interior of a vertical tube.  
1383 part 2. air-driven flow. *Journal of Fluid Mechanics* **825**, 1056–1090.
- 1384 CHANG, H. C., DEMEKHIN, E. A. & KALALIDIN, E. 1996a Simulation of noise-driven wave dynamics on a  
1385 falling film. *AIChE J.* **42** (6), 1553–1568.
- 1386 CHANG, H. C., DEMEKHIN, E. A., KALALIDIN, E. & YE, Y. 1996b Coarsening dynamics of falling-film solitary  
1387 waves. *Phys. Rev. E* **54** (2), 1467–1477.
- 1388 COHEN, L. S. & HANRATTY, T. J. 1968 Effect of waves at a gas—liquid interface on a turbulent air flow.  
1389 *Journal of Fluid Mechanics* **31** (3), 467–479.
- 1390 COHEN-SABBAN, J., GAILLARD-GROLEAS, J. & CREPIN, P.-J. 2001 Quasi-confocal extended field surface  
1391 sensing. In *Proceedings of SPIE* (ed. A. Duparre & B. Singh), *Optical Metrology Roadmap for the*  
1392 *Semiconductor, Optical, and Data Storage Industries II*, vol. 4449, pp. 178–183.
- 1393 DEMEKHIN, E. A. 1981 Nonlinear waves in a liquid film entrained by a turbulent gas stream. *Fluid Dyn.* **16**,  
1394 188–193.
- 1395 DIETZE, G. F. 2016 On the Kapitza instability and the generation of capillary waves. *Journal of Fluid*  
1396 *Mechanics* **789**, 368–401.
- 1397 DIETZE, G. F. 2019 Effect of wall corrugations on scalar transfer to a wavy falling liquid film. *Journal of*  
1398 *Fluid Mechanics* **859**, 1098–1128.
- 1399 DIETZE, G. F. & RUYER-QUIL, C. 2013 Wavy liquid films in interaction with a confined laminar gas flow. *J.*  
1400 *Fluid Mech.* **722**, 348–393.
- 1401 DOEDEL, E. J. 2008 AUTO07P: Continuation and bifurcation software for ordinary differential equations.  
1402 *Montreal Concordia University*.
- 1403 DROSOS, E. I. P., PARAS, S. V. & KARABELAS, A. J. 2006 Counter-current gas-liquid flow in a vertical narrow  
1404 channel - liquid film characteristics and flooding phenomena. *Int. J. Multiphase Flow* **32**, 51–81.
- 1405 FAIR, J. R. & BRAVO, J. L. 1990 Distillation columns containing structured packing. *Chemical Engineering*  
1406 *Progress* **86** (1), 19–29.
- 1407 FLORYAN, J. M., DAVIS, S. H. & KELLY, R. E. 1987 Instabilities of a liquid film flowing down a slightly  
1408 inclined plane. *Phys. Fluids* **30** (4), 983–989.
- 1409 FREDERICK, K. A. & HANRATTY, T. J. 1988 Velocity measurements for a turbulent nonseparated flow over  
1410 solid waves. *Experiments in Fluids* **6** (7), 477–486.
- 1411 HALPERN, D. & GROTBORG, J. B. 2003 Nonlinear saturation of the rayleigh-instability due to oscillatory flow  
1412 in a liquid-lined tube. *J. Fluid Mech.* **492**, 251–270.
- 1413 HANRATTY, T. J. & ENGEN, J. M. 1957 Interaction between a turbulent air stream and a moving water surface.  
1414 *AIChE Journal* **3** (3), 299–304.
- 1415 KALLIADASIS, S., RUYER-QUIL, C., SCHEID, B. & VELARDE, M. G. 2012 *Falling Liquid Films, Applied*  
1416 *Mathematical Sciences*, vol. 176. Springer Verlag.
- 1417 KAPITZA, P. L. 1948 Wave flow of thin layer of viscous fluid (in Russian). *Zhurn. Eksper. Teor. Fiz.* **18** (1),  
1418 3–28.
- 1419 KOFMAN, N. 2014 Films liquides tombants avec ou sans contre-écoulement de gaz: application au problème  
1420 de l'engorgement dans les colonnes de distillation. PhD thesis, Université Pierre et Marie Curie.
- 1421 KOFMAN, N., MERGUI, S. & RUYER-QUI, C. 2014 Three-dimensional instabilities of quasi-solitary waves in  
1422 a falling liquid film. *Journal of Fluid Mechanics* **757**, 854–887.
- 1423 KOFMAN, N., MERGUI, S. & RUYER-QUIL, C. 2017 Characteristics of solitary waves on a falling liquid film  
1424 sheared by a turbulent counter-current gas flow. *Int. J. Multiph. Flow* **95**, 22–34.
- 1425 KUPFER, K., BERS, A. & RAM, A. K. 1987 The cusp map in the complex-frequency plane for absolute  
1426 instabilities. *Physics of Fluids* **30** (10), 3075–3082.
- 1427 KUSHNIR, R., BARMAK, I., ULLMANN, A. & BRAUNER, N. 2021 Stability of gravity-driven thin-film flow in  
1428 the presence of an adjacent gas phase. *International Journal of Multiphase Flow* **135**, 103443.
- 1429 LAPKIN, A. & ANASTAS, P. T., ed. 2018 *Green Chemical Engineering, Handbook of Green Chemistry*,  
1430 vol. 12. Wiley-VHC.
- 1431 LAVALLE, G., GRENIER, N., MERGUI, S. & DIETZE, G. F. 2020 Solitary waves on superconfined falling liquid  
1432 films. *Physical Review Fluids* **5** (3), 032001(R).
- 1433 LAVALLE, G., LI, Y., MERGUI, S., GRENIER, N. & DIETZE, G. F. 2019 Suppression of the kapitza instability  
1434 in confined falling liquid films. *Journal of Fluid Mechanics* **860**, 608–639.



- 1435 LAVALLE, G., MERGUI, S., GRENIER, N. & DIETZE, G. F. 2021 Superconfined falling liquid films: linear  
1436 versus nonlinear dynamics. *Journal of Fluid Mechanics Rapids* **919**, R2.
- 1437 LEL, V.V., AL-SIBAI, F., LEEFKEN, A. & RENZ, U. 2005 Local thickness and wave velocity measurement  
1438 of wavy films with a chromatic confocal imaging method and a fluorescence intensity technique.  
1439 *Experiments in Fluids* **39** (5), 856–864.
- 1440 LIU, J. & GOLLUB, J. P. 1993 Onset of spatially chaotic waves on flowing films. *Physical Review Letters*  
1441 **70** (15), 2289–2292.
- 1442 LIU, J. & GOLLUB, J. P. 1994 Solitary wave dynamics of film flows. *Physics of Fluids* **6** (5), 1702–1712.
- 1443 LUCHINI, P. & CHARRU, F. 2019 On the large difference between Benjamin’s and Hanratty’s formulations of  
1444 perturbed flow over uneven terrain. *Journal of Fluid Mechanics* **871**, 534–561.
- 1445 MATLAB 2015 *Version 8.6 (R2015b)*. Natick, Massachusetts: The MathWorks Inc.
- 1446 MCCREADY, M. J. & CHANG, H.-C. 1994 Formation of large disturbances on sheared and  
1447 falling liquid films. *Chemical Engineering Communications* **141-142** (1), 347–358, arXiv:  
1448 <http://www.tandfonline.com/doi/pdf/10.1080/00986449608936423>.
- 1449 MERGUI, S., LAVALLE, G., LI, Y., GRENIER, N. & DIETZE, G. F. 2023 Nonlinear dynamics of strongly-confined  
1450 gas-sheared falling liquid films. *Journal of Fluid Mechanics* **954**, A19.
- 1451 MEZA, C. E. & BALAKOTAIAH, V. 2008 Modeling and experimental studies of large amplitude waves on  
1452 vertically falling films. *Chemical Engineering Science* **63**, 4704–4734.
- 1453 MIESEN, R. & BOERSMA, B. J. 1995 Hydrodynamic stability of a sheared liquid film. *J. Fluid Mech.* **301**,  
1454 175–202.
- 1455 MILES, J. W. 1957 On the generation of surface waves by shear flows. *J. Fluid Mech.* **3**, 185–204.
- 1456 MIYARA, A. 1999 Numerical analysis on flow dynamics and heat transfer of falling liquid films with  
1457 interfacial waves. *Heat and Mass Transfer* **35**, 298–306.
- 1458 MOISY, F., RABAUD, M. & SALSAC, K. 2009 A synthetic schlieren method for the measurement of the  
1459 topography of a liquid interface. *Experiments in Fluids* **46**, 1021–1036.
- 1460 NÁRAIGH, L. Ó., SPELT, P. D. M., MATAR, O. K. & ZAKI, T. A. 2011 Interfacial instability in turbulent flow  
1461 over a liquid film in a channel. *International Journal of Multiphase Flow* **37** (7), 812–830.
- 1462 ORON, A. & GOTTLIEB, O. 2004 Subcritical and supercritical bifurcations of the first- and second-order  
1463 Benney equations. *Journal of Engineering Mathematics* **50** (2-3), 121–140.
- 1464 ORSZAG, S. A. 1971 Accurate solution of the Orr-Sommerfeld stability equation. *Journal of Fluid Mechanics*  
1465 **50** (4), 689–703.
- 1466 ÖZGEN, S., CARBONARO, M. & SARMA, G. S. R. 2002 Experimental study of wave characteristics on a thin  
1467 layer of de/anti-icing fluid. *Physics of Fluids* **14** (10), 3391–3402.
- 1468 POPE, S. B. 2000 *Turbulent Flows*. Cambridge University Press.
- 1469 PRANDTL, L. 1925 Bericht über Untersuchungen zur ausgebildeten Turbulenz. *Zeitschrift für angewandte*  
1470 *Mathematik und Mechanik* **5**, 136–139.
- 1471 RICHARD, G., RUYER-QUIL, C. & VILA, J. P. 2016 A three-equation model for thin films down an inclined  
1472 plane. *Journal of Fluid Mechanics* **804**, 162–200.
- 1473 RUSSO, S. & LUCHINI, P. 2016 The linear response of turbulent flow to a volume force: comparison between  
1474 eddy-viscosity model and dns. *Journal of Fluid Mechanics* **790**, 104–127.
- 1475 RUYER-QUIL, C. & MANNEVILLE, P. 1998 Modeling film flows down inclined planes. *Eur. Phys. J. B* **6** (2),  
1476 277–292.
- 1477 RUYER-QUIL, C. & MANNEVILLE, P. 2000 Improved modeling of flows down inclined planes. *Eur. Phys. J.*  
1478 *B* **15** (2), 357–369.
- 1479 RUYER-QUIL, C. & MANNEVILLE, P. 2002 Further accuracy and convergence results on the modeling of flows  
1480 down inclined planes by weighted-residual approximations. *Phys. Fluids* **14** (1), 170–183.
- 1481 SAMANTA, A. 2014 Shear-imposed falling film. *Journal of Fluid Mechanics* **753**, 131–149.
- 1482 SAMANTA, A. 2020 Optimal disturbance growth in shear-imposed falling film. *AIChE Journal* **66** (5),  
1483 0001–1541.
- 1484 SCHMIDT, P., NÁRAIGH, L. Ó., LUCQUIAUD, M. & VALLURI, P. 2016 Linear and nonlinear instability in vertical  
1485 counter-current laminar gas-liquid flows. *Physics of Fluids* **28**, 042102.
- 1486 SHKADOV, V. YA. 1967 Wave flow regimes of a thin layer of viscous fluid subject to gravity. *Fluid Dyn.* **2** (1),  
1487 29–34.
- 1488 THOMPSON, A. B., GOMES, S. N., DENNER, F., DALLASTON, M. C. & KALLIADASIS, S. 2019 Robust low-  
1489 dimensional modelling of falling liquid films subject to variable wall heating. *Journal of Fluid*  
1490 *Mechanics* **877**, 844–881.

- 1491 THORSNESS, C. B., MORRISROE, P. E. & HANRATTY, T. J. 1978 A comparison of linear theory with  
1492 measurements of the variation of shear stress along a solid wave. *Chem. Eng. Sci.* **33**, 579–592.
- 1493 TILLEY, B. S., DAVIS, S. H. & BANKOFF, S. G. 1994 Linear stability theory of two-layer fluid flow in an  
1494 inclined channel. *Phys. Fluids* **6** (12), 3906–3922.
- 1495 TREFETHEN, L. N. 2000 *Spectral methods in MATLAB*. Philadelphia: SIAM.
- 1496 TRIFONOV, Y. Y. 2010a Counter-current gas-liquid wavy film flow between the vertical plates analyzed using  
1497 the Navier-Stokes equations. *AIChE Journal* **56** (8), 1975–1987.
- 1498 TRIFONOV, Y. Y. 2010b Flooding in two-phase counter-current flows: Numerical investigation of the gas-  
1499 liquid wavy interface using the Navier-Stokes equations. *Int. J. Multiphase Flow* **36**, 549–557.
- 1500 TRIFONOV, Y. Y. 2017 Instabilities of a gas-liquid flow between two inclined plates analyzed using the  
1501 Navier-Stokes equations. *International Journal of Multiphase Flow* **95**, 144–154.
- 1502 TRIFONOV, Y. Y. 2019 Nonlinear wavy regimes of a gas-liquid flow between two inclined plates analyzed  
1503 using the Navier-Stokes equations. *International Journal of Multiphase Flow* **112**, 170–182.
- 1504 TSELUIKO, D. & KALLIADASIS, S. 2011 Nonlinear waves in counter-current gas-liquid film flow. *J. Fluid*  
1505 *Mech.* **673**, 19–59.
- 1506 VALLURI, P., MATAR, O. K., HEWITT, G. F. & MENDES, M. A. 2005 Thin film flow over structured packings  
1507 at moderate Reynolds numbers. *Chem. Eng. Sci.* **60**, 1965–1975.
- 1508 VAN DRIEST, E. R. 1956 On turbulent flow near a wall. *Journal of the Aeronautical Sciences* **23** (11),  
1509 1007–1011, arXiv: <https://doi.org/10.2514/8.3713>.
- 1510 VELLINGIRI, R., TSELUIKO, D. & KALLIADASIS, S. 2015 Absolute and convective instabilities in counter-  
1511 current gas-liquid film flows. *Journal of Fluid Mechanics* **763**, 166–201.
- 1512 VLACHOS, N. A., PARAS, S. V., MOUZA, A. A. & KARABELAS, A. J. 2001 Visual observations of flooding in  
1513 narrow rectangular channels. *Int. J. Multiphase Flow* **27**, 1415–1430.
- 1514 YIH, C. S. 1963 Stability of liquid flow down an inclined plane. *The Physics of Fluids* **6** (3), 321–334.
- 1515 YOSHIMURA, P. N., NOSOKO, P. & NAGATA, T. 1996 Enhancement of mass transfer into a falling laminar liquid  
1516 film by two-dimensional surface waves—some experimental observations and modeling. *Chemical*  
1517 *Engineering Science* **51** (8), 1231–1240.
- 1518 ZAPKE, A. & KRÖGER, D. G. 2000 Countercurrent gas-liquid flow in inclined and vertical ducts - I: Flow  
1519 patterns, pressure drop characteristics and flooding. *International Journal of Multiphase Flow* **26**,  
1520 1439–1455.
- 1521 ZHOU, G. & PROSPERETTI, A. 2020 Capillary waves on a falling film. *Physical Review Fluids* **5**, 114005.
- 1522 ZILKER, D. P., COOK, G. W. & HANRATTY, T. J. 1977 Influence of the amplitude of a solid wavy wall on a  
1523 turbulent flow. part 1. non-separated flows. *Journal of Fluid Mechanics* **82** (1), 29–51.